INSTITUTO TECNOLÓGICO Y DE ESTUDIOS SUPERIORES DE MONTERREY

CAMPUS MONTERREY

SCHOOL OF ENGINEERING AND INFORMATION TECHNOLOGIES GRADUATE PROGRAM

A CMOS CANTILEVER PLATFORM USING ADSORPTION-INDUCED SURFACE STRESS AND PIEZORESISTIVE TRANSDUCTION FOR BIOSENSING

THESIS

SUBMITTED IN PARTIAL FULFILLMENT OF THE REQUIREMENTS FOR THE DEGREE OF

MASTER OF SCIENCE IN ELECTRONIC ENGINEERING (ELECTRONICS SYSTEMS)

BY

ADRIÁN ABDALÁ RENDÓN HERNÁNDEZ, B.Sc.

MONTERREY, N.L. DECEMBER, 2012

© Adrián Abdalá Rendón Hernández, 2012.

INSTITUTO TECNOLÓGICO Y DE ESTUDIOS
SUPERIORES DE MONTERREY

CAMPUS MONTERREY

SCHOOL OF ENGINEERING AND INFORMATION TECHNOLOGIES
GRADUATE PROGRAM

A CMOS Cantilever Platform using Adsorption-induced Surface Stress and Piezoresistive Transduction for Biosensing

THESIS

SUBMITTED AS PARTIAL FULFILLMENT OF THE
REQUIREMENTS FOR THE DEGREE OF

MASTER OF SCIENCE IN ELECTRONIC ENGINEERING
(ELECTRONICS SYSTEMS)

BY

ADRIÁN ABDALÁ RENDÓN HERNÁNDEZ, B.Sc.

MONTERREY, N.L. DECEMBER, 2012

In memoriam of my dear father Pedro RENDÓN. Although there are no words to express my gratefulness to you, thank you for all those good times. I still miss you. **Q.E.P.D.**
To those who always believe in my dreams, Emilia and Arlene, this thesis is lovingly dedicated to you.
"If we knew what it was we were doing, it would not be called research, would it?" - Albert Einstein (1879 - 1955).

Acknowledgements

This thesis work would not have been possible without the guidance and the help of several individuals who in one way or another contributed and extended their valuable preparation and completion of this study. During the years I have spent at Tecnolgógico de Monterrey I have been very happy, to learn a lot from incredible people through academic and social interactions. I hope this lines can convey how thankful I am for their continuing support, invaluable friendship and great memories.

First and foremost, my utmost gratitude to Professor Dr. Sergio Omar Martínez Chapa, Director of the Department of Electrical and Computer Engineering and the BioMEMS Research Chair, for his invaluable teaching, constant patience, abiding support, and his motivation in order to achieve this thesis and projects involving my passion, the research. I am indebted to him for accepting me in his research group so I can make this dream true. His constructive criticism was essential to overcome the early stages of my research. I strongly hope that one day I can develop some of his skills as a mentor and researcher.

It gives me great pleasure in acknowledging the support and help of Professor Dr. Graciano Dieck Assad, who introduced me to Microelectronics, and whose sincerity and encouragement I will never forget.

This thesis would have remained a dream had it not been for Professor Dr. Sergio Camacho León, who introduced me to MEMS. his continuous encouragement and discussions helped me to understand the physics involved in Microsystems branch.

Thanks to my colleagues who always shared the days of hard work with me.

This research was jointly funded by the Research Chair in Biointeractive Systems and BioMEMS of the Instituto Tecnológico y de Estudios Superiores de Monterrey, Campus Monterrey, and by Nacional Council on Science and Technology (CONACyT) of México.

Last, but not the least, my family and the one above all of us, the omnipresent God, for answering my prayers for giving me the strength to plod on despite my constitution wanting to give up and throw in the towel, than you so much Dear Lord. I must thank

my Dear mom, Emilia, who has always been able to face my absence, in exchange for get my dreams. To my Dear Arlene, who lovingly and charm has always believed and supported all my dreams and has been a source of inspiration, thank you my love.

Adrián Abdalá Rendón Hernández.

A CMOS-based Cantilever Platform Using Adsorption-Induced Surface Stress and Piezoresistive Transduction for Biosensing

Adrián Abdalá Rendón Hernández, B.Sc.
Instituto Tecnológico y de Estudios Superiores de Monterrey, 2012.

Advisor: Sergio Omar Martínez Chapa, Ph.D.
Instituto Tecnológico y de Estudios Superiores de Monterrey.

ABSTRACT

This work proposes a biosensing platform based on a microcantilever operating in static mode. The microcantilever transforms the adsorption-induced surface stress into a deflection which is then transformed in an electrical signal by means of a piezoresistive element that is embedded in the structure.

A non-destructive and independent-of-fabrication-processes method to characterize residual stress within composite micromachined beams has been proposed. The method was validated by comparing available experimental data and simulation results from fourteen microbeams obtaining an average of 27% absolute error concerning the maximum deflection of the structures.

A multipysics model incorporating a suspended beam, a piezoresistor and a Wheatstone bridge has been created in Comsol and used to explore performance of different piezoresistor geometries. A serpentine piezoresistor compared favorably among different geometries and showed a sensibility of $116\Omega/\mu m$.

Finally, several Bandgap references were designed to be used in conjunction with the Wheatstone bridge in order to get low sensibilities to temperature and voltage supply variations. The best reference showed sensibilities of $18\,ppm/^{\circ}C$ and $3.2mV/V$.

This platform was entirely designed to be fabricated in a CMOS process, and is expected to be used in the future to detect and quantify different analytes for environmental monitoring, food industry and biomedicine.

Contents

List of Figures xi

List of Tables xii

1 Introduction 1

1.1 Microsensors . . . 1
1.2 MEMS-based Sensor Applications . . . 3
1.3 Motivation of this Thesis . . . 4
1.3.1 Statement of the Problem . . . 4
1.4 Thesis Aim and Contributions . . . 5
1.5 Thesis Outline . . . 6

2 State of the Art on Cantilever-based Biosensors 7

2.1 CMOS-based Cantilever as Biosensor . . . 7
2.2 Discussion . . . 16
2.3 Proposed model . . . 16

3 Theoretical background 19

3.1 Adsorption Induced Surface Stress . . . 19
3.1.1 Mechanism of Bending . . . 22
3.1.2 Responses of Microcantilever Sensor Depending of Coatings . . 26
3.1.2.1 Interactions Around Microcantilever . . . 26
3.1.2.2 Surface with Analyte-Permeable Coating . . . 27
3.1.2.3 Nanostructured Interfaces and Coatings . . . 28
3.1.3 Modeling Adsorption Onto a Surface . . . 29
3.1.3.1 Surface Reconstruction . . . 29
3.1.3.2 Interaction Energy . . . 30
3.1.3.3 Coverage of the Adsorbate . . . 31
3.1.3.4 Adsorption Kinetics . . . 31
3.1.3.5 Electrostatic Interactions . . . 32
3.1.3.6 Surface Charge Redistribution . . . 32
3.2 Cantilever Deflection Associated to Residual Stress . . . 33
3.2.1 Proposed Method to Characterize Residual Stress . . . 36
3.3 Polysilicon Piezoresistive Sensing Elements . . . 40

3.3.1 Piezoresistance Effect in Polysilicon . . . 40
3.3.2 Polysilicon Piezoresistor . . . 41
3.3.3 Average Piezoresistive Coefficient . . . 42
3.3.4 Growth Orientation of [k, 0, m] Plane . . . 43
3.3.5 Growth Orientations of [k, k, n] Plane . . . 44
3.3.6 Completely Random Distribution . . . 46
3.4 Read-Out-Circuit . . . 47
3.4.1 Bandgap References . . . 48

4 Modeling Cantilever-based Sensors 50
4.1 Simulating Residual Stress . . . 51
4.2 Characterizing Residual Stress . . . 55
4.3 Discussion . . . 60

5 Modeling Piezoresistive Transducer 61
5.1 Modeling a First Geometry . . . 61
5.1.1 Discussion . . . 69
5.2 Modeling a Second Geometry . . . 69
5.2.1 Discussion . . . 74
5.3 Modeling a Third Geometry . . . 74
5.3.1 Discussion . . . 79

6 Voltage Reference Circuit 81
6.1 Voltage Reference . . . 81
6.2 Traditional Bandgap Reference Circuit in CMOS . . . 82
6.3 Design of Bandgap Voltage Reference . . . 83
6.3.1 Simulating Bandgap Voltage Reference 1 . . . 86
6.3.1.1 BGR1 Case I . . . 86
6.3.1.2 BGR1 Case II . . . 89
6.3.2 Simulating Bandgap Voltage Reference 2 . . . 92
6.3.2.1 BGR2 Case I . . . 94
6.3.2.2 BGR2 Case II . . . 96
6.3.2.3 BGR2 Case III . . . 98
6.4 Discussion . . . 100

7 Conclusions 102
7.1 Future Work and Directions . . . 103

Appendix A Complements 104
A.1 Piezoresistive Transduction in CMOS-based Microantilever sensor . . . 104
A.2 Coordinate System Transformation . . . 108
A.3 The Euler's Angles . . . 110

References 121

Vita 122

List of Figures

1.1 Schematic diagram of MEMS components and their relation. 2

2.1 Operation modes of a cantilever sensor 9
2.2 Schematic diagram of stages of our sensing platform proposed. 17
2.3 Topology of proposed model 18

3.1 Working principle of a microcantilever biosensor 20
3.2 Adsorptions and reaction at surfaces 21
3.3 Adsorption-induced surface stress under different perspectives 22
3.4 Arrangement of atoms on microcantilever 24
3.5 Position of surface atoms on deflected beam 25
3.6 First model of modified coatings 27
3.7 Second model of modified coatings 28
3.8 Third model of modified coatings 29
3.9 Surface reconstruction 30
3.10 Geometry of a multilayer beam 34
3.11 View of the plane of symmetry of a linear, isotropic elastic beam 35
3.12 Plane stress condition 37
3.13 Simplified model for a polysilicon material 41
3.14 Some directions in (010) plane 43
3.15 Some main directions in $(01\overline{1})$ plane 45
3.16 Deviations in a piezoresistive bridge 48
3.17 Voltages that increase and decrease with increasing temperature 49

4.1 Model of the microcantilever for simulation 52
4.2 Deflection due residual stress simulation 53
4.3 Comparison deflection profiles 58
4.4 Comparison deflection profiles 59

5.1 Whetstone bridge used in microcantilever 62
5.2 Microcantilever beam number 2, using a Wheatstone bridge 63
5.3 Deflection due to residual stress and a resistive bridge for the beam 2 . 66
5.4 Contribution of effective stress for the beam 2 67
5.5 Outcomes of the read-out-circuit, beam 2 68
5.6 Wheatstone bridge with second geometry 70
5.7 Second geometry of resistive element 70

5.8 3D model for the Wheatstone bridge, for beam 2 71
5.9 Outcomes of the read-out-circuit, second geometry 72
5.10 Von Mises stress, second geometry 73
5.11 Wheatstone bridge with second geometry 75
5.12 Serpentine shaped sensing resistance 75
5.13 Resistive bridge using serpentine shaped element 76
5.14 Von Mises stress, second geometry 77
5.16 Level of meshing applied to the 3D model in serpentine shaped case . . 79

6.1 Traditional bandgap voltage reference circuit 82
6.2 Schematic diagram of bandgap voltage reference 1 85
6.3 Schematic diagram of the Bandgap voltage reference 1 87
6.4 Simulations results of the bandgap voltage reference 1 88
6.5 Simulations results of the bandgap voltage reference 1, case II 91
6.6 Schematic diagram of the Bandgap voltage reference 2 93
6.7 Simulations results of the bandgap voltage reference 2 95
6.8 Simulations results of the bandgap voltage reference 2, case II. 97
6.9 Simulations results of the bandgap voltage reference 2 99

A.1 A piezoresistor at an arbitrary coordinate system 108
A.2 Locating a vector in two coordinate system 109
A.3 Rlationship between two coordinate systems by Euler's angles

List of Tables

2.1 Microcantilever-based biosensors. 10

3.1 Adsorptions and reactions onto a surface 21
3.2 Coefficients of piezoresistivity matrix of polysilicon in (010) plane . . . 44
3.3 Coefficients of piezoresistivity matrix of polysilicon in $(10\bar{1})$ plane . . . 46
3.4 Average of $\overline{\pi}_{11}$, $\overline{\pi}_{12}$, $\overline{\pi}_{66}$ considering a random distribution 47

4.1 Material parameters 51
4.2 Coefficients of deflection profiles by measurement [1]. 54
4.3 Linear gradient stress comparison 55
4.4 Maximum deflections comparison 56
4.5 Room mean square error in deflections 57

5.1 Table of constants, piezoresistivity coefficients 64
5.2 Table of scalar expressions used in the simulation model 65
5.3 Outcomes of parametric sweep analysis, first geometry 69
5.4 Outcomes of parametric sweep analysis, second geometry 74
5.5 Outcomes of parametric sweep analysis, third geometry 77
5.6 Performance comparison of the three geometries 79

6.1 Features of devices in Bandgap voltage reference 1, case I 87
6.2 Features of devices in Bandgap voltage reference 1, case II 90
6.3 Features of devices in Bandgap voltage reference 2, case I 94
6.4 Features of devices in Bandgap voltage reference 2, case II 96
6.5 Features of devices in bandgap voltage reference 2, case III 98
6.6 Comparison of results 101

A.1 Components of the piezoresistive coefficient tensor in silicon. 108
A.2 Piezoresistive tensor at an arbitrary coordinate system

Chapter 1

Introduction

1.1 Microsensors

Speaking about the origins of the microelectromechanical systems (MEMS), it is certainly talked of works published in the early of 1950's, as the paper published by [2] in April of 1954. Another precedent of this technology is the work made by [3], where the variation of resistivity of high-purity single crystals of silicon has been measured as a function of hydrostatic pressure in the intrinsic range.

Nowadays, the term MEMS is extensively referred to all ways to miniaturize devices, mostly fabricated form materials as silicon and using techniques which are often derived from the microelectronics industry as the isotropic and anisotropic etching, various thin film deposition methods, and surface micromachinig as well.

MEMS usually involve the following components: mechanical microstructures, microsensors, microactuators, and microelectronics [4]. Figure 1.1 shows a schematic of the global components that make up MEMS as we know them today.

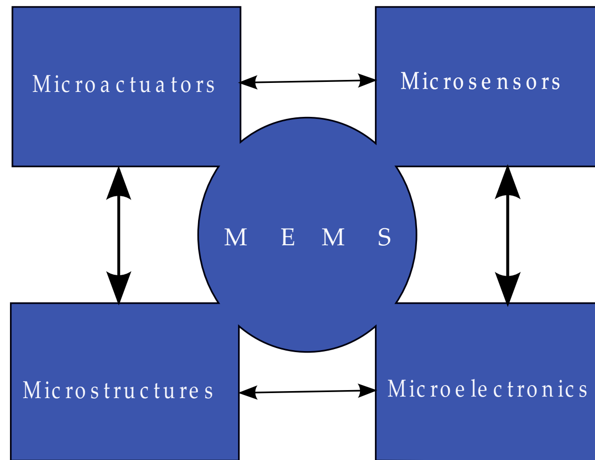

Figure 1.1: Schematic diagram of MEMS components and their relation.

Sensors are devices capable of detecting physical or chemical quantities, such temperature, light, pressure or a gas concentration. Also, a sensor converts a nonelectrical quantity into an electrical signal. Considering the miniaturization techniques, a microsensor can be defined as a sensor having dimensions on the order of the submilimeter.

The popularity of microsensors is strong due to the great advantages that they possess. In addition to their small size, MEMS-based microsensors consume very little power and are capable of delivering accurate measurements, whereas are matchless with macro-sized sensors.

The combination of microsensors and miniaturized electronic circuitry allows, for example, inside our cars, a micro accelerometer to reliably detect collisions and triggers air-bag release. Also having sensors inside the tires allows to alert the driver of a decreasing tire pressure. Moreover, microsensors are also finding their way into medical applications, with the premise of small, portable an easy-to-use equipment and new devices for early diagnosis and therapeutic treatment.

A smart or intelligent sensor is frequently referred to the combination of interface electronics and an integrated sensor on a single chip. One advantage of smart sensors is the improved signal-to-noise ratio and the lower electromagnetic interference [5].

At present, the electronic industry is dominated by the complementary metal-oxide-semiconductor (CMOS) technology. The use of CMOS technology entails a limited selection of device materials and a preestablished fabrication process for the CMOS part. CMOS chips are mass-produced at low cost and consume little power. With each wafer producing thousands of sensors affordably, these sensors can now be used in areas that were economically unthinkable before with other means.

Regardless of application, all MEMS sensors must work on the principle of measuring some form of a change. Some utilize ordinary methods while others use the benefits of

the small dimensions. MEMS sensors are able to detect a bunch of different measurable changes. These include, mechanical, chemical, electrical, and magnetic changes. Often it is then detected either externally with optics or internally with electrical electrodes.

1.2 MEMS-based Sensor Applications

Some areas in which MEMS-based sensors are already being used include: biomedical applications (BioMEMS), medical diagnostics, biosensors (glucose [6], antigens, antibodies [7], DNA [8, 9], proteins, micro-organisms [10], and viruses), pH sensors, environmental monitoring [11], atomic force microscope (AFM) [12], scanning force microscope (SFM) [13], food safety [14], RF switching [15], and high frequency resonators.

While MEMS represent a diverse family of designs, devices with simple cantilever configurations are attractive as transducers for chemical and biological sensors. One of the most important aspects to consider in fabrication of microcantilevers is the type of material and the physical dimensions, both characteristics being determined by the cantilever's application and operation requirements. Most common materials are silicon (Si, monocrystalline or polycristalline or amorphous compositions), polymers, and silicon nitride (SiN).

A cantilever is a type beam which is fixed at only one end. Microcantilevers can be as thin as a few nanometers with lengths that range from a few microns to several hundred microns. The use of microcantilevers as transducers, sensors, switches, actuators, and resonators is increasingly popular due to their intrinsic flexibility, together with the availability of techniques designed to monitor bending.

Considering the microcantilever as the most versatile application of MEMS, it is used to sense the presence of certain analyte or particle by coating it with a chemical or biologically sensitive material. This material must provide for a high level of specificity in detecting particles within a sample or medium.

Regarding MEMS cantilevers as transducers, they rely on their flexibility or elasticity to create some type of measurable change when exposed to external stimuli. This measurable change is referred to as mechanical stress, and this stress results in a change in one of the cantilever's mechanical or electrical properties, for example: resistivity, angular deflection, and natural resonant frequency.

In the environmental and monitoring applications, chemical or biological sensors incorporate microcantilever as transducers. Those sensors detect, analyze and measure specific particles within gas and liquid environments. These particles are usually called *target material*. To detect a specific analyte, a microcantilever is coated on one surface for static operation or both surfaces for dynamic operation. This probe coating is a chemically sensitive layer that provides specificity for molecular recognition. While the

analyte is adsorbed by the probe coating, the microcantilever experiences surface stress or an overall change in mass which cause a cantilever deflection (static mode) or a change in cantilever oscillations (dynamic mode).

Different types of reactions can occur in the probe coating of a microcantilever, when the analytes are adsorbed in the active layer. The exact molecular mechanism involved in adsorption induced stress is not completely understood. Frequently, deflections of microcantilevers are referred in terms of energy transfer between surfaced free energy and elastic energy associated with structural bending of the cantilever [16].

1.3 Motivation of this Thesis

An increasing interest in the research of cantilever-based sensors for detection of biomolecules was observed in the last decade. Environmental monitoring for the detection of pollutants is becoming increasingly important to regulatory agencies, the regulated community, and the general public. Driven by the need for faster and more cost-effective methods for environmental monitoring, a widely variety of environmental field analytical methods are commercially available or currently being developed.

The motivation of this thesis work is based on the study and design of a CMOS-based microcantilever platform using adsorption-induced surface stress as a recognition event and piezoresistive transduction, it is also planned the design of a circuit readout compatible with CMOS technology. The work in this thesis is focused on the use of a finite element analysis in order to model and characterize the multi-physic platform proposed. Concerning the circuit readout, it is used a SPICE simulation based on the C5 process of the MOSIS service.

In particular, biosensors with electrical readouts offer several advantages over their optical counterparts due to their reduced cost, reduced dimensions and ease of signal acquisition. Therefore it is very important to consider a voltage reference that is reasonably independent of both power supply and temperature. These references are typically called *bandgap voltage references*.

The work presented in this thesis includes the modeling and characterization of the microstructure, and its readout circuit. A specific comparison of three different piezoresistive elements is also studied.

1.3.1 Statement of the Problem

All thin film materials are found to be in a state of residual stress, regardless of the means by which they were produced. Therefore, it is expected that the proposed platform has an initial bending moment as a result of the residual stresses developed during

its microfabrication process. This initial bending moment will place the device in a rest position, out of the originally horizontal-considered plane. Residual stress measurement owns its particular importance because residual stress strongly depend on not only the material itself, but the attached substrates, boundary conditions, and processing parameters and histories. Residual stress characterization is more complicated in comparison with other material property such as Young's modules measurement.

For the field of MEMS, the existing of residual stress can seriously influence the reliability and dynamical characteristics of devices [17]. Focusing on the structural integrity perspective, it is necessary to control the residual stress level to prevent structure failure. The existence of tensile residual stress in thin film structures usually results in cracking of thin films, whereas the compressive residual stress existed in MEMS could induce buckling failure in micro beams, or hillocks formulation during microelectronics fabrication.

The need of having a rapid way, to design biosensors based on microcantilever, considering multiphysics involved such as the phenomena of adsorption, the transduction of out-of-plane deflection, and the instrumentation electronics to provide an electrical output signal has stimulated our interest in this line of research.

1.4 Thesis Aim and Contributions

The goal of this thesis work is to develop a platform of sensing based in CMOS-MEMS technology and using a multilayer cantilever as a transducer. Its operation principle is the surface stress induced as a result of adsorption between the target material and the biological receptor. Further, and as a result of residual stress in the multilayer cantilever, deflection is modeled and characterized under a finite element tool. In addition, it is presented a comparison of three different geometries of piezoresistive elements incorporating a bandgap-voltage reference to complete the sensing platform for biological applications.

The contributions of this thesis work are: 1) A microsensor design based on a microcantilever embedding a piezoresistive element, 2) the modeling, in a finite element analysis, of the initial microcantilever deflection as consequence of the residual stress in a CMOS multilayer cantilever. Simulation results were compared with experimental data provided by Camacho [1], 3) the comparison and choice of the geometry of piezoresistive element, that provides better sensitivity in resistance changes, 4) a read-out circuit design using a bandgap-voltage reference compatible with the C5 process of CMOS technology.

1.5 Thesis Outline

Chapter 1 has introduced the research topic of the thesis, the motivation of this work, and the most important applications of the microsensors. An overview of the state of the art in microcantilever-based biosensors is presented in chapter 2, where is also reviewed the CMOS cantilever microsensors and particularly those based on CMOS.

The theoretical framework of the physics describing the residual stress within a multilayer microcantilever is presented in chapter 3. It is described the adsorption phenomena producing surface stress and consequently the bending of the cantilever. The piezoresistive effect as a transduction method in CMOS-based microcantilever sensors is also presented. In chapter 4, cantilever deflection due to residual stress is studied. Simulations with a multiphysics software tool were performed and the results were compared with experimental data available from a previous work in the group [1].

In chapter 5, three different piezoresistive devices are simulated and compared. Chapter 6 shows the design process and simulation of a temperature-independent bandgap voltage reference. Finally, in chapter 7, the results are summarized.

Chapter 2

State of the Art on Cantilever-based Biosensors

This chapter presents a state of the art review of cantilever-based biosensors, a brief overhaul of the first uses of microcantilevers in MEMS. In addition, some of microcantilever-based sensors applications reported in current literature, and the technology used to produce them.

2.1 CMOS-based Cantilever as Biosensor

As a result of a development in MEMS, cantilever-based sensors have been applied in areas like the physical sensing, scanning-probe microscopy, as well as in biological and chemical sensing. Even tough the size of a cantilever-based sensor can be varied, this work focuses on the microcantilever-based sensors with dimensions in the micrometer range.

The use of microcantilever in MEMS dating back to the invention of scanning tunneling microscopy (STM) in 1981 [18] at IBM's Zurich Research Laboratory. The STM allowed researchers to see surface features smaller than an atom. The device is based on the phenomenon known as tunneling, the measurement of the electrical tunneling current from an ultrasharp electrode suspended by a few angstroms above the surface atoms. Then measuring the amount of tunneling that occurs while the tip scans the sample provides the data necessary to plot a picture of the surface [13].

Five years later, the atomic force microscopy (AFM) was developed by Binning [12], where the surface is mapped by the vertical displacement necessary to maintain a constant force on the cantilevered probe. These inventions were an important milestone in establishing efficient technological approaches to microcantilever-based sensors.

Standard CMOS technology offers the advantage of cost effective integrated circuits, programmability and control, embedded sensors, is a good fit for implementation of some of the essential functions of Lab-on-a-Chip [19]. Elements of the CMOS process, originally established for the realization of transistors, resistors and other electronic devices can, either by themselves or in combination with subsequent pos-processing, provide sensor elements.

Biosensing applications demand fast, easy-to-use, cheap, and highly sensitive methods for recognition of biomolecules. These points can be fulfilled by CMOS-based cantilever sensors which are therefore ideal candidates for biosensing applications.

A lot of methods for detecting biological substances in a solution are based on the use of fluorescent markers and optical analysis [20]. Nonetheless, this methods are very time consuming and needs a complex and expensive optical setup. Biosensing applications demand fast, easy-to-use, cheap, and highly sensitive methods for recognition of biomolecules. These points can be fulfilled by CMOS-based microcantilever sensors, which are therefore ideal candidates for biosensing applications.

To date, several works have described the use of microcantilever-based surface stress sensing for biomolecular detection [21]. However, few studies have explored the physical origins of the induced surface stress involved in specific sensing applications [22]. Many works have been focused on the study of microcantilevers-based biosensors, due to versatility that they provide. For the last eight years, the literature has shown several works, as shown the second column in Table 2.1. Furthermore, the sensing device section in Table 2.1 has six relevant characteristics.

Firstly, it is distinguished the sensing mode of the microcantilever-based sensor mentioned, as it is known and is showed in Figure 2.1, there are two modes of operation in a microcantilever as a transducer: static and dynamic mode. Secondly, a specific application of the sensing device is highlighted in order to verifying its relevance in biosensing area, some of branches of biosensing are: chemical detection, medical sensing, and environmental monitoring. Thirdly, and continuing into the sensing device section of Table 2.1, a list of target material is presented, intended for show what is the analyte or target material for each sensor. Fourthly, the transduction method is mentioned, highlighting microcantilever as the main method of transduction. Fifthly, the material involved in fabrication is presented. Many of the cantilever-based sensors are fabricated from silicon due to great compatibility with CMOS processes. Hence, ending with the section of the sensor device, it is determined whether or not belonging to a CMOS process.

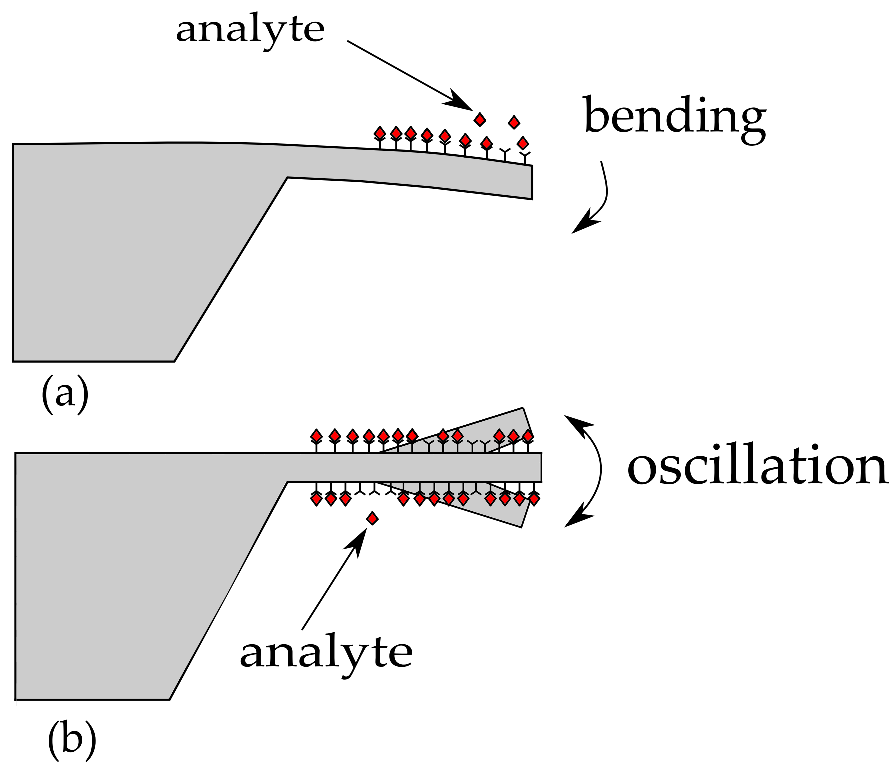

Figure 2.1: (a) Bending of a static microcantilever due to analyte adsorption, (b) resonant operation of the microcantilever.

Furthermore, inside the sensor performance section in Table 2.1 are outlined the sensitivity and size features as a main characteristic to remark in previous works. Sensitivity is frequently defined as the slope of the analytical calibration curve, in other words, how the measurement of the sensor depends on a change in the concentration of analyte.

Table 2.1: Microcantilever-based biosensors.

Publication		**Sensing Device**						**Sensor Performance**	
Reference	Year	Sensing Mode	Application	Target Material	Transduction	Materials	CMOS based	Sensitivity	Size
[23]	2012	Static	Biochemical sensing	12-mer oligonucleotides [24]	Cantilever fitted with organic field effect transistor	SU-8, Pentacene, Au, Cr	Yes	Deflection 15.6ppm/nm, surface stress 401$ppm[mN/m^{-1}]$	Cantilever length 312μm, width 168μm, chip area $4 \times 4mm^2$
[25]	2012	Static	Biochemical sensing	Gas concentration, TNT	Piezoresistive cantilever	SU-8, Au, 4-MBA acid	No	10$\mu V/ppm$	Device area 3.3×4.4cm^2
[26]	2012	Static	Biochemical sensing	Carbon monoxide	Piezoresistive cantilever	Silicon, SU-8, Cr, Au	No	Deflection 1.1 ppm/nm	Cantilever length 200μm, width 50μm, thickness 3.5μm

Continued on next page

Table 2.1 – continued from previous page. Ê

Publication		Sensing Device						Sensor Performance	
Reference	Year	Sensing Mode	Application	Target Material	Transduction	Materials	CMOS based	Sensitivity	Size
[27]	2011	Static	Biochemical detection	DNA	Piezoresistive cantilever	Si, Al	Yes	NR[a]	Cantilever length $5mm$, width $2mm$, thickness $1mm$
[28]	2011	Dynamic & static	Medical application	Motions of heart wall	Piezoelectric cantilever	PZT, ZnO, AlN, PVDF	No	NR[a]	Cantilever length $18mm$, width $7mm$
[29]	2011	Dynamic	Biosensing	DNA molecules	Cantilever embedded MOSFET structure	Si, PZT, SiO_2	Yes	$0.123pg/Hz$	Cantilever length $100\mu m$, width $30\mu m$, thickness $5\mu m$

Continued on next page

[a]**NR:** Not reported in original publication

Table 2.1 – continued from previous page.

Publication		Sensing Device						Sensor Performance	
Reference	Year	Sensing Mode	Application	Target Material	Transduction	Materials	CMOS based	Sensitivity	Size
[30]	2010	Static	Biosensing	Arsenic	Piezoresistive cantilever	Si, SiO_2, Al_2O_3,	No	$0.76 mV/ppm$ at room temperature	Cantilever length $200 \mu m$, width $100 \mu m$, thickness $2 \mu m$
[31]	2010	Static	Biosensing	Salivary alpha amylase, human stress	Piezoresistive cantilever	Si, Polysilicon, SiN, Al	Yes	NR[a]	Piezoresistor length $195 \mu m$, width $75 \mu m$
[32]	2009	Dynamic	Biosensing	Streptavidin and DNA	Oscillator cantilever, lasser-Doppler vibrometer	SU-8, Al_2O_3, Cr, Au,	No	Minimal streptavidin concentration $0.025 \mu g/ml$, 17-mer single DNA strand $0.13 nmol/ml$	SU-8 thickness $1.45 \mu m$

Continued on next page

[a]**NR:** Not reported in original publication.

Table 2.1 – continued from previous page.

Publication		Sensing Device						Sensor Performance	
Reference	Year	Sensing Mode	Application	Target Material	Transduction	Materials	CMOS based	Sensitivity	Size
[33]	2008	Dynamic	Biochemical sensing	Prostate specific antigen	Resonant piezoresistive cantilever	Silicon	Yes	Prostate specific antigen concentrations level down of $10ng/mL$	Cantilever length $150\mu m$, width $140\mu m$
[34]	2008	Static	Biosensing	Biomolecular forces [35]	Piezoresistive cantilever	SiO_2, Si	No	Relative change in resistance $(\Delta R/R)$ $2.25x10^{-6}$	Cantilever length $250\mu m$, width $100\mu m$, thickness $1\mu m$
[36]	2008	Dynamic	Biosensing	Antibody 6xHis Tag [37]	Oscillator cantilever, optical read-out shift frequency	Ni, Si, Ti, Au,	No	$0.32pg/Hz$	Cantilever length $60\mu m$, width $1.4\mu m$, thickness $1.4\mu m$

Continued on next page

Table 2.1 – continued from previous page. Ê

Publication		Sensing Device						Sensor Performance	
Reference	Year	Sensing Mode	Application	Target Material	Transduction	Materials	CMOS based	Sensitivity	Size
[38]	2008	Static	Biomedical	Heartbeat monitoring	Cantilever based capacitive pressure sensor	Si, SiO_2, poly-Si	Yes	NR[a]	Width $200\mu m$
[39]	2008	Static	Biosensing	Myoglobin protein	Cantilever	NR[a]	No	Analyte concentration 10^{-4} to $10^{-15} mol/L$	Cantilever length $500\mu m$, width $100\mu m$, thickness $50\mu m$,
[35]	2007	Static	Biosensing	Forces involved in Biomolecular bonding [40]	Piezoresistive cantilever	Poly-Si, SiO_2	Yes	$11\mu V/pN$	Cantilever length $150\mu m$, width $2\mu m$

Continued on next page

[a]**NR:** Not reported in original publication.

Table 2.1 – continued from previous page. Ê

Publication		Sensing Device						Sensor Performance	
Reference	Year	Sensing Mode	Application	Target Material	Transduction	Materials	CMOS based	Sensitivity	Size
[41]	2005	Static	Biochemical sensing	Ethanol vapor	Piezoresistive cantilever	Poly-Si	Yes	$6nV/ppm$	Cantilever length $300\mu m$, width $300\mu m$, thickness $5\mu m$
[42]	2005	Dynamic	Chemical weapons detection	$C_3H_9O_3P$ dimethyl-methylphos-phonate	Piezoresistive multilayer cantilever, resonant frequency shift	SIO_2, Si_3N_4, poly-Si, Al	Yes	Concentration of $0.1mg/m^3$	Cantilever length $130\mu m$, width $60\mu m$
[43]	2004	Dynamic	Biosensing, envtl. monitoring	Toluene	Piezoresistive resonating cantilever	Poly-Si	Yes	NR[a]	Length $150\mu m$, width $140\mu m$, chip area $2.7x1.3mm^2$

[a]**NR:** Not reported in original publication.

2.2 Discussion

After a qualitative analysis of Table 2.1, it is easy to note that the prevalent sensing mode in the reported microcantilever-based sensors is the static mode. This prevalence can be attributed to the advantage of implementing this cantilever sensing mode in biological applications and under liquid media instead of a dynamic mode of operation because of the damping that the media causes.

Moreover, as Table 2.1 shows, MEMS-based microcantilever sensor proposed by Littrel et al. [44] is one of the few works where multilayered microcantilever are studied, but they do not involve the study of residual stress within the multilayered microcantilever. Accordingly, one of the objective of this thesis work is to model the residual stress in a multilayered microcantilever in order to obtain the operational point or the initial deflection of the structure due to this phenomenon.

Furthermore, the main application that have the microcantilever-based sensors is biosensing detection, as well in environmental monitoring are usually used. Besides, in biochemical applications such as DNA or gas detection, this kind of sensors are recently applied. Despite the last place in the main areas of application showed in Table 2.1, biomedical applications are evidence of the versatility of a microcantilever-based sensor. Depending of application area, the target material or analyte can be from heartbeat monitoring [38], ethanol vapor [41], to some chemical weapons [42].

On the other hand, the predominant transduction method is piezoresistive microcantilever. One of the reasons of this trend is the ease to implement readout circuitry and feasibility to produce a portable device. Others alternatives are proposed such as piezoelectric microcantilever using a laser-Doppler vibrometer [32], and microcantilever embedded MOSFET structure [29].

At last, actual literature makes clear the extended use of CMOS process as a fundamental part of fabrication of microcantilever-based biosensors, in contrast with the structures that are not based in CMOS technology. Summarizing, based on the trends set by the state of the art in microcantilever-based biosensors, our proposed sensing platform is located within these trends.

2.3 Proposed model

Considering the current literature summarized in Table 2.1, our proposed model is based in most of the current state of the art in microcantilever-based biosensors features. The platform consists in a microcantilever of a given length, made of multilayers of metals and oxides. Each layer has the same length and width, but not the same thickness. The multilayered microcantilever has a free end and a fixed end using the silicon substrate.

Very close to the fixed end of microcantilever, there is a embedded piezoresistive element, made of polysilicon. The piezoresistive element serves to provide a translation from a mechanical signal as the deflection of microcantilever to a electrical signal as change in electrical resistance.

Regarding the principle of operation of our sensing platform, there are three main stages involved. First, the translation of energy from chemical to mechanical. In this stage, the adsorption that occurs between the probe coating and the analyte, in the upper surface of the microcantilever, results in a mechanical deflection of the structure. Second, this mechanical change in deflection is detected by the piezoresistive element embedded on the structure, by deforming his geometry. At this stage, the translation of energy from chemical to mechanical and then to electrical is achieved. Third, the change in electrical resistance is rendered in a voltage output by a CMOS-based readout circuit. Figure 2.2 depicts a schematic diagram of the main three stages, above mentioned, involved in our proposed model.

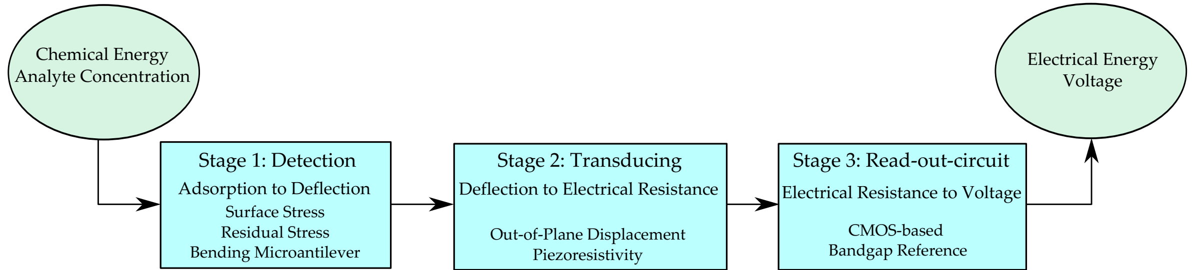

Figure 2.2: Schematic diagram of stages of our sensing platform proposed.

In the following chapters, it will be studied each stage of the sensing platform proposed. But before that, chapter 3 will outline the principles of multiphysics implicated in respective stage of sensing process. For instance, the first step in the sensig process involves phenomenon such as adosrption-induced surface stress by the interaction between the analyte and the probe coating of microcantilever. Several analytical methods to model that interaction will be mentioned. Then in the second step, the action of transduction is performed by the deflection of microcantilever which results from surface stress. A fitted method presented by [1] will be adopted to guide the corresponding simulation in chapter 4. In addition, the piezoresistivity of polysilicon will be studied. Finally, will be studied the fundamentals of the design of a CMOS-based bandgap voltage reference as part of the read-out circuit.

The proposed sensing platform (Figure 2.3) is a CMOS-based multilayered cantilever equipped with a piezoresistive element. The length of the microcantilever is denoted by L, the width by W and the total thickness including oxides and metal layers is depicted by t. This microcantilever is clamped at one end to the substrate but is contiguous with the structure. The platform is designed to work as a biosensor, therefore, its upper surface will be equipped with a bioreceptor, which is beyond the scope of this thesis work. However, the operation mechanism of the sensing platform will be studied

starting from the interaction between the bioreceptor and the probe coating of the microcantilever, as well the surface stress generated and the residual stress within the device.

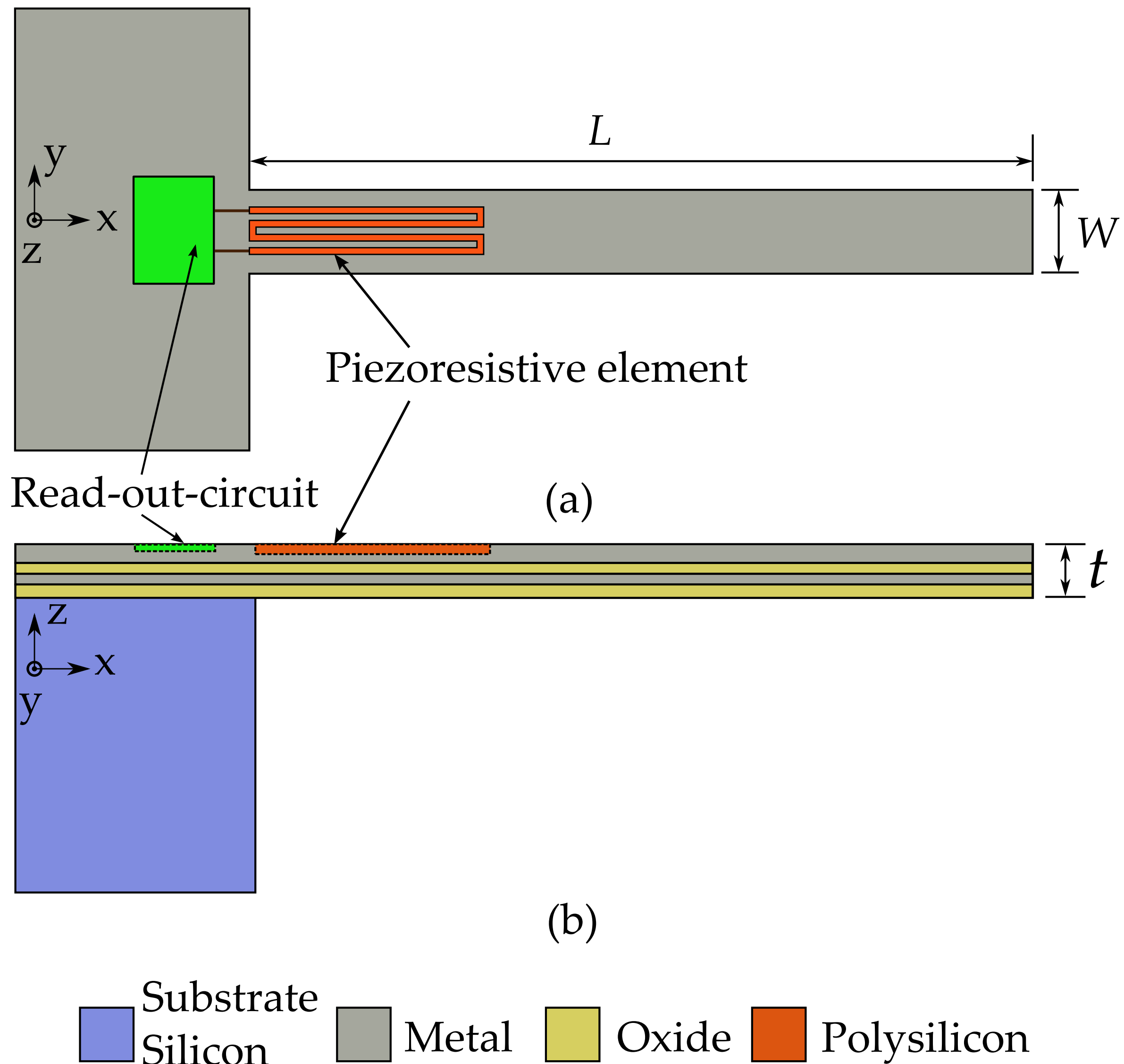

Figure 2.3: Schematic definition of the proposed CMOS-based sensing platform: (a) top view with embedded piezoresistive element, (b) side view with oxide and metal layers.

Figure 2.3 shows a read-out-circuit placed near to piezoresistive element, for the sake of simplicity is presented by a block, nonetheless, chapter 6 presents the design of this CMOS-based circuit and a comparison between two different models and their performance by a SPICE simulation.

Chapter 3

Theoretical background

This chapter is divided in three main sections. Firstly, based on the schematic diagram of Figure 2.2, it is presented the theoretical background for the detection stage, where adsorption occurs between the analyte and the probe coating, consequently a surface stress is induced, and a subsection intended to analyze the fundamentals of residual stress that affects the microcantilever deflection. Secondly, another section will present the fundamentals of piezoresistance effect in polysilicon. By using a simplified model to characterize a polysilicon material, the piezoresistive effect of polysilicon piezoresistors are discussed. Thirdly, the representation of change in electrical resistance as a change in voltage is studied in the last section of this chapter, as well as design principles of CMOS-based read out circuit.

3.1 Adsorption Induced Surface Stress

Microantilevers show potential as highly sensitive biochemical sensors. Microantilever-based sensing involves the transduction of a biomolecular interaction to a measurable mechanical change in the microcantilever resulting from induced surface stress [45].

Microcantilever-based sensors have two operational modes: resonance frequency variation due to mass loading and cantilever bending due to differential adsorption. Microcantilever bending due to adsorption induced is observed when the adsorption is confined to a single side of a microcantilever. For the surface stress sensing applications, one side of the microcantilever beam is rendered sensitive to a specific target molecule, as long as the opposing surface is chemically passivated [46]. At the moment that target molecules interact with the sensitized surface of the microcantilever, the change in surface stress between the sensitized and passivated surfaces results in a well measurable mechanical deflection of the microcantilever.

The adsorption-induced microcantilever bending is ideally suited for measurements in air or under solution. The behavior of the microcantilever beam substrate on application of the adsorbate or analyte is shown in Figure 3.1. First the microcantilever in static mode with the adsorbent. Next, the adsorption between the adsorbate and the adsorbent producing surface stress, and finally, the deflection of microcantilever.

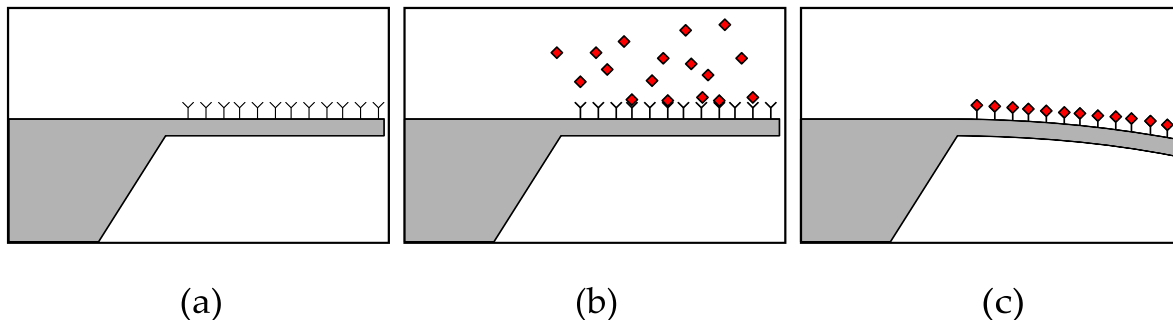

Figure 3.1: (a) Microcantilever in static mode before adsorption (b) Deposition of absorbate on sensign platform (c) Surface stress induced deflection

As definition of adsorption, it is said that is the adhesion or accumulation of atoms, ions, or molecules from a gas, liquid or dissolved solid to a determined surface. In principle, adsorption can occur at any solid-fluid interface. For instance: gas-solid interface (as in the adsorption of volatile organic compounds on activated carbon), and liquid-solid interface (as adsorption of an organic pollutant on activated carbon).

Adsorbate: or solute is the material being adsorbed (e.g., 6-trichlorophenol).

Adsorbent: the solid material being used as the adsorbing phase (e.g., activated carbon).

It has been known since 1960's [47] that molecular and atomic adsorbates on atomically pure faces of single crystals tend to induce surface stress changes [48]. Moreover, it is distinguished two types of adsorption: (a) Physical adsorption, or called physisortpion, where generally a molecule is physisorbed if the bond energy is less than 10 kcal/mole. On the other hand, (b) Chemical adsorption, also called chemisorption, it is chemisorbed if bond energy is more than 10 kcal/mole. A summary of features of those two types of adsorption and reaction at surfaces are shown in Table 3.2 while Figure 3.2 shows a molecular scale representation of these two phenomena.

Table 3.1: Adsorptions and reactions onto a surface

PHYSISORPTION	CHEMISORPTION
Weak, long range bonding, binding energy $< 0.1eV$ [48]	Strong, short range bonding, binding energy $> 0.3eV$ [48]
Van der Waals interactions (e.g. London dispersion, dipole-dipole)	Chemical bonding involving orbital overlap and charge transfer
Not surface specific, it takes place between all molecules on any surface providing the temperature is low enough	Surface specific, as chemisorption of hydrogen takes place on transition metals but not on gold or mercury
Non activated with equilibrium achieved relatively quickly. Increasing temperature always reduces surface coverage	Can be activated, in which case equilibrium can be slow and increasing temperature can favor adsorption

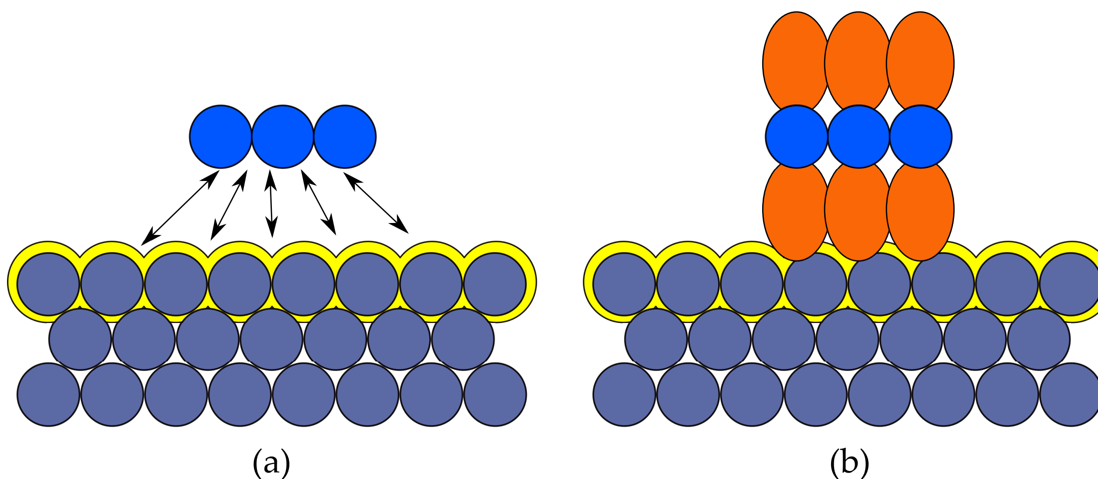

Figure 3.2: (a) Physisorption representation (b) Chemisorption representation

Under the condition that microcantilever-based sensing is to become as viable technology in strategic areas such as medical diagnostics, food safety and environmental monitoring, the origins of the surface stress signal need to be better understood and used to significantly improve performance. So far, several works have described the use of microcantilever-based surface stress sensing for biomolecular detection. Despite the wide number of demonstrated applications, few studies have explored the physical origins of the induced surface stress involved in specific sensing applications [22].

The exact molecular mechanism involved in adsorption-induced stress is not completely understood. However, frequently, deflections of microcantilevers are explained as a function of energy transfer between surfaced free energy and elastic energy associated with structural bending of the cantilevers. Accordingly with figure 3.3, relevant literature explains a mechanism of bending in terms of atomic energy and elastic energy [16]. Then,

Lavrik et al. [48] have proposed three distinctive models in order to understand how different modifying coatings provide responses of microcantilever sensors in the static bending mode. Finally, several models involving the adsorption onto a surface [49, 21] are presented as an overall literature review.

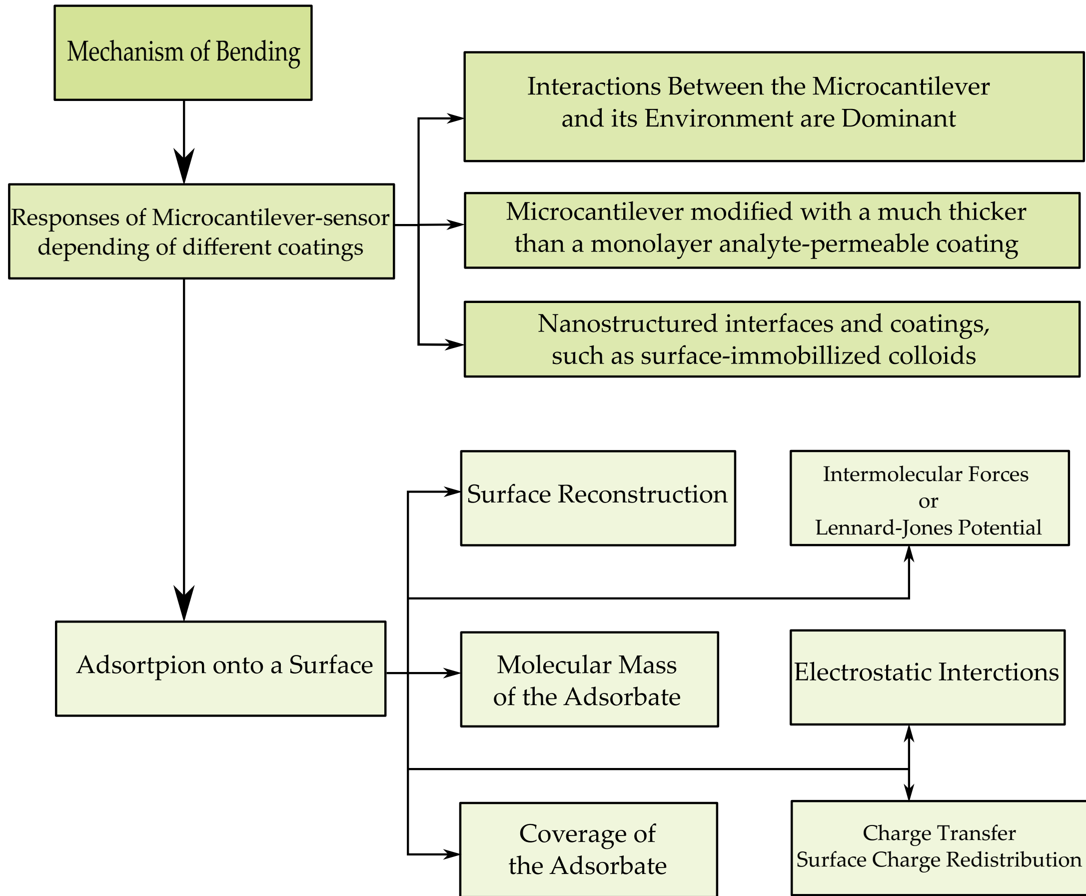

Figure 3.3: Adsorption-Induced Surface Stress under different perspectives

3.1.1 Mechanism of Bending

A model for adsorption-induced surface stress based on atomic or molecular interaction is proposed in [16]. They tested its model with mercury adsorption on gold-coated microcantilevers. They also stated that total energy is the sum of the atomic (or molecular) interactive potential of the adsorbant plus elastic energy. Lastly, they find the beam deflection by minimizing the total potential energy expression in terms of beam curvature.

The surface stress involved in adsorption-induced stress is often calculated by Stoney's equation [50]. What Stoney observed was that glass plates bent form the attachment of metallic films onto the surface of glass. He concluded that the metallic films are

deposed under tension and that tension in the attached film could be determined from measurements of transverse deflections of beams. Therefore, from classic theory of beams mechanics he showed that

$$Pt = \frac{Ed^2}{6r} \tag{3.1}$$

where P is the tension force per unit cross-sectional area of the film (normal stress), t is the thickness of film; estimated by weighing beam before and after film attachment, E is the modulus of elasticity, d is the thickness of beam, and r is the radius of curvature of the microcantilever beam. Therefore, the magnitude of the normal stress in the film can easily be related to beam deflection, depending on boundary conditions of the beam.

But, equation (3.1) was recently refined to recognize the biaxial state of stress in beams [16], for this case, the relation between stress and curvature is depicted by

$$\sigma = \frac{Et^2}{6R(1-\nu^2)} \tag{3.2}$$

where σ is typically called stress, it is actually force per unit length. t is the thickness of the microcantilever, ν is the Poisson's ratio, and R is the curvature radius. Otherwise, the earlier equation would not be dimensionally. The stress involved in this formula is shear or interfacial stress and not normal stress as in equation (3.1). Consequently, this formula is used to relate surface free energy and surface tension to beam curvature deflection.

In addition, using the first law of thermodynamic and differential calculus, Shuttleworth [51] shows that the surface stress σ and surface free energy γ can be interrelated

$$\sigma = \gamma + A\frac{\partial \gamma}{\partial A} \tag{3.3}$$

where γ is surface free energy and A is surface area. The difficulty of using this equation on microcantilevers rely on the fact that $\partial\gamma/\partial A$ depends on beam curvature, which is an unknown. Both the Stoney and Shuttleworth equations (3.1) and (3.3) must be solved simmultaneously to obtain σ and R.

The proposed model is based on energy potential in the first layer of atoms attached to one surface of a microcantilver and elastic potential in the microcantilever itself. Atoms are located against the microcantilever surface as shown in Figure 3.4. The first atomic layer on the beams surface has the dominate role in microcantilever deflections and this is supported by the experimental works of [52], who measured changes in curvature in

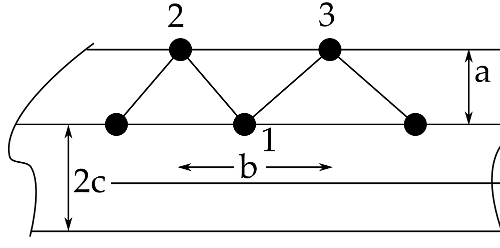

Figure 3.4: Arrangement of small molecules on microcantilever surface.

microcantilevered-thin plates due to adsorption of submonolayer of different atoms in ultrahigh vacuum conditions.

According to their model, atoms in the attached film are attracted and repulsed governing to the Lennard-Jones potential expression:

$$w(r) = \frac{-A}{r^6} + \frac{B}{r^{12}} \tag{3.4}$$

where r is the gap between atoms or molecules. A part of this potential is transferred into the cantilever as elastic strain energy causing the beam to deflect. Therefore, the equilibrium configuration of the microcantilever is determined by minimizing the total potential function, which is made up of the Lennard-Jones potential and elastic energy in the microcantilever. Both potential components will now be expressions in terms of the local curvature of the beam.

Figure 3.5 shows the curvature of the beam over a distance, b, which is taken as the atomic space between two atoms on the surface of the beam. Three atoms are involved on the atomic potential expression. It is assumed that the adsorbate distribution is uniform over the surface since the surface is chemically homogeneous. Since the distribution of surface atoms i assumed to be uniform, the curvature will be uniform along the microcantilever. The curvature can be established by considering the elastic energy in the beam over the length, d, and the atomic potential between the three atoms, one on the microcantilever surface and two in the attached film or coating [16].

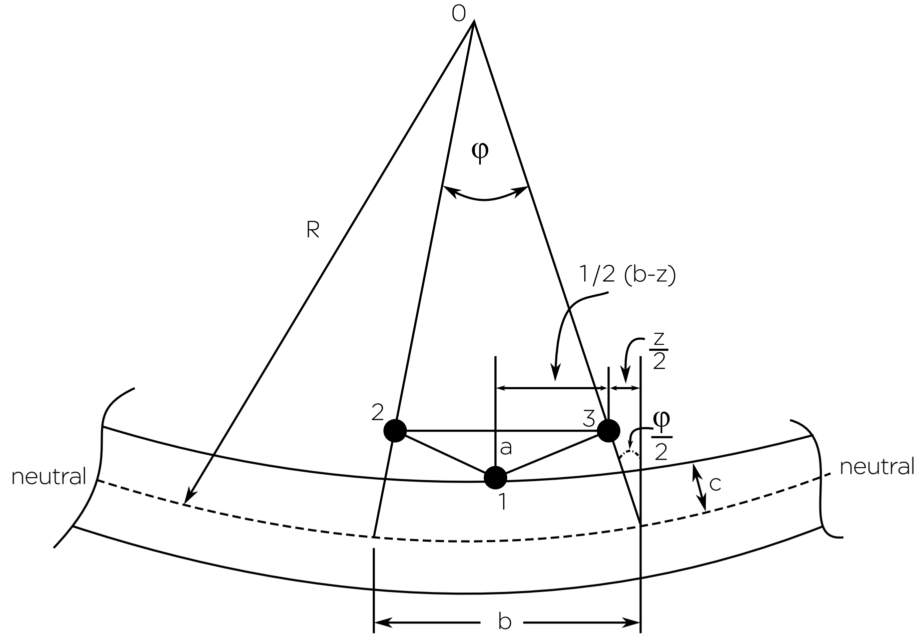

Figure 3.5: Position of surface atoms on deflected beam

Other assumptions made are typical of those used in beam theory, for instance, a cross-sectional plane before bending remains a plane after bending. In addition, the near surface layer of atoms, 2 and 3 see Figure 3.5 also remain in the same plane after beam deformation. Thus, the energy potential in the near surface layer of atoms can be expressed in terms of beam curvature. The movement of molecule 2 toward 3 is

$$z = \varphi(c + a), \tag{3.5}$$

$$b = R\varphi, \tag{3.6}$$

hence

$$z = \frac{b}{R}(c + a) \tag{3.7}$$

Atomic potential, U_s, in terms of beam curvature $(1/R)$ according to the Lennard-Jones expression is

$$U_s = \frac{-A}{(b-z)^6} + \frac{B}{(b-z)^{12}} + 2\left\{ \frac{-A}{\left[\frac{1}{4}(b-z)^2 + a^2\right]^3} + \frac{B}{\left[\frac{1}{4}(b-z)^2 + a^2\right]^6} \right\} \tag{3.8}$$

The resulting equation is

$$
\begin{aligned}
\frac{EI}{c^2}\left(\frac{c}{R}\right) =& \frac{\frac{A}{b^7}6\left(1+\frac{a}{c}\right)}{\left[1-\frac{c}{R}\left(1+\frac{a}{c}\right)\right]^7} - \frac{\frac{B}{b^{13}}12\left(1+\frac{a}{c}\right)}{\left[1-\frac{c}{R}\left(1+\frac{a}{c}\right)\right]^{13}} \\
&+ 2\left\{\frac{\frac{A}{b^7}\frac{3}{2}\left[1-\frac{c}{R}\left(1+\frac{a}{c}\right)\right]\left(1+\frac{a}{c}\right)}{\left[\frac{1}{4}\left[1-\frac{c}{R}\left(1+\frac{a}{c}\right)\right]^2+\left(\frac{a}{b}\right)^2\right]^4}\right. \\
&\left. - \frac{\frac{B}{b^{13}}3\left[1-\frac{c}{R}\left(1+\frac{a}{c}\right)\right]\left(1+\frac{a}{c}\right)}{\left[\frac{1}{4}\left[1-\frac{c}{R}\left(1+\frac{a}{c}\right)\right]^2+\left(\frac{a}{b}\right)^2\right]^7}\right\}
\end{aligned}
\tag{3.9}
$$

The values of c/R, which satisfy this expression, define the curvature of the microcantilever beam. To summarize, the proposed model takes into account the intermolecular interaction force between the adsorbed atoms and the substrate atoms.

3.1.2 Responses of Microcantilever Sensor Depending of Coatings

Microcantilevers intended for use as chemical sensors are typically modified so that one of the sides is relatively passive while other side exhibits high affinity to the targeted analyte. In order to understand how different modifying coatings provide responses of microcantilever sensors in the static bending mode, Lavrik et al. [48] have proposed the three distinctive models. The first model is most adequate when interactions between the microcantilever and its environment are predominantly surface phenomena, the second model of analyte-induced stresses is applicable for a microcantilever modified with a much thicker than a monolayer analyte-permeable coating, and the third model is most relevant to nanostructured interfaces and coatings, such as surface-immobilized colloids.

3.1.2.1 Interactions Around Microcantilever

Adsorption of analyte species on transducer surfaces may involve physisorption (weak bonding, binding energy < 0.1 eV) or chemisorption (stronger bonding, binding energy > 0.3 eV). Physisorption is associated with van der Waals interactions between the adsorbate and the adsorbent substrate. The analyte species can polarize the surface creating induced dipoles at the time they approach the surface. The resulting interactions are associated with binding energies less than 0.1 eV. While on chemical bonding between the analyte and the surface in the case of chemisorption, much higher binding energies are characteristic.

In overall, changes in surface stresses can be attributed to changes in Gibbs free energy associated with adsorption processes. For instance, Figure 3.6 shows chemisortpion of

straight-chain thiol molecules on a gold coated microcantilever. Surfaces usually tend to expand as a result of adsorptive processes. A compressive stress is referring to a posibility of return of the surface into the original compressed state.

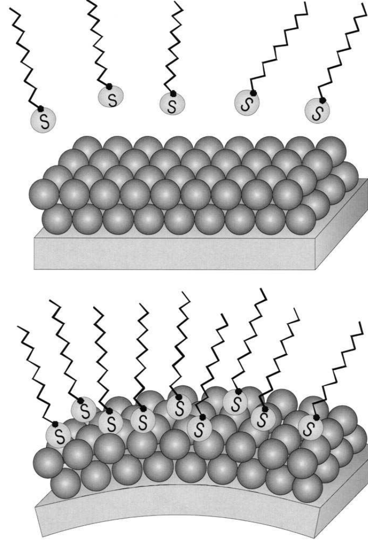

Figure 3.6: Depiction of chemisorption on straight-chain thiol molecules on a gold coated microcantilever [48]

In many cases, adsorbate-induced deformations of thin plates can be accurately predicted using a modification of the relationships derived by Stoney and von Preissig [50].

$$\frac{1}{R} = \frac{6\,(1-\nu)}{Et^2}\Delta\sigma, \tag{3.10}$$

Where R is the radius of microcantilever curvature, ν and E are Poisson's ratio and Young's modulus for the substrate respectively, t is the thickness of the microcantilever, and $\Delta\sigma$ is the differential surface stress. Therefore, knowledge of the radius of curvature R allows the tip displacement of a microcantilever with length l tip to be determined by

$$\Delta z = \frac{1}{2}\frac{l^2}{R} = \frac{3l^2(1-\nu)}{Et^2}\Delta\sigma \tag{3.11}$$

When adsorbate-induced stresses are generated on ideal smooth surfaces or within coatings that are very thin in comparison to the cantilever.

3.1.2.2 Surface with Analyte-Permeable Coating

The second of the three models that propose Lavrik et al. [48] is applicable for a microcantilever modified with a much thicker than a monolayer analyte-permeable coating.

Taking into account interactions of the analyte molecules with the bulk of the responsive phase, a predominant mechanism of microcantilever deflection can be described as deformation due to analyte-induced swelling of the coating (see Figure 3.7). Those swelling processes can be quantified using approaches developed in colloidal and polymer science. By evaluating molecular forces acting in the coating and between the coating and the analyte species. Depending on whether it is more appropriate to describe the responsive phase as solid or gel-like, these altered forces can be put into accordance with, respectively, stress or pressure changes inside the coating.

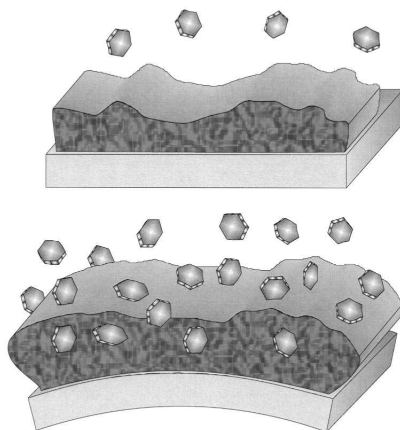

Figure 3.7: Depiction of analyte-induced microcantilever deformation when the surface is modified with a thicker analyte-permeable coating [48]

It is important to note that the magnitude of apparent surface stress scales up in proportion with the thickness of the responsive phase. Using the Stoney's model, an estimate deflection of a microcantilever coated with thin, soft, responsive films can be performed.

3.1.2.3 Nanostructured Interfaces and Coatings

This model involves nanostructured interfaces and coatings, such as surface-immobilized colloids. It is deserving to note that grain boundaries, voids, and impurities have been long known as being responsible for high intrinsic stresses in disordered, amorphous, and polycrystalline films. The combination of these mechanisms facilitates efficient conversion of the energy of receptor-analyte interactions into mechanical energy of cantilever bending. Recent studies demonstrated that up to two orders of magnitude increases in microcantilever responses can be obtained when receptor molecules are immobilized on nanostructured instead of smooth gold surfaces [48]. The Figure 3.8 depicts a microcantilever deformation in the case of a structured modifying phase.

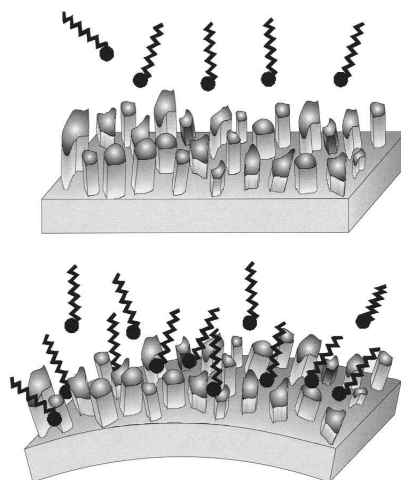

Figure 3.8: Depiction of analyte-induced microcantilever deformation when the surface is modified with structured phases combine mechanisms of bulk, surface, and intersurface interactions [48].

Moreover, nanostructured responsive phases offer an approach to substantially increase the number of binding sites per microcantilever without compromising their accessibility for the analyte. In other words, many of these nanostructures phases exhibit behaviors of molecular sponges.

3.1.3 Modeling Adsorption Onto a Surface

Mathad et al. [49] studied the origin, cause and factors influencing surface stress, experienced by a microcantilever beam. The adsorption based biosensor experiences surface stress caused by surface reconstruction, substrate mediated interaction, charge density redistribution and intermolecular repulsive forces. On their work, the surface stress developed, is calculated by applying the Stoney equation. One constraint their had, the deflection of the beam should not exceed half the thickness value, to maintain accuracy of Stoney equation and avoid nonlinearity. One of their conclusions is that the surface free energy technique of measuring surface stress is best suited due its non dependance on material properties.

The four important factors that they discussed are the surface reconstruction, intermolecular forces, interaction energies, coverage of the adsorbate and the molecular mass of adsorbate. Those four factors will be mentioned on following sections.

3.1.3.1 Surface Reconstruction

The adsorption of foreign atoms upon crystal surfaces has been studied by the diffraction of low-energy electrons [47]. Altogether, a tensile surface stress acts in a clean metal

surface. Therefore any adsorption onto a surface changes the surface forces acting in the surface layer. Adsorption leads to reduced coordination of surface atoms due to absence of bonding partners on the surface. Consequently, this causes a peculiar redistribution of the electronic charge at the surface. The shift in electronic charge at the surface causes change in acting surface forces on the bulk, leading to the observed surface reconstruction [49]. When the adsorption occurs, the surface undergoes changes, forming the X (2x2) structure (see Figure 3.9(a)) or the missing row reconstruction (see Figure 3.9 (b)). To sum up, the stress change associated with missing row reconstruction is smaller than stress change associated with the X (2x2) structure formation.

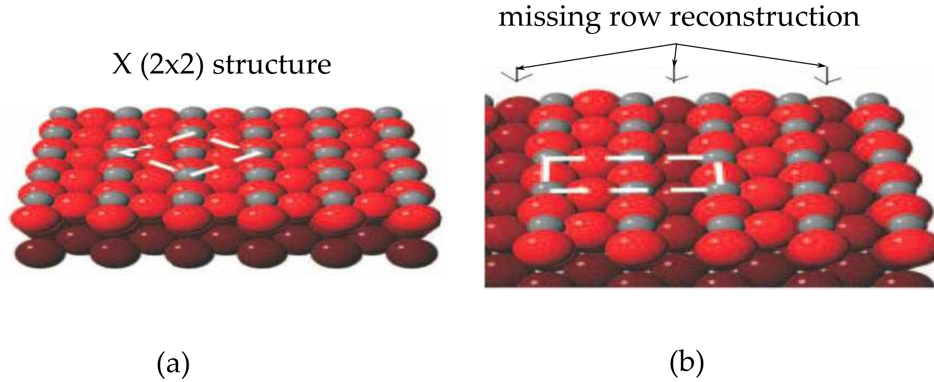

Figure 3.9: (a) The X (2x2) structure, (b) The missing row reconstruction [49]

3.1.3.2 Interaction Energy

In this model, also are considered intermolecular forces. Surface stress is caused due to the contribution of interaction energies in adsorption layer with the derivatives and because of the configuration entropy [49]. Intermolecular interactions such as atractive (van der Waals) and repulsion (Pauli exclusion) described by the Lennard-Jones potential, resulting in a surface stress, are also considered [21].

The interaction energy is influenced by the electrostatic energy among adions, induction energy, van der Waal's attraction and Pauli's repulsion, many body interactions within adjacent layers and the substrate mediated interaction energy. Mathad et al. [49] noted that substrate mediated interaction energy and energy among adions are very dominant. The substrate mediated interaction energy is very large and for lower coverage configuration the surface stress. Surface stress is generated due to the intermolecular repulsive forces [49]. When adsorption there is a change in the surface free energy (also called Gibbs energy) ΔG, which is related to change in surface stress as $\Delta\sigma$.

$$\Delta\sigma = \frac{\Delta G \cdot X}{M} \tag{3.12}$$

Where X is the molecule mass per unit area and M is the molar mass. Immobilization and Hybridization are the causes for the developed intermolecular forces.

3.1.3.3 Coverage of the Adsorbate

The influence that coverage of adsorbate has on the surface reconstruction and change in interaction energy, resulting in surface stress. If it considered coverage (Θ) as

$$\Theta = \frac{Na}{Ns} \tag{3.13}$$

where Na is the adsorbate mass and Ns is the substrate mass. The variation of surface stress with coverage varies from adsorbate to adsorbate. The coverage influences the type of surface reconstruction [53]. What they have inferred is that surface stress depends on coverage for example, it depends on the mass of the adsorbate. However, the mass of the adsorbate depends on the molecular size. Thus, molecular size of the adsorbate influences the amount of change in surface stress on the micro-cantilever beam substrate.

3.1.3.4 Adsorption Kinetics

The Langmuir adsorption model is used to quantify the amount of adsorbate adsorbed on an adsorbent as a function of partial pressure or concentration at a given temperature. Langmuir related coverage to the concentration of the adsrobate by the formula,

$$\Theta = \frac{\alpha P}{1 + \alpha P} \tag{3.14}$$

Where P is the concentration of the adsorbate, α is the proportionality constant. This helps us add a new dimension to the study of origin of surface stress. Thus, the time dependence on the layer formation is modeled by the Langmuir isotherm. According with Mathad et al. [49], the use of the obtained rate constant to find the surface free energy and in turn the change in surface stress is well established by the following equations,

$$\Delta G = -RTln(Ke) \tag{3.15}$$

where,

$$Ke = \frac{Kads}{Kdes} \tag{3.16}$$

here, R is the gas constant and T is the ambient temperature. $Kads$ is the rate constant of adsorption and $Kdes$ is the rate constant of desorption. Concluding, change in surface stress is calculated using the expression,

$$\Delta\sigma = \frac{\Delta G \cdot X}{M} \tag{3.17}$$

3.1.3.5 Electrostatic Interactions

Electrostatic repulsion between the adsorbed molecules has been proposed as a possible source of the observed surface stress, according with [21]. They have worked in a alkanethiol self-assembled monolayer (SAM) on a gold-coated microcantilever. They stated that when a complete SAM is formed on a gold surface, a series of adjacent dipoles are pinned to the surface, all repelling each other through Columbic interactions. Therefore, the electrostatic energy contribution to the surface stress can be evaluated in a rather simplistic model where the electrostatic energy us summed over all Au^+S^- bonds. This total electrostatic energy, E_{es-tot}, is counterbalanced by a restoring elastic energy, $E_{cantilever}$, resulting from the bent surface of the cantilever. Lastly, minimization of the sum of these two energy contributions yields an equilibrium intermolecular separation, which can be converted and interpreted as a surface stress.

3.1.3.6 Surface Charge Redistribution

Godin et al. [21], proposed that changes in the electronic charge density at the gold surface can account for the generation of large surface stresses. In other words, one can consider the effect of cleavage of noble metal surface on the surface stress. When a clean metal surface is created since the electronic charge density surrounding surface atoms is different than that surrounding bulk atoms, a tensile surface stress results. They also mentioned that the loss of bonds at the newly formed surface triggers an electronic redistribution which causes an increased charge density between the top surface atoms, suddenly observed as a tensile surface stress resulting from the increase in the attractive interaction between surface atoms.

At this point, we have presented the most relevant methodologies to characterize and describe the origin of surface stress due to adsorption on microcantilever-based sensors. However, not only that kind of stress is present in a composite beam. The next section will be focused on the introduction of residual stress characterization of MEMS materials, mainly on one of the contributions of this thesis work; a nondestructive and independent-of-fabrication-processes method proposed to characterize it.

3.2 Cantilever Deflection Associated to Residual Stress

Structures that are fabricated of more than one material are called composite structures or multilayer structures. A multilayer structure can be studied as an anisotropic material, the reason is some of its effective material properties, such as electrical, mechanical and thermal properties, depend on the direction considered [54].

Regardless of the origin of the stresses, these may be tensile ($\sigma > 0$), it kind of stress tend to contract the length of the materials, or compressive ($\sigma < 0$) where it stress tend to expand the structure. Residual stresses are classified as thermal and non-thermal (intrinsic) parts, as discussed below.

Intrinsic Stresses: Generally, intrinsic stresses of thin film can be further classified according to its formation mechanisms. Notwithstanding, all of those mechanisms have a common feature, that is all of them change normal spacing between atoms or molecules and as consequence generate microscopic strains and thus stresses. For mentioning some formation mechanisms, a) Stress generation during coalescence of crystallites, b) grain growth, c) excess vacancy annihilation, d) impurity and inclusions effects, and e) lattice mismatch.

Extrinsic Stresses: Are caused by external factors such as packaging or actuation.

Residual stresses can be defined as those stresses that remain in a material or body after manufacturing and processing in the absence of external forces or thermal gradients. In general there are three kinds of residual stress: a) Macroscopic, is long range in nature, extending over at least several grains of the material, and usually many more. b) Structural microstress, covers a distance of one grain or a part of a grain and it can occur between different phases and have different physical characteristics. c) Grain-related stress, this kind of residual stress range over several atomic distance within a grain, and is equilibrated over a small part of the grain.

Residual stress occurs in materials and mechanical components during manufacturing from many film growth processes. Residual stresses are often a result of manufacturing processes that produce non-uniform elastic or plastic deformation. A residual stress field is normally created during the growth process and can result in the unwanted deformation or failure of the structures released.

The figure 3.10 consists in a structure of N different elastic material layers, each one denoted by index i and with unique thickness and material properties. The thickness of the whole structure is t and its length and width are L and W, respectively.

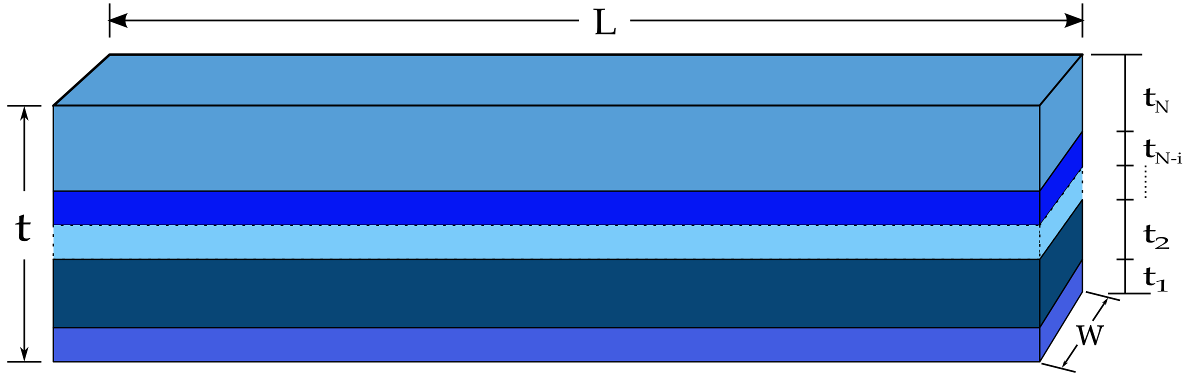

Figure 3.10: Geometry of a multilayer beam

Considering an elastic structure, such as the beam proposed in figure 3.10, its deflection curve describes the deformation profile along its longitudinal axis as a result of applied loads. Since multimorphs employ two or more thin-films layers, they tend to curl upon release from the substrate due to different residual stresses of each layer.

Multimorph cantilevers have been analyzed by analytical and numerical techniques. Analytical models typically utilize the approach based on Tomoshenko's thermal bimorph analysis, theoretical evaluation of bimetal thermostats reported by Timoshenko [55] provided an analytical expression for the radius of curvature of a bimetal cantilever as a function of a temperature change. The deformation resulting from unequal thermal expansion of each layer has been used extensively as an operation principle of thermostats and often referred to as the bimetallic effect.

The approach based on Timoshenko's thermal bimorph analysis [55] includes 1) strain continuity between two neighboring layers at their interface, 2) balance of forces and moments at static equilibrium, and 3) formulation of the radius of curvature and tip deflection. Feng and Liu [56] presented generalized formulas for the radius of curvature and layer stresses caused by thermal strains in semiconductor multimorphs . DeVoe and Pisano [57] developed a multimorph model for piezoelectric cantilever microactuators, which is applicable to thin-film devices composed of an arbitrary number of layers.

According to the Euler-Bernoulli beam theory, when a linear and isotropic elastic beam is subjected to a pure bending moment M, for example when the shear force acting on the beam is equal to zero, it is known that axial lines bend to form circumferential lines and transverse lines remain straight and become radial lines as the figure 3.11 shows. Therefore, a neutral surface must exist that is parallel to the top and bottom surfaces of the beam and for which the length does not change.

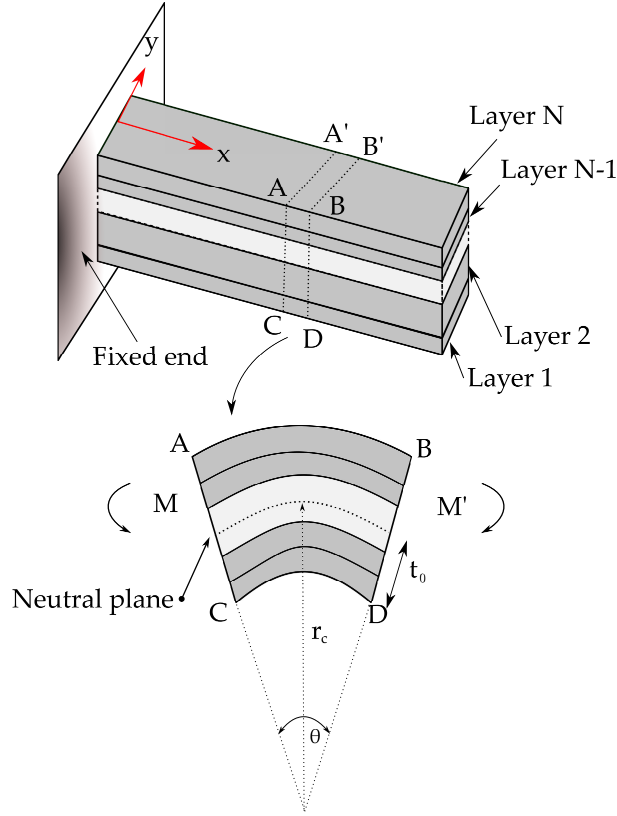

Figure 3.11: View of the plane of symmetry of a linear, isotropic elastic beam

Some assumptions are considered in the model: a) the subscript i represents the index for a layer, b) the material of each layer remains linearly elastic, c) two consecutive layers are perfectly bonded at their interface, d) the length of multimorph beam is much larger than its thickness ($L > 6t$)[58], e) the thickness of the multimorph beam is much smaller than the radius of curvature r_c induced by the combined effect of all stresses. Then, this radius is approximately equal for all layers and given by

$$\frac{1}{r_c} = \frac{M_i}{E_i I_i} \tag{3.18}$$

where M_i is the individual bending moment and $E_i I_i$ is the flexural rigidity relative to the multimorph's neutral axis. Then, the equation (3.18) can be applied to composite beam too since, as in one-material beams, the assumption that their cross section remain plane during pure bending is also valid.

The position of the neutral surface t_0 in a layered composite beam under in-plane loadings can be obtained as the modulus-weighted centroid of the cantilever [59], that position is described by

$$t_0 = \frac{\sum_{i=1}^{N} \int_{A_i} E_i z dA_i}{\sum_{i=1}^{N} \int_{A_i} E_i dA_i} \tag{3.19}$$

where E_i and A_i are the elastic modulus and corss section of the ith material layer, N is the number of composing material layers and z is the out-of-plane coordinate with respect to the neutral surface.

The effective flexural rigidity of a layered composite beam under to in-plane loadings can be described as the summation of the flexural rigidity of each material layer and is expressed as

$$EI = \sum_{i=1}^{N} E_i I_i = \sum_{i=1}^{N} \int_{A_i} E_i z^2 dA_i \tag{3.20}$$

where I_i is the moment of inertia of the ith cross-sectional area with respect to the y axis. The stress-induced bending moment about the neutral surface of a multilayers cantilever is given by

$$M_y = \sum_{i=1}^{N} \int_{A_i} \sigma_i z dA_i \tag{3.21}$$

where σ_i represents the normal stress acting over the cross section of the ith material layer and z is the out-of-plane coordinate across the thickness of the multilayered cantilever, with an origin chosen at its neutral surface.

3.2.1 Proposed Method to Characterize Residual Stress

Residual stress can affect the performance of thin-film micromachined structures and lead to distortion in the frequency of resonant as well as an initial state of curling in cantilevers. As the origin of residual stress is dependent on the fabrication processes, a method for characterization of residual stress, being independent of processes conditions and nondestructive, is crucial to provide a rapid way to effectively design microcantilever-based microsystems.

In this section we present an analytical model that characterizes the residual stress within composite microcantilever beams towards predicting its initial deflection profile. The model relies on the contribution of a linear gradient stress and the approach of a quadratic deflection profile due to residual stress within a composite microcantilever such as the case of our sensing platform.

According to the definition of plane stress [60], it is defined to be a state of stress in which the normal stress, σ_z, and the shear stresses, σ_{xz} and σ_{yz}, directed perpendicular to the $x - y$ plane are assumed to be zero. Furthermore, the geometry of the body is essentially that of a plate with one dimension much smaller than the others. The loads are applied uniformly over the thickness of the plate and act in the plane of the plate as shown Figure 3.12. This plane stress condition is the simplest form of behavior for continuous structures and represents situations frequently encountered in practice.

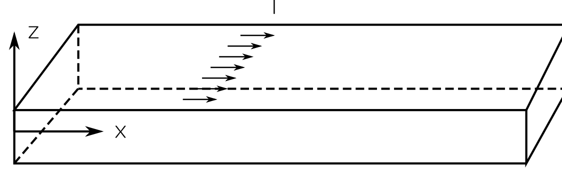

Figure 3.12: Plane stress condition

Based on that plane stress condition, we consider that,

$$\sigma_z = \tau_{xz} = \tau_{yz} = 0 \tag{3.22}$$

According with the constrains described by the plane stress condition, it is the appropriate condition for the microcantilever modeling, consequently, the tensor stress has the form,

$$S_0 = \begin{pmatrix} \sigma_{1,max} \cdot \left(\frac{z}{t_0}\right) & 0 & 0 \\ 0 & \sigma_{1,max} \cdot \left(\frac{z}{t_0}\right) & 0 \\ 0 & 0 & 0 \end{pmatrix} \tag{3.23}$$

Where, $\sigma_{1,max}$ is the maximum linear gradient stress value experienced by the microcantilever, z is the coordinate along the thickness of the structure, and t_0 represents the position of the neutral surface stress in the whole structure. Now, Equation (3.23) is consistent with the plane stress condition.

According with Fang's methodology, the residual stress within a homogeneous thin film is modeled as an uniaxial field, which is expressed by the mth degree polynomial,

$$\sigma_{total}(z) = \sum_{m=0}^{\infty} \sigma_{m0} \left(\frac{z}{t/2}\right)^m, \quad for \quad -t/2 \leq z \leq t/2, \tag{3.24}$$

where σ_{total} is the linear superposition of the fundamental states of residual stress (σ_m), σ_{m0} is a maximum stress value and z is the out-of-plane coordinate across the thickness t of the film, with an origin chosen at the film's mid-plane, for instance $z = 0$.

Now, using the first approximation ($m = 1$) we can express (3.24) as,

$$\sigma_{total}(z) = \sigma_{00} + \sigma_{10}\left(\frac{z}{t/2}\right) \tag{3.25}$$

where σ_{00} is a constant mean stress and $\sigma_{10}(2z/t)$ is a linear gradient stress, the former being symmetric and the latter anti-symmetric, about the mid-plane of the cantilever beam.

From [61], the flexural formula for a homogeneous microcantilever beam is

$$\sigma_{1,max} = E \cdot \kappa \cdot \frac{t}{2} \tag{3.26}$$

where E depicts the Young's modulus, $t/2$ represents the position of neutral plane of homogeneous cantilever beam, and κ is the curvature component due to gradient stress.

From Fang's methodology, is stated that the curve of a cantilever beam subjected to a residual stress fiedl given by (3.25) can be decomposed into rotation and curvature components that derive independently from σ_{00} and σ_{10}. According with model described by Camacho in [1], the curvature component originates from a sensibly constant bending moment along the length of the cantilever. The bending moment tends to produce a quadratic deflection profile of the cantilever beam. Therefore, there are defined a rotation and curvature components due to gradient (σ_1) stress; the deflection curve of a homogeneous cantilever beam can be expressed as

$$\omega(x) = \frac{\kappa_{\sigma_1}}{2}x^2 + \theta_{\sigma_1}x, \quad for \;\; 0 \leq x \leq L \tag{3.27}$$

where x is the coordinate across the length L of the cantilever beam.

The coefficients $\kappa_{\sigma_1}/2$ and θ_{σ_1} are obtained by a fit of the measured deflection curve to (3.27). Also, the maximum gradient stress is obtained from the flexure formula (3.26) and the rotation component, θ_{σ_1} is obtained from the parametric analysis model [62]

$$\theta_{\sigma_1} = \frac{\sigma_{10}}{E}(0.0086t^2 - 0.047t + 0.81) \tag{3.28}$$

Considering experimental results proposed by Camacho [1], where are presented fitted curves governed by the second degree polynomial

$$\omega(x) = a_2x^2 + a_1x + a_0, \quad for \;\; 0 \leq x \leq L_j \tag{3.29}$$

where a_0, a_1, and a_2 are constant coefficients to be determined; L_j is the measured length of the jth cantilever beam.

Now, after analyzing (3.27) and (3.29) it is possible to write that

$$a_2 = \frac{\kappa_{\sigma_1}}{2}, a_1 = \theta_{\sigma_1}, a_0 = 0 \tag{3.30}$$

Note that the independent term is approximately equal to zero due to the boundary condition of zero displacement at the base of the cantilever beam.

About our method proposed in this thesis work, the model methodology comprises first, measuring the surface curvature profile of the structures by white-light interferometry, then, extracting its curvature component, later computing linear gradient stress by using a parametric analysis, and finally, analytical and experimental results are compared.

Using Equation (3.26) where is considered a homogeneous cantilever, we assume a composite cantilever beam and a small angle approximation, then, using the average of the Young's modulus as following

$$\overline{E} = \frac{E_1 t_1 + E_2 t_2 + E_3 t_3 + ... + E_n t_n}{t_{total}} \tag{3.31}$$

where the subscript n is the nth layer of the composite cantilever beam, and t_{total} depicts the total thickness of the cantilever beam. Therefore, using (3.31) and (3.26) we have a gradient stress as

$$\sigma_{1,max} = \overline{E} \cdot \kappa_{\sigma_1} \cdot t_0 \tag{3.32}$$

now, using Equation (3.30) by substituting the quadratic coefficient we can write for the new stress gradient as following

$$\sigma_{1,max} = \overline{E} \cdot 2a_2 \cdot t_0 \tag{3.33}$$

So far, we have a theoretical expression to estimate the gradient stress $\sigma_{1,max}$ using Equation (3.33). However, in order to use it, it is necessary to know previously the term a_2. This coefficient it is well approximated by the radius curvature of the cantilever beam, measuring the deflection by white-light interferometry and invoking Equation (3.18) as is made in Camacho's experiments. In next chapter will be applied this method and will be compared the experimental results face to analytical results. Nonetheless, next section will introduce the theoretical framework surrounding polysilicon piezoresistive sensing elements as the next step in schematic diagram presented in 2.2.

3.3 Polysilicon Piezoresistive Sensing Elements

Continuing with the stages within schematic diagram of stages 2.2 having our sensing platform. In this section is discussed the design principles of polysilicon piezoresistive sensing element.

Piezoresistive sensing elements are usually formed by a diffusion or ion-implantation layer in practical applications. The impurity concentration in the layer is laterally uniform (in x' -y' direction), but in the depth direction is no uniform. As the leakage current increases exponentially with temperature, a piezoresistive sensor may even fail to work when the temperature exceeds 100℃. Hence, for stable operation at a temperature from 100℃ to 300℃, materials with a layer of crystalline silicon on an insulator substrate (SOI) have been developed for piezoresistive sensing elements [63].

A low cost alternative to single crystalline silicon SOI material is a polysilicon layer deposited on a SiO_2/Si substrate.

3.3.1 Piezoresistance Effect in Polysilicon

Polysilicon layer consists of a large amount of crystalline silicon grains and some non-crystalline regions between the grains (the boundary regions). The orientation of the grains can be totally random, or, they may have one or a few preferential growth orientations in the normal direction (z'- direction) of the layer.

The boundary regions contain a large amount of trap centers. As there are very few free charge carriers in the region, it is virtually "non-conductive". The trap centers in the boundary regions cause a potential barrier between neighboring grains and cause depletion layers un the surface region of the grain.

The next figure represents a model for a polysilicon material, where the grains are assumed to be square in shape of the same size much smaller than the width of the resistor, but the grains are as high as the layer thickness. Also assumed is that the area occupied by a grain is a square with a dimension of a, and the conductive area of the grain has a dimension of βa ($\beta < 1$).

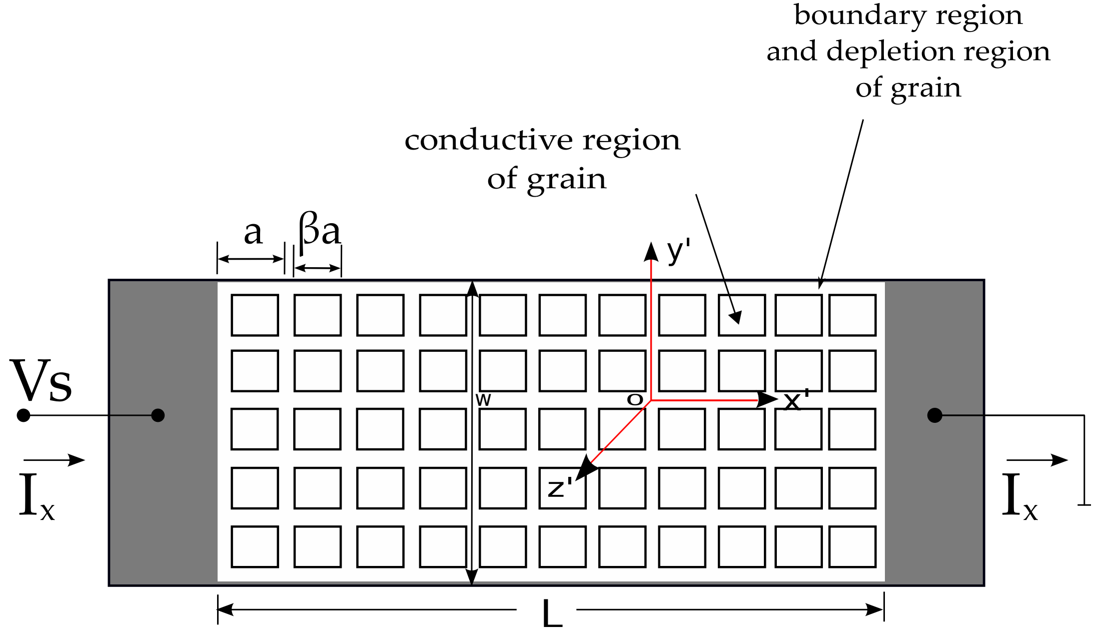

Figure 3.13: Simplified model for a polysilicon material

3.3.2 Polysilicon Piezoresistor

The resistance of a polysilicon piezoresistor, R, consists of two parts generally: one from conductive region of the grains, R_g, and the other from the boundary regions and the depletion layers of the grains, R_I. Hence, the total resistance is:

$$R = R_g + R_I \tag{3.34}$$

The relative change in resistance is

$$\frac{\Delta R}{R_0} = \frac{\Delta R_g + \Delta R_I}{R_{g0} + R_{I0}} \tag{3.35}$$

where subscript "0" denotes the original value when the material is not stressed. As R_I is dominated by tunneling mechanism, it depends on the distance between the conductive regions. Therefore, the piezoresistance effect is the dominant mechanism, equation (3.35) is approximated as

$$\frac{\Delta R}{R_0} = \frac{\Delta R_g}{R_{g0} + R_{I0}} \tag{3.36}$$

As the orientation of grain are random, leastways in two dimensions, the piezoresistance of the grains has to be found by taking an average over the directions as follows

$$\Delta R_g = R_{g0}(\overline{\pi}_l T_l + \overline{\pi}_t T_t + \overline{\pi}_s T_s) \tag{3.37}$$

Using equations (3.36) and (3.53), we have

$$\frac{\Delta R}{R_0} = \frac{(\overline{\pi}_l T_l + \overline{\pi}_t T_t + \overline{\pi}_s T_s)}{R_{g0} + R_{l0}} R_{g0} \tag{3.38}$$

Typical applications use a four-terminal sensing element, for a polysilicon four-terminal sensing element, the lateral electric field inside a grain is

$$E_Y = (\overline{\pi}_{61} T_l + \overline{\pi}_{62} T_t + \overline{\pi}_{66} T_s) E_X \tag{3.39}$$

Considering the model shown in figure 3.13, the electric field in the x-direction is written as

$$E_X = \frac{R_{g0} V_S}{R_{g0} + R_{I0}} \frac{1}{\beta L} \tag{3.40}$$

Where V_S is the supply voltage and L is the length of the resistor. Hence, we have

$$E_Y = \frac{V_S}{\beta L} \frac{R_{g0}}{R_{g0} + R_{I0}} (\overline{\pi}_{61} T_l + \overline{\pi}_{62} T_t + \overline{\pi}_{66} T_s) \tag{3.41}$$

Since the orientation of grain are random and the lateral electric field is induced only in the conductive regions of a grain, the transverse output voltage is

$$V_T = \beta W E_Y = V_S \frac{W}{L} \frac{R_{g0}}{R_{g0} + R_{I0}} \tag{3.42}$$

Where W is the width of the resistor. To analyze the components of the average piezoresistive coefficient $\overline{\pi}_{ij}$, is taken in count two conditions: (i) The grains have a specific growth orientation in their normal direction, (ii) The grains are completely random in orientation.

3.3.3 Average Piezoresistive Coefficient

In the polysilicon layer, the grains may have one or a few preferential growth orientation in the normal direction, however they are always random in the layer plane. What is more, the piezoresistance of a polysilicon sensing element is obtained by the average

piezoresistive coefficient of the grains. So, in this section we will first analyze the average piezoresistive coefficient of polysilicon layer for two important series of growth orientations and then the average piezoresistive coefficient of polysilicon layer with completely random growth orientation.

Speaking of average for specific orientations, the orientation can be described by two Euler's angles, ϕ and θ, with reference to the crystallographic coordinate system of the grain. Although all grains in the layer have the same Euler's angles ϕ and θ, the third Euler's angle, ψ, is random. Accordingly, the average of piezoresistive coefficient tensor component, $\overline{\pi}_{ij}$, can be found by taking the average for ψ in the range of 0° to 360°.

3.3.4 Growth Orientation of [k, 0, m] Plane

If the growth orientation of grains is in a (010) plane, the series of orientations are in the form of [k, 0, m]. For instance, some directions in the series are: [001], [102], [201] and [100] as the figure 3.14 shows. For these directions, the first two Euler's angles are $\phi = 0$ and $\theta = tan^{-1}(k/m)$ but tne third Euler's angle, ψ, is random for the grains.

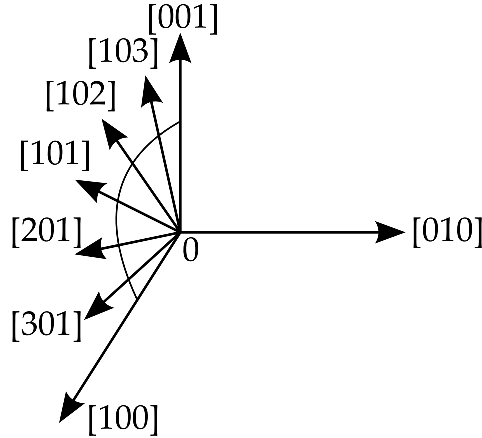

Figure 3.14: Some directions in (010) plane

Ê Using equation (A.23), the direction cosines of the resistor's coordinate system with respect to the crystallographic coordinate system of a grain are described by

$$\begin{pmatrix} l_1 & m_1 & n_1 \\ l_1 & m_2 & n_2 \\ l_3 & m_3 & n_3 \end{pmatrix} = \begin{pmatrix} cos\theta cos\psi & sin\psi & -sin\theta cos\psi \\ -cos\theta sin\psi & cos\psi & sin\theta sin\psi \\ sin\theta & 0 & cos\theta \end{pmatrix} \tag{3.43}$$

According with the equation (3.43) and using the table A.2, the results for some main directions are presented in table

$$\overline{\pi}'_{11} = \pi_{11} - 2\pi_0 \frac{1}{2\pi} \int_0^{2\pi} (l_1^2 m_1^2 + l_1^2 n_1^2 + m_1^2 n_1^2)\, d\psi = \pi_{11} - \frac{1}{4}\pi_0 (1 + 3cos^2\theta sin^2\theta) \quad (3.44)$$

Solving for other useful components

$$\pi'_{12} = \pi_{12} + \frac{1}{8}\pi_0(1 + cos^4\theta + sin^4\theta) \quad (3.45)$$
$$\pi'_{16} = \pi'_{61} = \pi'_{62} = 0 \quad (3.46)$$
$$\pi'_{66} = \pi_{44} + \frac{1}{4}\pi_0(1 + cos^4\theta + sin^4\theta) \quad (3.47)$$

Using the values of the table A.1 for the coefficients π_{11}, π_{12} and π_{44} in the expression of the table A.2, the results for some main directions are presented in table 3.2

Table 3.2: Coefficients of piezoresistivity matrix of polysilicon in (010) plane

		n-Si, $\pi(10^{-11}Pa^{-1})$			p-Si, $\pi(10^{-11}Pa^{-1})$		
directions	θ	$\overline{\pi}'_{11}$	$\overline{\pi}'_{12}$	$\overline{\pi}'_{66}$	$\overline{\pi}'_{11}$	$\overline{\pi}'_{12}$	$\overline{\pi}'_{66}$
[001]	0°	-66.7	18.0	-89.6	39.2	-33.7	72.9
[103]	18.35°	-57.1	21.1	-78.2	48.0	-30.8	78.8
[102]	26.57°	-49.7	23.7	-73.2	54.9	-28.5	83.3
[101]	45°	-40.1	26.8	-66.9	63.7	-25.6	89.2
[201]	63.34°	-49.7	23.7	-73.2	54.9	-28.5	83.3
[301]	71.57°	-57.1	21.1	-78.2	48.0	-30.8	78.8
[100]	90°	-66.7	18.0	-89.6	39.2	-33.7	72.9

3.3.5 Growth Orientations of [k, k, n] Plane

In a similar way, used in previous section, the analysis if the growth orientations of the grains are in the $(10\overline{1})$ plane, the Miller index of the orientation have the form $[k, k, n]$. For mentioning some main directions are [001], [113], [111], [331] and [110] as is presented in figure 3.15.

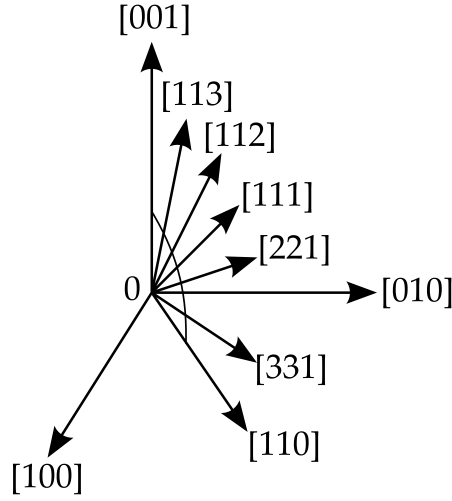

Figure 3.15: Some main directions in $(01\overline{1})$ plane

In this series of directions, the first two Euler's angles are $\phi = 45°$ and $\theta = tan^{-1}(\sqrt{2}k/n)$, but as the same case of the $[k, 0, m]$ plane, the third angle, ψ is random for the grains.

Thereupon, the direction cosines of the resistor's coordinate system with respect to the crystallographic coordinate system of a grain are denoted by

$$\begin{pmatrix} l_1 & m_1 & n_1 \\ l_1 & m_2 & n_2 \\ l_3 & m_3 & n_3 \end{pmatrix} = \begin{pmatrix} \frac{cos\theta cos\psi - sin\psi}{\sqrt{2}} & \frac{cos\theta cos\psi + sin\psi}{\sqrt{2}} & -sin\theta cos\psi \\ \frac{cos\psi - cos\theta sin\psi}{\sqrt{2}} & \frac{cos\psi - cos\theta sin\psi}{\sqrt{2}} & sin\theta sin\psi \\ sin\theta/\sqrt{2} & sin\theta/\sqrt{2} & cos\theta \end{pmatrix} \quad (3.48)$$

According with the equation (3.48) and table A.2, we can obtain some piezoresistive coefficients in rotated coordinate system.

$$\overline{\pi}'_{11} = \pi_{11} - \frac{1}{16}\pi_0(3 + 3cos^4\theta - 2coss^2\theta + 12cos^2\theta sin^2\theta + 4sin^2\theta) \quad (3.49)$$

$$\overline{\pi}'_{12} = \pi_{12} + \frac{1}{16}\pi_0(1 + cos^4\theta + 2cos^2\theta + 2sin^4\theta) \quad (3.50)$$

$$\overline{\pi}'_{66} = \pi_{44} + \frac{1}{8}\pi_0(1 + cos^4\theta + 2cos^2\theta + 2sin^4\theta) \quad (3.51)$$

$$\overline{\pi}'_{16} = \overline{\pi}'_{61} = \overline{\pi}'_{62} = 0 \quad (3.52)$$

Using the data of π_{11}, π_{12} and π_{44} from the table A.2 in order to obtain the non-zero components of the piezoresistivity matrix by in equation (3.48). The results are presented in table 3.3

Table 3.3: Coefficients of piezoresistivity matrix of polysilicon in $(10\overline{1})$ plane

		n-Si, $\pi(10^{-11}Pa^{-1})$			p-Si, $\pi(10^{-11}Pa^{-1})$		
directions	θ	$\overline{\pi}'_{11}$	$\overline{\pi}'_{12}$	$\overline{\pi}'_{66}$	$\overline{\pi}'_{11}$	$\overline{\pi}'_{12}$	$\overline{\pi}'_{66}$
[001]	0°	-66.7	18.0	-89.6	39.2	-33.7	72.9
[113]	25.24°	-50.0	23.5	-73.5	54.6	-38.6	83.1
[112]	35.26°	-40.1	26.8	-66.6	63.7	-25.5	98.1
[111]	54.74°	-31.2	29.7	-60.9	71.8	-22.6	94.6
[221]	70.53°	-35.1	28.4	-63.6	68.2	-24.0	92.2
[331]	76.74°	-37.5	27.6	-65.1	66.0	-24.7	90.7
[110]	90°	-40.1	26.8	-69.9	63.7	-25.5	89.1

3.3.6 Completely Random Distribution

Most of cases, there are too many preferential growth orientations for a polysilicon layer, so that none of them dominates, or, the preferential growth is not significant. For these cases, it could be convenient to use just the average results for a completely random distribution for design considerations. This average of components of piezoresistive coefficient for a completely random distribution can be found by taking the average over the whole space angle for three Euler's angles and it can be described as

$$\overline{\pi}_{ij} = \frac{1}{4\pi}\int_0^{2\pi} d\phi \int_0^{\pi} sin\theta d\theta \left(\frac{2}{2\pi}\int_0^{2\pi} \pi_{ij}(\phi,\theta,\psi)d\psi\right) \tag{3.53}$$

But calculating the non-zero components

$$\overline{\pi}'_{11} = \pi_{11} - \frac{2}{5}\pi_0 \tag{3.54}$$

$$\overline{\pi}'_{12} = \pi_{12} + \frac{1}{5}\pi_0 \tag{3.55}$$

$$\overline{\pi}'_{66} = \pi_{44} + \frac{2}{5}\pi_0 \tag{3.56}$$

In addition, using the data of π_{11}, π_{12} and π_{44} in table A.1, the averages are presented in table 3.4, note that the units of

In summary, they are many factors that affect sensitivity of a polysilicon sensor, the effect of piezoresistance does not cancel out by the random distribution of grain orientation. Lastly, this chapter will present the theoretical background involving read-out-circuit proposed and discussed on chapter 6; the BandGap Voltage Reference.

Table 3.4: Average of $\overline{\pi}_{11}$, $\overline{\pi}_{12}$, $\overline{\pi}_{66}$ considering a random distribution

Coefficient	Units	n-Si	p-Si
$\overline{\pi}'_{11}$	$(10^{-11}Pa^{-1})$	-45.4	58.8
$\overline{\pi}'_{12}$	$(10^{-11}Pa^{-1})$	25.0	-27.2
$\overline{\pi}'_{66}$	$(10^{-11}Pa^{-1})$	-70.4	85.9

3.4 Read-Out-Circuit

Using a Wheatstone bridge as a read-out-circuit, is ideally symmetric. The output of the bridge is zero when the resistors are not stressed. And, the output remains zero for any temperature since the four resistors have the same temperature coefficient of resistance. However, there are always some non-ideal factors that cause a non-zero output voltage for a Wheatstone bridge. Therefore, this original non-zero output is referred to as the offset voltage of the bridge.

Two main factor that cause offset voltage are: the geometric deviation of the resistors from their nominal value, and the stresses in the chip caused by the mismatch of thermal expansion coefficient between the silicon substrate and the deposited films on surface or the packaging materials [63].

In a Wheatstone bridge, considering that, $R_1 = R_2 = R_3 = R_4 = R_B$. If each resistor has a specific relative deviation from its nominal value, for instance, $R_1 = R_B(1 + \beta_1)$, $R_2 = R_B(1 + \beta_2)$, $R_3 = R_B(1 + \beta_3)$, and $R_4 = R_B(1 + \beta_4)$, as shown Figure **??**, the offset voltage of the bridge is

$$V_{offset} = V_{o1} - V_{o2} = V_s \cdot \frac{R_2R_3 - R_1R_4}{(R_1 + R_2) \cdot (R_3 + R_4)} = V_s\Big(\frac{\beta_1}{4} + \frac{\beta_2}{4} + \frac{\beta_3}{4} + \frac{\beta_4}{4}\Big) \quad (3.57)$$

where V_s is the supply voltage. Note that the contribution by the deviation of a specific resistor R_i is one fourth of its relative deviation β_i, and the effects of R_2, R_3, and R_1, R_1 are in the opposite directions. Hence, for the convenience further discussion, the circuit shown in Figure 3.16 (a), is reduced as the circuit shown in Figure 3.16 (b), where

$$\beta = (\beta_2 + \beta_3 - \beta_1 - \beta_4) \quad (3.58)$$

The offset voltage is $V_{os} = \beta V_s/4$. and for the sake of simplicity, β is assumed to be positive in value. Note, that the offset voltage shown in Figure 3.16 is not temperature dependent if all resistors have the same temperature coefficient. But, as part of the offset voltage is caused by the thermal stress, the offset is often temperature dependent.

But in a more critical case, the power supply is influenced by the temperature and it affects the Wheatstone bridge outcomes.

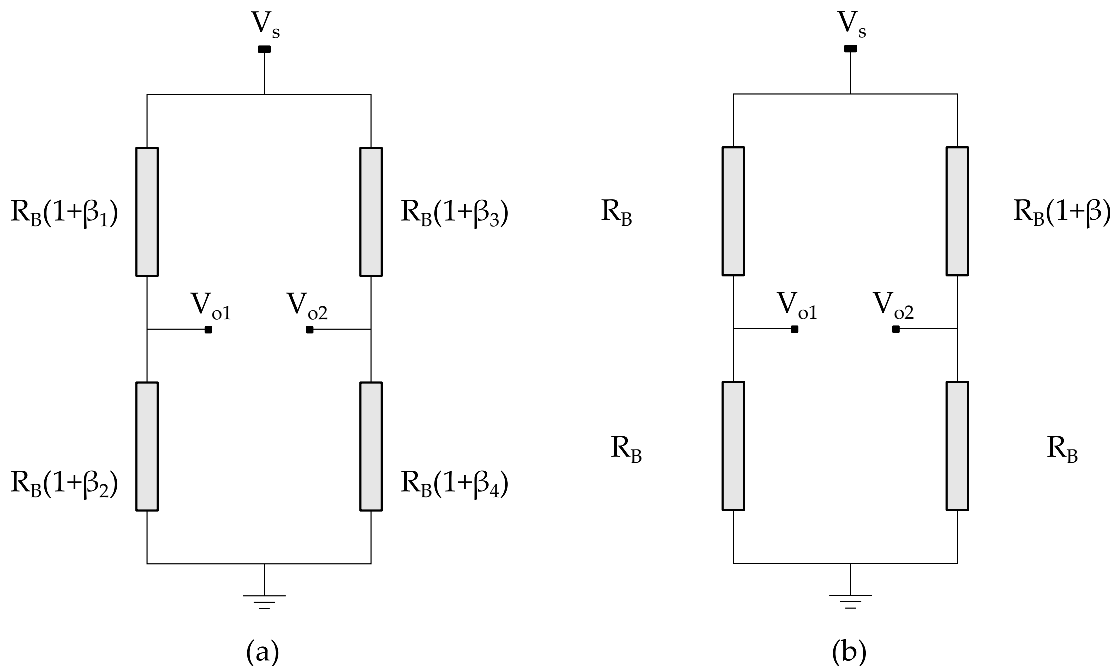

Figure 3.16: A piezoresistive bridge of resistors with deviations from nominal resistance

If all four resistors values and the supply voltage are known. The voltage across the bridge, (V_{out}) can be found by working out the voltage from each potential divider, then doing a subtraction between one from the other.

3.4.1 Bandgap References

In this section we will show how to design voltage references that are reasonably independent of both power supply and temperature. These references are typically called bandgap references [64]. The principle of temperature-independent references begins identifying a voltage that increases with temperature and a voltage that decreases with temperature. Figure 3.17, shows two voltages, one that increases proportionately with temperature and one that decreases proportionately with temperature.

The proportional to absolute temperature (PTAT) and the complementary to absolute temperature (CTAT) are shown. Multiplying by a temperature independent constant, K, the voltage with the smallest magnitude of slope and then both slopes are equal. The superposition of two voltages, finally provides an independent of temperature voltage $(V_{CTAT}(T) + K \cdot V_{PTAT}(T))$.

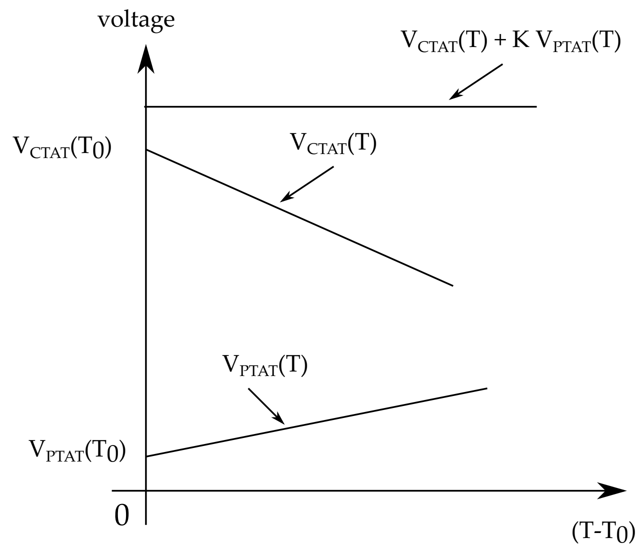

Figure 3.17: Voltages that increase and decrease with increasing temperature

In order to obtain the voltage independent of temperature, it is necessary to implement both voltages, $PTAT$ and $CTAT$. In a traditional bandgap reference, usually is strongly depending on the temperature coefficient of BJTs or semiconductor diodes, taking in account the $P-N$ junction.

Chapter 4

Modeling Cantilever-based Sensors

This chapter presents a comparison between experimental results for deflection in micromachined cantilever beams due to residual stress, and simulation results using a finite element analysis together with the analytical method of characterization for residual stress proposed in section 3.2.1.

Beam structures are widely used in MEMS sensors. However, from a fabrication perspective, MEMS microbeams are usually curled due to residual stress gradients, and this causes difficulties to accurately predict the microcantilever's behavior. Moreover, due to thermomechanical property mismatches for different materials and deposition-generated intrinsic stresses, thin-film MEMS structures such as bilayer microbeams usually exhibit a high residual stress, for the most part varying along the direction of thickness. Such a residual stress may alter the mechanical behavior of MEMS structures. And a zero mean residual stress does not necessarily imply a satisfactory situation. Once the film is released by a sacrificial etch, the mean residual stress vanishes, but the nonuniformity of the residual stress actually causes an out-of-plane deformation [65].

The deformation of MEMS structure usually results in a deterioration of device performance, therefore its control is a critical issue in developing many sensors and actuators. Tensile and compressive stressres contribute both to the bending of a cantilever. Real MEMS devices mostly have multilayered structures with different materials and complex geometries, therefore the modeling of their deformations would be practically difficult to implement [66]. One common effect of residual stresses is to introduce curvature on structures. Moreover, it is much more common for designers to view the problem from the other perspective; where they are designing a cantilever or beam, and need to predict how much bending will occur, either as a limit to the cantilever's usefulness, or to make use of the bending [67].

4.1 Simulating Residual Stress

As mentioned in section 3.2, residual stress within cantilever beams causes a de ection moment. Exemplary de ection curves are reported in [1] for a set of thirty test structures fabricated for residual stress characterization. The structures are basically microcantilever beams with di erent composition layers formed in a CMOS-MEMS fabrication process [68]. All these structures have a width of $W = 6\ \ m$ and a length of $L = 100\ \ m$.

Table 4.1 shows relevant physical data of the involved CMOS materials in the structures [1]. For analysis and design purposes, the CMOS materials are supposed to be linearly elastic below the yield stress, isotropic and homogeneous. Also, all material properties are supposed to be temperature independent.

The linear stress gradient e ect on these structures is analyzed by using FEM simulation in Comsol Multiphysics [69]. As shown in Figure 4.1, FEM analysis was implemented over a xed-free, composite layered model. Figure 4.2 depicts simulations results of the residual stress deformation performed in beams 2, 3, 4 and 5. This stress eld is described by a linear gradient stress, which is anti-symmetric about the neutral surface plane of the lm and collinear to the longitudinal coordinate of the cantilever beam. Furthermore, a plane stress approach is considered, for which the normal stress $_z$ and the shear stresses $_{xz}$ and $_{yz}$ are assumed to be zero; the initial de ection angle at the base of the cantilevers is neglected.

Table 4.1: Material parameters of cantilevers [1].

Property	Symbol	Unit	Material		
			SiO_2	MET[a]	PolySi
Young s modulus	E	Pa	$5\ 40 \times 10^{10}$	$1\ 54 \times 10^{11}$	$1\ 60 \times 10^{11}$
Poisson s ratio			$1\ 70 \times 10^{-1}$	$3\ 00 \times 10^{-1}$	$2\ 20 \times 10^{-1}$
Mass density		$kg \cdot m^{-3}$	$2\ 20 \times 10^{3}$	$2\ 70 \times 10^{3}$	$2\ 33 \times 10^{3}$
Thermal expansion		K^{-1}	$5\ 00 \times 10^{-7}$	$2\ 31 \times 10^{-5}$	$2\ 33 \times 10^{-6}$
Heat capacity	C_p	$J(kg \cdot K)^{-1}$	$7\ 70 \times 10^{-1}$	$9\ 25 \times 10^{2}$	$7\ 54 \times 10^{2}$

[a] **MET:**Metallization involves Al-Ti-W.

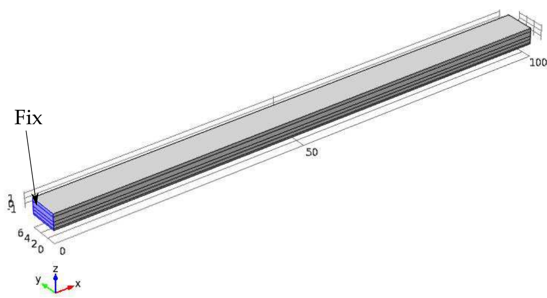

(a) 3D view of the model

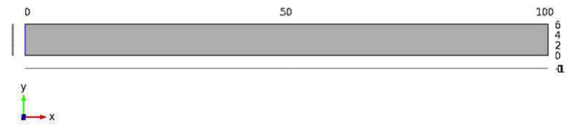

(b) XY view of the model

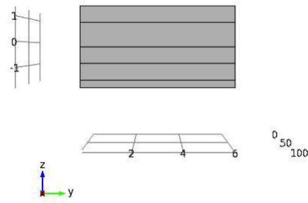

(c) YZ view of the model

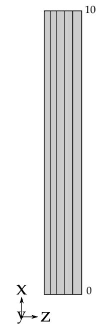

(d) ZX view of the model

Figure 4.1: 3D model of the simulated microcantilever.

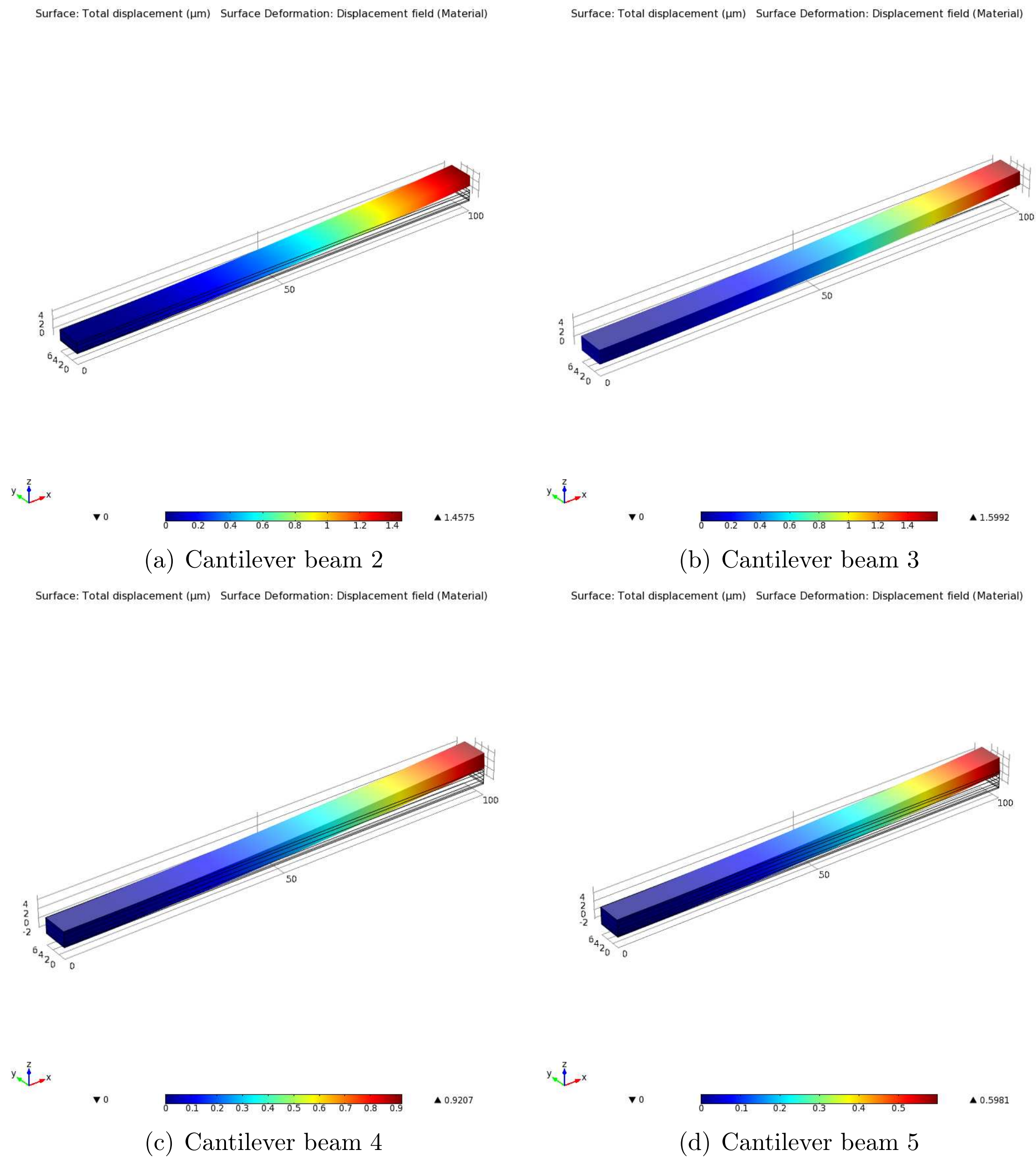

(a) Cantilever beam 2

(b) Cantilever beam 3

(c) Cantilever beam 4

(d) Cantilever beam 5

Figure 4.2: Results of deflection due to residual stress by simulation with linear elastic material condition and tetrahedral mesh.

For comparison purposes, the coe cients describing the experimental de ection pro les of these elements (see Equation (3.29)), as well as the root mean square error (RMSE) and linear gradient stress ($_{1\,max}$) of each t, are summarized in Table 4.2.

Table 4.2: Coefficients of deflection profiles by measurement [1].

Element	a_2 (1 m)	a_1 (rad)	a_0 (m)	RMSE (m)	$_{1\,max}$(MPa)
1	$7\ 39 \times 10^{-4}$	$3\ 37 \times 10^{-2}$	$2\ 75 \times 10^{-16}$	0.139	104.05
2	$2\ 13 \times 10^{-4}$	$5\ 47 \times 10^{-3}$	$-4\ 30 \times 10^{-16}$	0.033	47.92
3	$2\ 25 \times 10^{-4}$	$4\ 77 \times 10^{-3}$	$1\ 49 \times 10^{-16}$	0.022	70.22
4	$1\ 46 \times 10^{-4}$	$4\ 59 \times 10^{-3}$	$-7\ 20 \times 10^{-17}$	0.022	44.32
5	$8\ 80 \times 10^{-5}$	$3\ 68 \times 10^{-3}$	$-8\ 80 \times 10^{-17}$	0.016	35.68
6	$1\ 69 \times 10^{-4}$	$4\ 95 \times 10^{-3}$	$0\ 00 \times 10^{-0}$	0.018	60.39
7	$1\ 45 \times 10^{-4}$	$5\ 04 \times 10^{-3}$	$-8\ 00 \times 10^{-18}$	0.014	68.12
8	$6\ 58 \times 10^{-5}$	$3\ 75 \times 10^{-3}$	$5\ 00 \times 10^{-17}$	0.037	44.96
9	$6\ 56 \times 10^{-5}$	$3\ 39 \times 10^{-3}$	$-6\ 25 \times 10^{-16}$	0.031	60.95
10	$7\ 90 \times 10^{-5}$	$1\ 80 \times 10^{-3}$	$-1\ 53 \times 10^{-16}$	0.053	67.50
11	$4\ 85 \times 10^{-5}$	$3\ 13 \times 10^{-3}$	$4\ 26 \times 10^{-16}$	0.030	50.94
12	$6\ 46 \times 10^{-5}$	$3\ 61 \times 10^{-3}$	$8\ 95 \times 10^{-16}$	0.035	51.55
13	$6\ 36 \times 10^{-5}$	$1\ 44 \times 10^{-3}$	$2\ 47 \times 10^{-15}$	0.042	64.64
14	$6\ 64 \times 10^{-5}$	$2\ 12 \times 10^{-3}$	$9\ 70 \times 10^{-16}$	0.034	62.95
15	$4\ 19 \times 10^{-5}$	$2\ 84 \times 10^{-3}$	$1\ 47 \times 10^{-15}$	0.033	47.30

4.2 Characterizing Residual Stress

Now, in application of our methodology, the linear stress gradient for each structure can be calculated from Equation (3.33), as shown in Table 4.3. Likewise, by means of a parametric FEM analysis, a second estimation for the linear stress gradient can be found by comparing the experimental and simulated maximum displacements. For the sake of simplicity, only fourteen microcantilevers are considered in the present simulation study.

Table 4.3: Comparison of linear gradient stress from parametric analysis and our proposed method.

Beam	$_{1\,max}$ (MPa) from parametric analysis	$_{1\,max}$ (MPa) from Eq. (3.33)	% Abs. Error
2	108.64	45.129	48
3	127.57	81.406	33
4	97.76	53.536	43
5	75.46	46.177	38
6	126.88	83.189	33
7	138.22	92.037	33
8	90.41	87.594	3
9	137.98	91.002	33
10	109.06	89.849	17
11	104.88	79.312	22
12	104.05	94.59	9
13	106.62	78.719	26
14	109.59	89.375	18
15	107.46	76.689	28

To compute the absolute error between both linear gradient stress values, for each cantilever beam, it was used the expression:

$$\%\ absolute\ error = ABS\left(\frac{expected\ value - new\ value}{expected\,value}\right) \cdot 100 \tag{4.1}$$

where for this speci c case, the *expected value* is the gradient stress value provided by the parametric analysis, and the *new value* is depicted by the gradient stress from Equation (3.33). For example, for the beam 2, the % absolute error is:

$$\%\ absolute\ error = ABS\left(\frac{108\ 64MPa - 45\ 129MPa}{108\ 64MPa}\right) \cdot 100 \approx 58\% \tag{4.2}$$

As shown in Table 4.3, there is a prevalence in the error, approximately 27% in average.

Table 4.4 shows the maximum displacements measured for the beams as reported in [1], together with FEM-obtained values considering linear gradient stress value from [1], and Equation 3.33.

Table 4.4: Comparison of maximum deflections

Beam	Max. Disp. B [b] (m)	Max. Disp. C [c] (m)	Max. Disp. D [d] (m)
2	2.677	1.457	1.384
3	2.727	1.599	1.829
4	1.919	0.920	1.099
5	1.248	0.598	0.770
6	2.185	1.086	1.472
7	1.954	0.980	1.314
8	1.033	0.526	1.006
9	0.995	0.446	0.663
10	0.970	0.610	0.802
11	0.780	0.479	0.609
12	1.007	0.509	0.918
13	0.780	0.479	0.581
14	0.876	0.511	0.717
15	0.703	0.313	0.503

The stress-induced de ection pro les associated to Table 4.4 are shown in Figure 4.3 and Figure 4.4, whose RMS errors are reported in Table 4.5.

[b] **Fitted data from [1]**
[c] **Simulation from COMSOL, using gradient stress value from [1]**
[d] **Simulation from COMSOL, using gradient stress resulting from our proposed method**

Table 4.5: Root mean square error in deflection profiles

Beam	RMSE E [e] (m)	RMSE F [f] (m)	RMSE G [g] (m)
2	0.575	0.611	0.036
3	0.535	0.425	0.111
4	0.494	0.411	0.084
5	0.332	0.254	0.079
6	0.539	0.359	0.181
7	0.489	0.337	0.154
8	0.287	0.066	0.227
9	0.283	0.185	0.100
10	0.177	0.087	0.092
11	0.217	0.121	0.099
12	0.266	0.089	0.191
13	0.149	0.103	0.047
14	0.182	0.087	0.099
15	0.119	0.503	0.091
Average	0.332	0.260	0.114

[e] **Between Fitted data from [1] and FEM using $\sigma_{1,max}$ from [1]**
[f] **Between Fitted data from [1] and FEM using $\sigma_{1,max}$ from Eq 3.33**
[g] **Between FEM using $\sigma_{1,max}$ from [1] and FEM using $\sigma_{1,max}$ from Eq 3.33**

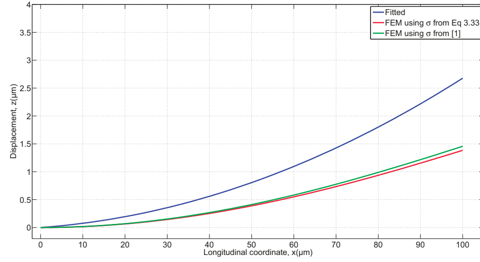

(a) Cantilever 2

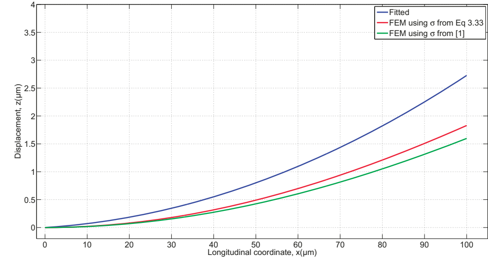

(b) Cantilever 3

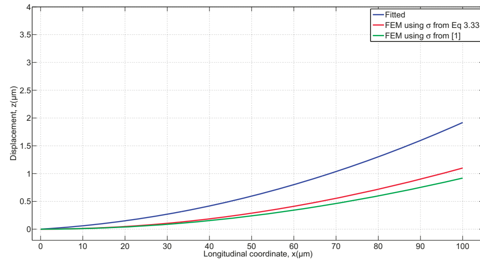

(c) Cantilever 4

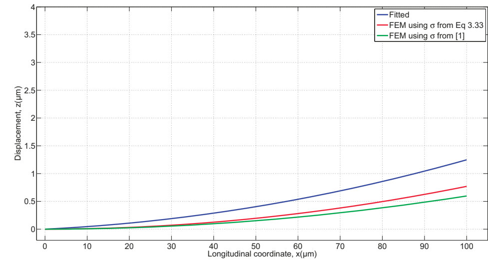

(d) Cantilever 5

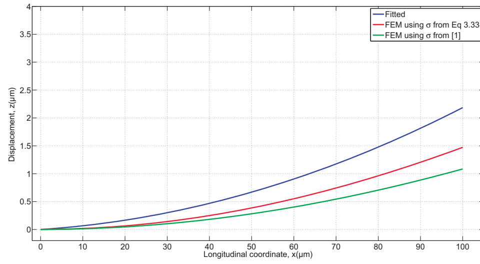

(e) Cantilever 6

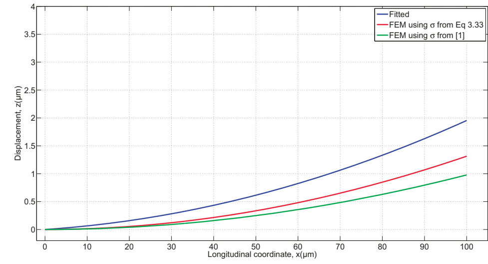

(f) Cantilever 7

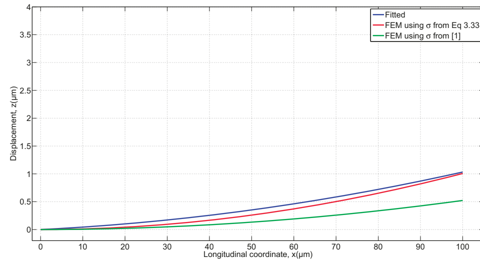

(g) Cantilever 8

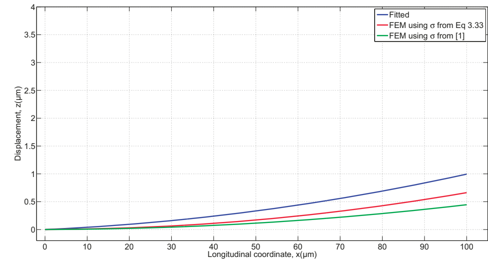

(h) Cantilever 9

Figure 4.3: Comparing deflection profiles

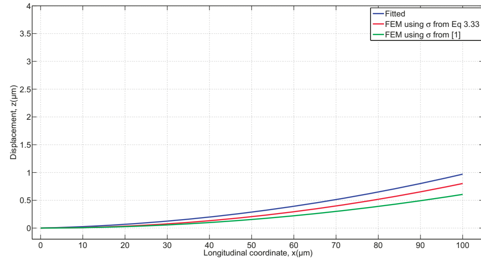

(a) Cantilever 10

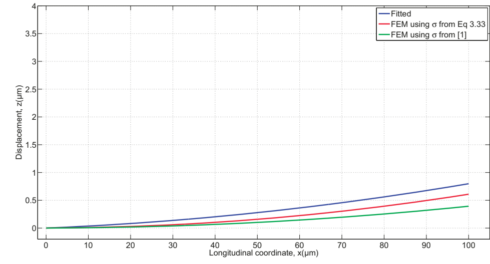

(b) Cantilever 11

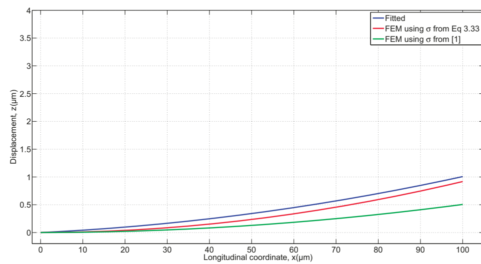

(c) Cantilever 12

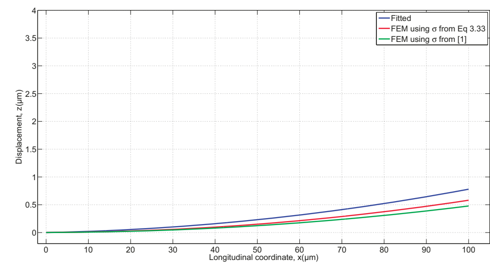

(d) Cantilever 13

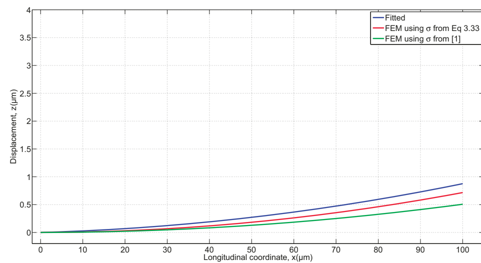

(e) Cantilever 14

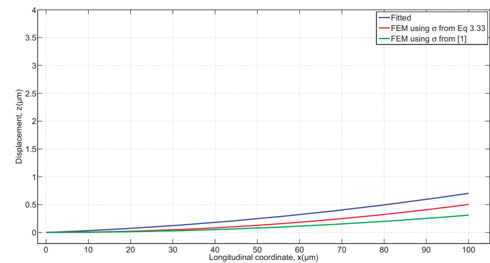

(f) Cantilever 15

Figure 4.4: Comparing deflection profiles

4.3 Discussion

From Table 4.4, it can be calculated an absolute error average concerning the maximum displacement for each microcantilever beam, using Equation (4.1).

First obtaining the absolute error average in the maximum displacements between tted data in [1] and the maximum displacements obtained by FEM using $_{1\,max}$ from [1]. Resulting a value of 47% in average.

Second, computing the absolute error average in the maximum displacements between tted data in [1] and the maximum displacements by FEM considering $_{1\,max}$ from Equation (3.33). The absolute error average is 27% in average.

Third, calculating the absolute error average in the maximum displacements between FEM using $_{1\,max}$ from [1] and a FEM considering $_{1\,max}$ considering the $_{1\,max}$ from Equation (3.33). Resulting 38% of error in average.

The minimum absolute error in average is shows by using the linear gradient stress resulting from Equation (3.33), this is expected taking into account that the model proposed considers a new linear gradient stress from a parametric analysis in this value. Therefore, the maximum displacements are better reproduced by using this technique.

In the context of the RMS error, a comparison between absolute average is performed just to evaluate the behavior along the curvature pro le by using those three di erent ways to reproduce de ection. Table 4.5 shows the RMS errors presented by the di erent ways to reproduce the de ections du to the residual stress. Concerning the RMSE E, there is a prevalence of 0.332 m in average, whereas in RMSE F the average of error is of 0 260 m, and the average of RMSE G is of 0 114 m.

Concluding that the best performances, based on errors already computed, are obtained by using Equation (3.33) in order to generate the de ections du to residual stress there computed.

Chapter 5

Modeling Piezoresistive Transducer

This chapter presents the model and simulation of the piezoresisitve element used as transducer from mechanical de ection to electrical resistance. Moreover, a comparison among three di erent geometries is shown for the piezoresistive element, to conclude with illustrations of the important parameters to consider.

The piezoresistive element is simulated using nite element analysis, provided by COMSOL Multiphysics ©. The model considers a growth base plane in the piezoresistive elements as <110>. The reason why this condition is considered is because in most of Integrated Circuits (IC), the orientation of the silicon wafer is of type <110> as well.

5.1 Modeling a First Geometry

As presented in chapter 3, the piezoresistivity is the energy conversion phenomena that translates a mechanical change, from de ection of the microcantilever beam, to an electrical signal. Using a Wheatstone bridge. The piezoresistive element provided in the microcantilever may have a de ned geometry which performs according to di erent loading conditions. The Figure 5.1 depicts the Wheatstone bridge used to produce an electrical signal in terms of changes in piezoresistance.

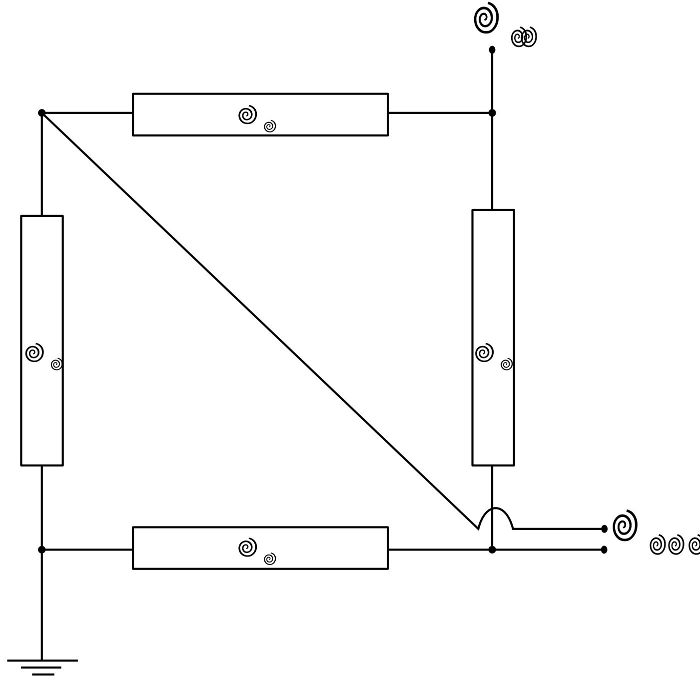

Figure 5.1: Whetstone bridge used in microcantilever

In Figure 5.1, where R_1, R_2, R_3, are equal, while R_s represents the sensing element that changes as a function of the de ection of the microcantilever. The voltage across the bridge (V_{out}) can be found by simple voltage division as follows:

$$V_{out} = \quad \frac{R_3}{R_S + R_3} \quad \frac{R_1}{R_1 + R_2} \quad V_{in} \tag{5.1}$$

The voltage supply, V_{in}, is a known value, and the value of the four resistors is found by nite element analysis.

Figure 5.2 shows the microcantilever beam with the detailed view of the Wheatstone bridge shown over the edge.

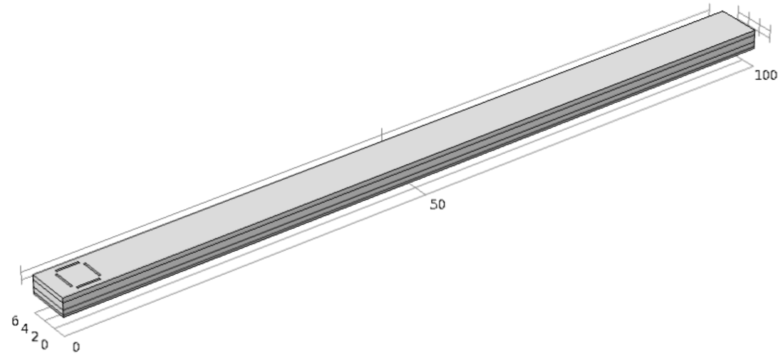

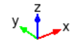

(a) Microcantilever beam 2, provided with a Wheatstone bridge

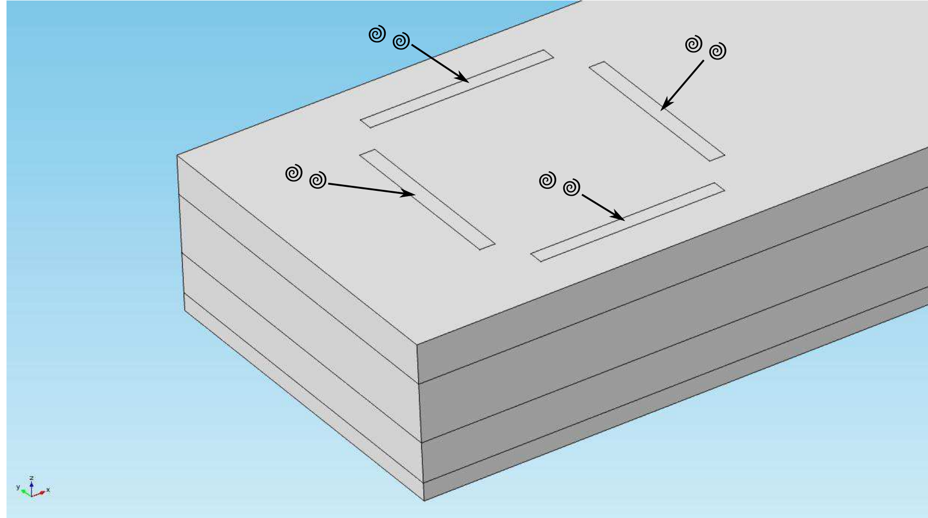

(b) Detailed view of the Wheatstone bridge

Figure 5.2: Microcantilever beam number 2, using a Wheatstone bridge

Figure 5.2, shows the first of the three geometries where R_1, R_2, R_3, and R_s appear in rectangular fashion. Using Comsol Multiphysics ©, a simulation of this phenomena is performed, considering the orientation of growth base plane of the piezoresistive elements, made of poly-Si material.

In simulations performed, were considered, for the same microcantilever beam, three di erent resistive bridge con guration changing the geometry of the sensing element and the same stress condition expressed by Equation (3.23). The value of the linear gradient stress in this stress tensor is the one obtained by using our proposed method, Equation (3.33). The resistor dimensions for R_1, R_2, R_3, and R_s are: width of 0 25 m, length of 3 m, and thickness of 0 25 m. The initial resistance is 8 540 with no stress applied.

Table 5.1 illustrates the four constants de ned in the model.

Table 5.1: Table of constants, piezoresistivity coe cients

Name	Value	Description
$rhoe0const$	$180e^{\ 6}[\ \ m]$	Resistivity of the unstressed material
$pi11const$	$6\ 6e^{\ 11}[1\ \ Pa]$	Piezoresisitve stress coe cient, 11 component
$pi12const$	$1\ 1e^{\ 11}[1\ \ Pa]$	Piezoresisitve stress coe cient, 12 component
$pi44const$	$138\ 1e^{\ 11}[1\ \ Pa]$	Piezoresisitve stress coe cient, 44 component

The model used in the simulator also de nes several scalar expressions, described by Table 5.2.

Table 5.2: Table of scalar expressions used in the simulation model

Name	Symbol	Expression	Description
$RHOE0$	$_{e}\ 0$	$rhoe0const$	Resistivity of the unstressed material
$piijscalar\,(i\ \ j =$ $11\ \ 12\ \ 44)$	$_{ij}$	$piijconst$	Piezoresistive stress coe cient, ij component
$T_{ij}\,(i\ \ j = 1\ \ 2\ \ 3)$	T	$coord1T_{ij}$	Transformation matrix, ij component
$sij1scalar\,(i\ \ j =$ $x\ \ y\ \ z)$	$_{l}$	$sijlsmsld$	Material stress in local coordinates
$rhoerlij\,(i\ \ j =$ $1\ \ 2\ \ 3)$	$_{e\,l}\quad _{e\,0}$	$\begin{matrix}1 & 0 & 0\\ 0 & 1 & 0\\ 0 & 0 & 1\end{matrix} + \quad _{l}$	Relative resistivity ($rhoe\ \ rhoe0$) in local coordinates, ij component
$rhoerij\,(i\ \ j =$ $1\ \ 2\ \ 3)$	$_{e}\quad _{e\,0}$	$T\ \ \frac{_{e\,l}}{_{e\,0}}\ \ T^T$	Relative resistivity ($rhoe\ \ rhoe0$) in global coordinates
$detrhoer$	$det(\ _{e}\quad _{e\,0})$	$det(\ _{e}\quad _{e\,0})$	Determinant of the relative resistivity
$sigmaeij(i\ \ j =$ $1\ \ 2\ \ 3)$	$_{e}$	$1\quad _{e}$	Conductivity in global coordinates
$PIij(i\ \ j = 1\ \ 2\ \ 3)$		$_{ij}$ ordered for Poly-Si like material	Piezoresistive stress coe cient matrix component

Where:

$RHOE0$, $piijscalar$: They simply repeat the constant.

T_{ij}: Matrix that map the coordinate system variables to be used in the rest of the expressions.

$sij1scalar$: De ne the mapping to the stress values solved by the structural application mode.

The rest of the variables de ne the coupling between stress and the resistance change, transformation of local resistance to global, inversion of resistance to conductivity, and the mapping of material constant to the full piezoresistive stress coe cient matrix.

The model contains one prede ned coordinate system, this coordinate system is aligned with the $< 110 >$ orientation. Appendix A.2 presents the theoretical background of coordinate systems transformation.

Using the model of piezoresistivity described before, the microcantilever beam number 2, the Wheatstone bridge mentioned, and considering a residual stress gradient value of: 45 129MPa, a stress force sweep was performed, from 0MPa to 45 129MPa considering 6 steps. The de ection in the microcantilever due to residual stress generates a change in the electrical resistance having an applied voltage of 2Volts.

The Figure 5.3 depicts the maximum de ection achieved by the microcantilever beam number 2, using a Wheatstone bridge near of its xed side.

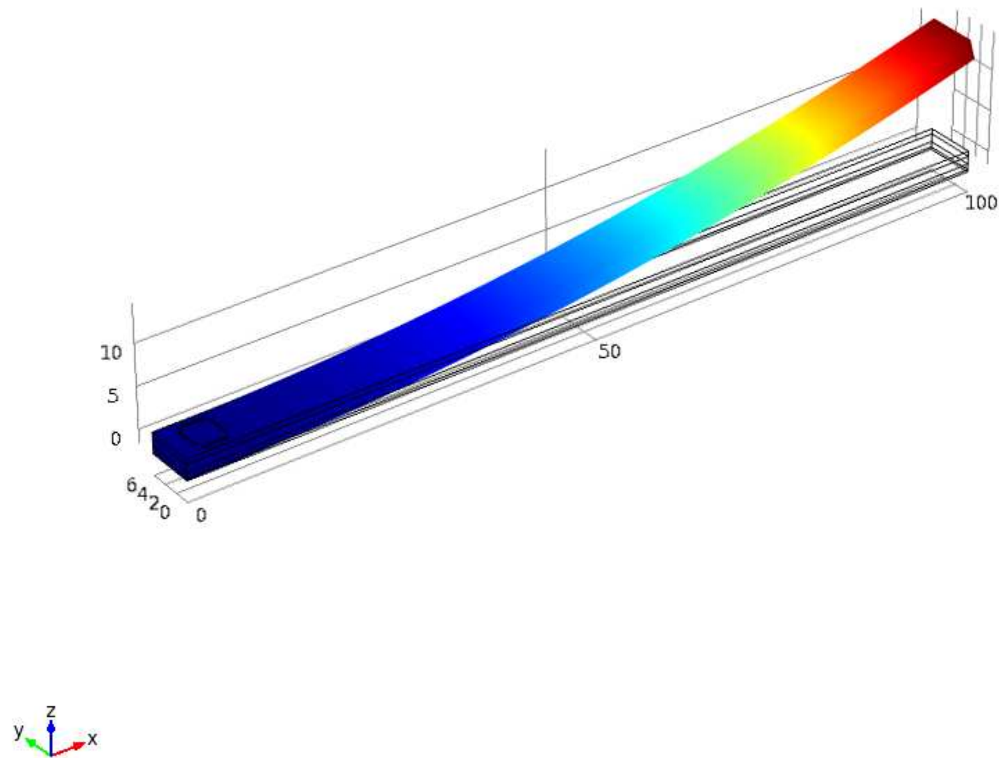

Figure 5.3: De ection due to residual stress in beam 2, using a Wheatstone bridge located over the xed end.

Using an extended view of the con guration of Wheatstone bridge designed for the

microcantilever beam, Figure 5.4 shows the contribution of the stress to piezoresistive elements. Also, the Von Mises stress, that is an equivalent or e ective stress at which yielding is predicted to occur in ductile materials [70], is represented.

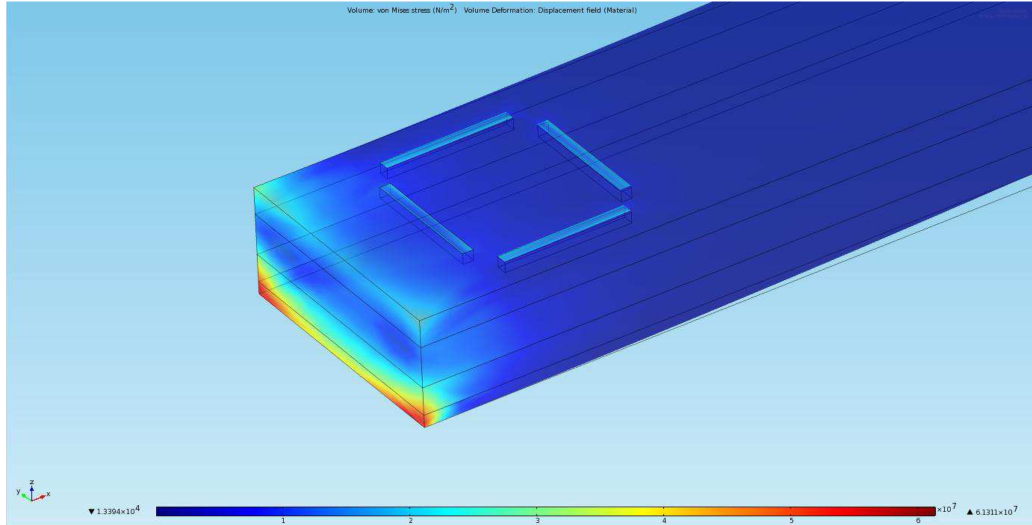

Figure 5.4: Detailed view of resistive bridge over the xed end for the beam 2, showing the contribution of the Von Mises stress due to initial de ection.

In Figure 5.4 is presented the Von Mises Stress in $(N\ m^2)$ experienced by the microcantilever during de ection. It is observed the contribution of this stress to resistive elements in the read-out-circuit. As is shown, the maximum contribution of stress is nearest to resistive elements. According with this fact, the maximum deformation that experiences the resistive element, causes a change in their piezoresistivity, and thereby unbalancing the bridge.

Figure 5.5 represents the output voltage of the Wheatstone bridge versus the maximum displacement of the microcantilever, due to residual stress and during the 6 steps of the parametric sweep analysis in the residual stress gradient.

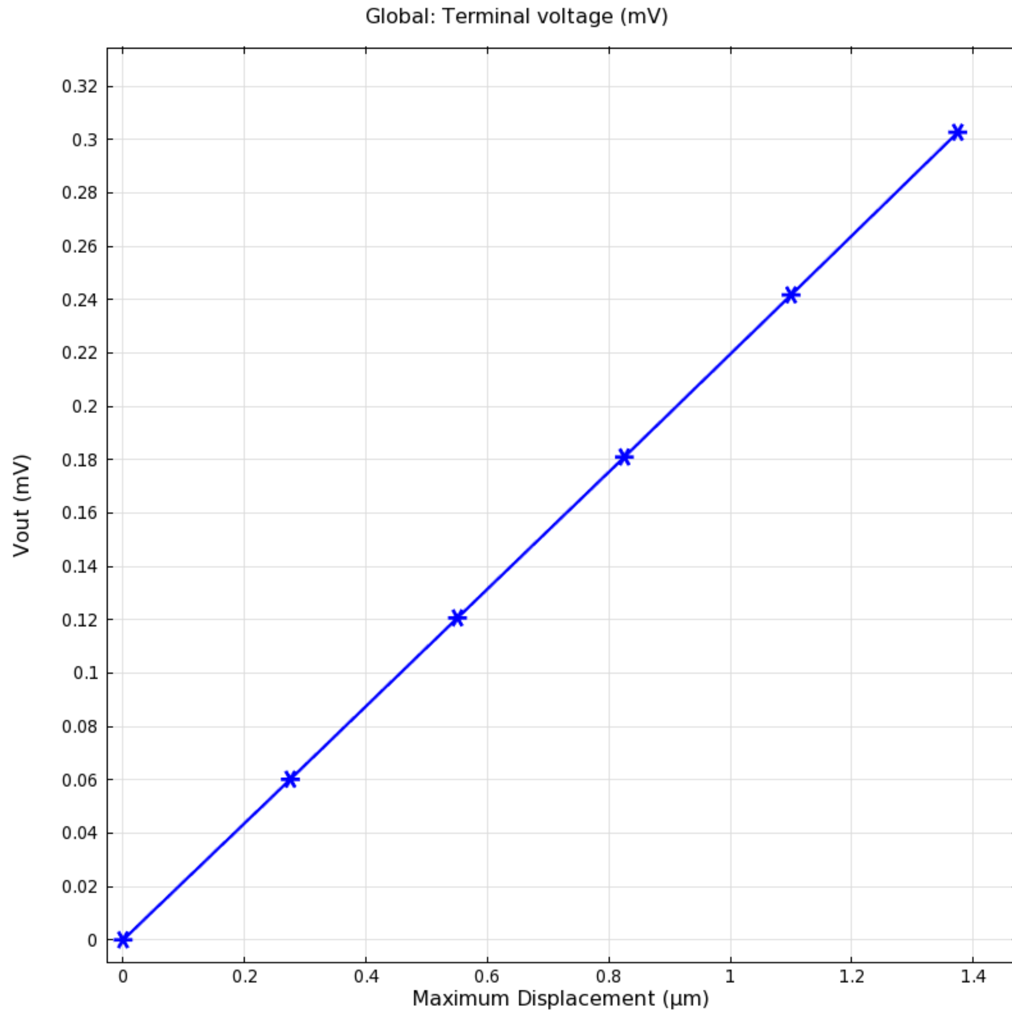

Figure 5.5: Output voltage versus maximum displacement in microcantilever 2

It is evident a linearity in the response of the Wheatstone bridge, starting from 0 according to the balanced state of the bridge. This is because the four resistive elements have the same dimensions, hence they have the same electrical resistance. But once the residual stress appears, a curling in the cantilever is resulting and resulting in surface stress that will a ect the sensing element; R_S. As long as the gradient stress value is increasing, a raise in the out-of-plane de ection is being detected by the resistive element, the value of the output voltage also is increasing in a proportional way. Finally, the parametric sweep analysis, demonstrates the perfect linearity in outcomes of the Wheatstone bridge.

The following table summarizes the results of this rst simulation, using the microcantilver 2.

Table 5.3: Results of parametric sweep analysis, for beam 2

Step	$_{1\,max}$ in (MPa)	Max. Disp. in (m)	V_{out} in (mV)	Von Mises stress in ($MN\ m^2$)	Resistance R_s in ( )
1	0	0	0	0	8640
2	9.025	0.275	0.0602	13.59	8639.2573
3	18.05	0.550	0.1207	27.19	8638.5109
4	27.075	0.825	0.1810	40.78	8637.7552
5	36.100	1.100	0.2417	54.38	8636.9983
6	45.125	1.374	0.3027	67.97	8636.238

5.1.1 Discussion

After analyzing data from Table 5.3, it is stated again a linearity in output voltage of the read-out-circuit designed. Reaching a maximum value of output voltage about 0.3 mV DC. As expected, the increasing in de ection experienced by microcantilever, is directly proportional to the stress in the beam. Von Mises stress up to 67.97 MPa is achieved, this maximum stress is concentrated nearest to Wheatstone bridge in the xed end of the microcantilever. Another important observation from results is the change in resistance that experiences the sensing element; R_S. Its initial value, without stress present is of 8640 , while it decrease to 8636.238 as the maximum gradient stress is reached. In other words, this means that the resistance is compressing. By nite element analysis were obtained those measures.

The parameters of the element of mesh are:

Maximum element size: 5.5 m,

Minimum element size: 0.4 m,

Complete mesh consist of 5881 elements.

5.2 Modeling a Second Geometry

In this section, a second geometry for the resistive element is considered. Now a U-shaped resistive element is used as the R_s of the Wheatstone bridge in the same microcantilever beam; number 2. The schematic diagram of this new resistive element is shown by the following Figure 5.6

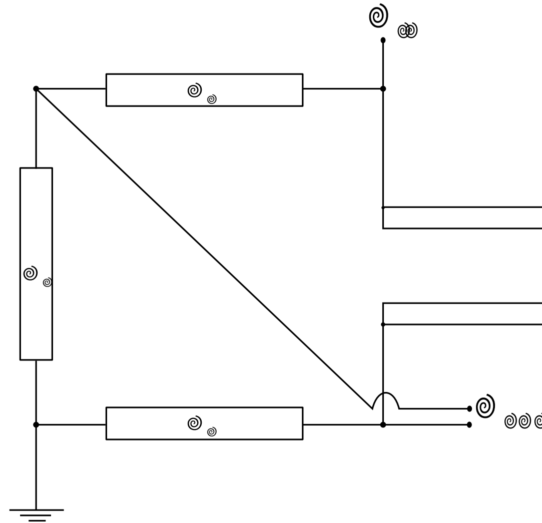

Figure 5.6: Schematic diagram of a Wheatstone bridge using U-shaped resistive element

Figure 5.6 shows the Wheatstone bridge used for this model of piezoresistivity, with R_1, R_2, and R_3 having in the same shape as in the rst model. Dimensions of R_S are shown by Figure 5.7.

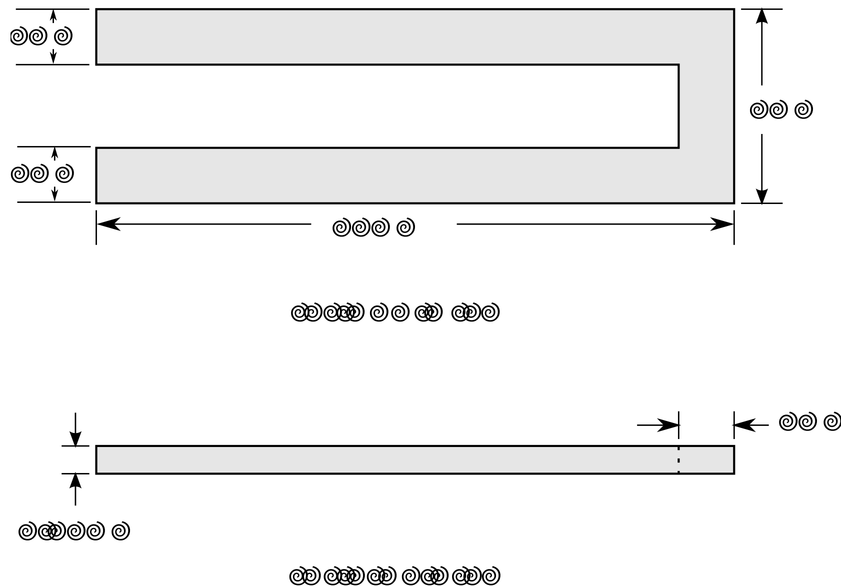

Figure 5.7: U-shaped resistive element

Using now, the U-shaped form for the resistive element, is simulated for piezoresistivity using COMSOL Multiphysics ©. The results of parametric sweep analysis are summarized in Table 5.4. The simulation uses the same voltage input value of 2Volts, and the same environmental conditions are used in the microcantilever beam. This geometry

has two legs of 50 m of length, separated by a gap of 1 m. Each leg, has 1 m of width and all the U-shape form has a thickness of 0.25 m. Considering those dimensions, its electrical resistance without stress is $R_{S0} = 72\ \ 054\ 7214$

The new model of Wheatstone bridge using the U-shaped resistive element in the microcantilever beam is depicted in Figure 5.8.

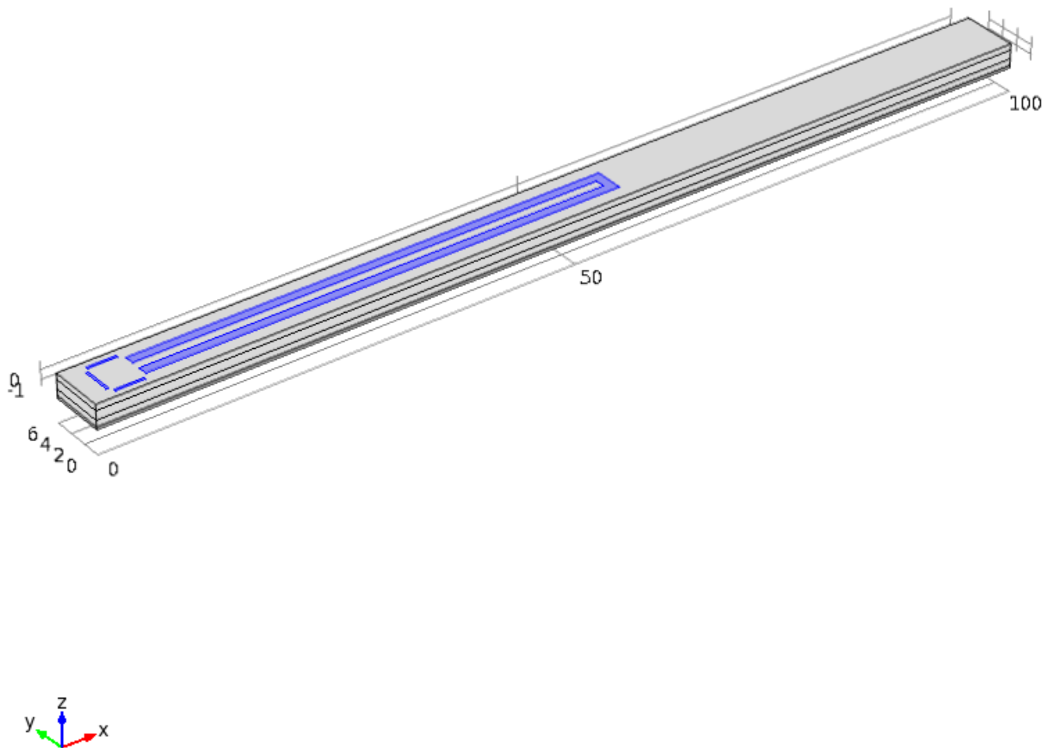

Figure 5.8: 3D model for the Wheatstone bridge using U-shaped resistive element

Figure 5.8 shows the U-shaped resistance used in this simulation, as long as the microcantilever beam is de ecting due to residual stress. The sensing resistance follows the microcantilever s curvature stress. By applying 2V electrical potential, the output measured voltage is plotted in Figure 5.9.

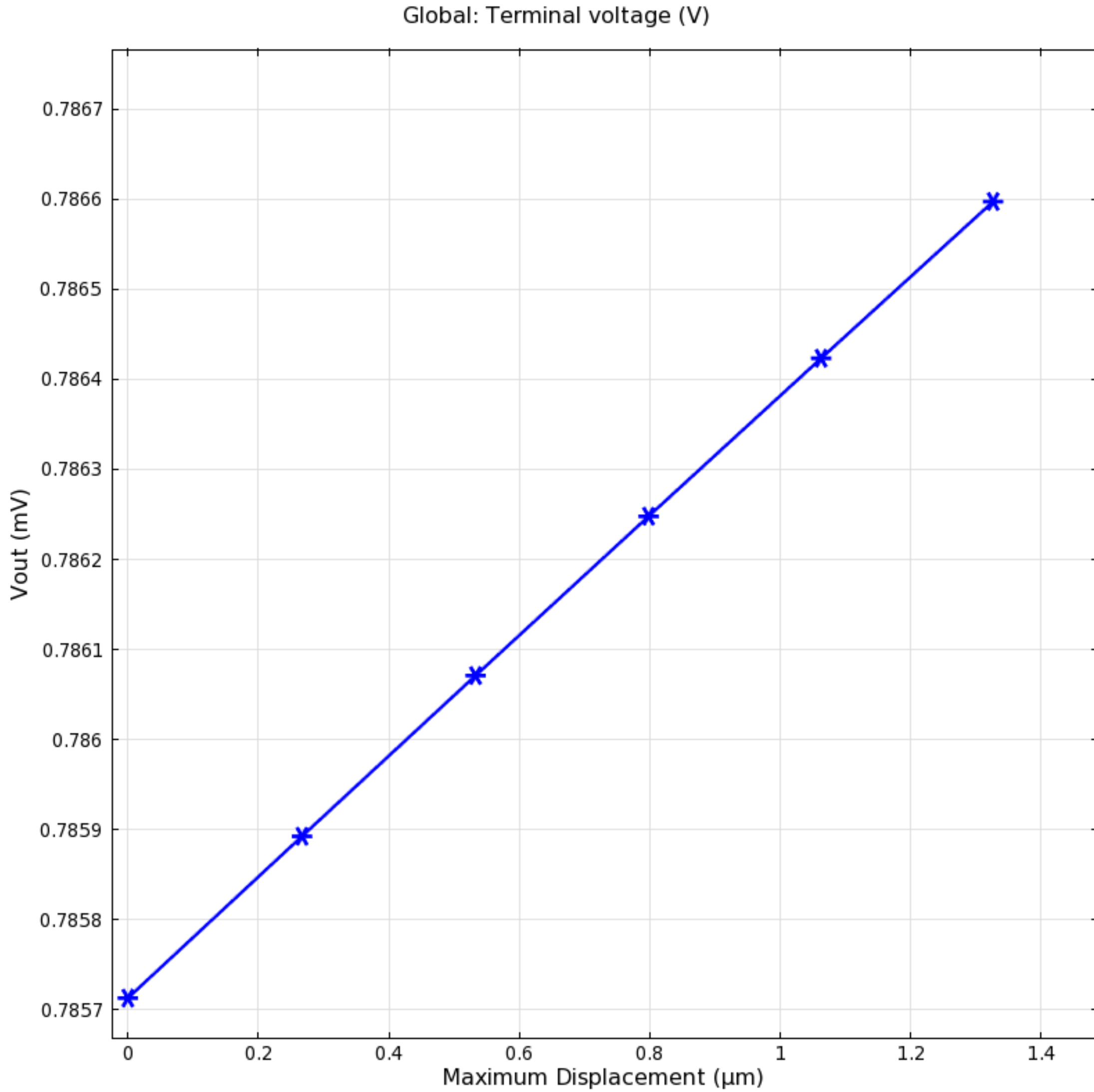

Figure 5.9: Output voltage versus maximum displacement in microcantilever 2, using U-shaped resistance

The output voltage is governed by a linearity depending directly of the maximum displacement of the microcantilever beam. However, the initial value, without stress is not zero. The Wheatstone bridge is not balanced. The minimum voltage in the read-out-circuit, using 2V as input voltage, considering this second geometry is $V_{out} = 785\ 7134mV$, while the maximum value of output voltage is $V_{out} = 786\ 5974mV$.

Figure 5.10 illustrates the microcantilever beam at its maximum displacement. Note that for the sake of simplicity, an ampli cation factor of 10 was applied to picture, but not in the simulation. Figure 5.10 also depicts the contribution of Von Mises stress involved in the structure. It is evident the large concentration of stress nearest the border of the U-shaped resistive element.

Volume: von Mises stress (N/m^2)   Volume Deformation: Displacement field (Material)

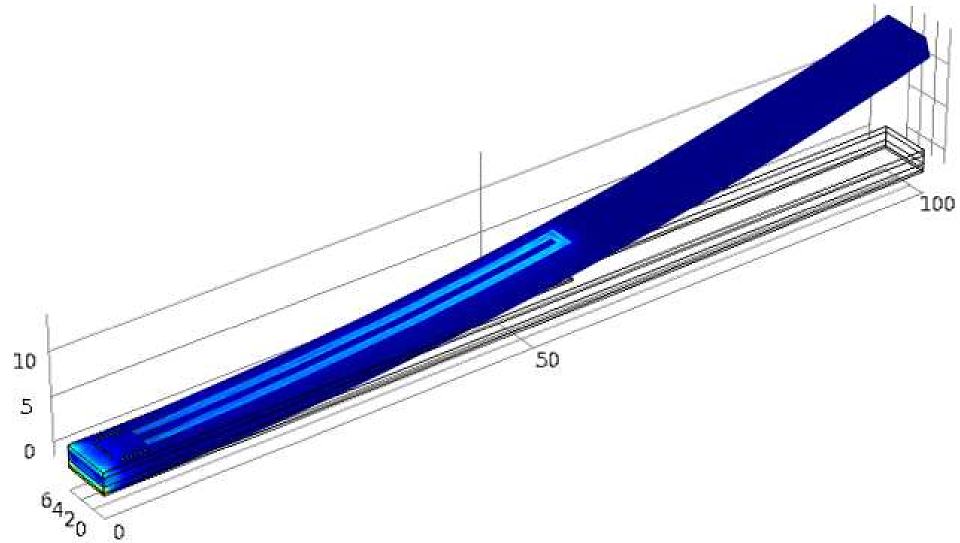

Figure 5.10: Von Mises stress in maximum de ection, using U-shaped resistance for beam 2

After running a parametric sweep analysis in the residual gradient stress, simulated results are summarized in Table 5.4.

Table 5.4: Results of parametric sweep analysis using U-shaped form, for Beam 2

Step	$_{1\,max}$ in (MPa)	Max. Disp. in (m)	V_{out} in (mV)	Von Mises stress in ($MN\ \ m^2$)	Resistance R_s in (K)
1	0	0	785.7134	0	72.055
2	9.025	0.2669	785.8930	13.598	72.047
3	18.05	0.5329	786.0713	27.197	72.039
4	27.075	0.7982	786.2482	40.796	72.030
5	36.100	1.0626	786.4235	54.395	72.021
6	45.125	1.3263	786.5974	67.994	72.012

5.2.1 Discussion

Comparing both results, from rst and second geometries, a better performance is noted using a balanced Wheatstone bridge, considering an equivalent geometry in four resistive elements. Taking into account, that the minimum value of the output voltage is zero, when no stress is applied.

Furthermore, the sensitivity of the rst geometry is better than the second geometry. This is, using U-shaped resistive element, the sensitivity reached is of $0.66mV\ \ m$, while using the rst geometry is achieved a sensitivity of $0.2203mV\ \ m$. Also, the change in resistance from results of nite element analysis is lower in the rst geometry. according to Table 5.4.

The parameters of the element of mesh are:

Maximum element size: 5.5 m,

Minimum element size: 0.4 m,

Complete mesh consist of 8151 elements.

5.3 Modeling a Third Geometry

A third geometry in the resistive element is considered to perform a nite element analysis. Now, a serpentine-shaped element is considered as the sensing resistance. Figure 5.11 depicts a schematic diagram of the Wheatstone bridge used. As shown, the other three resistances of the resistive bridge did not change.

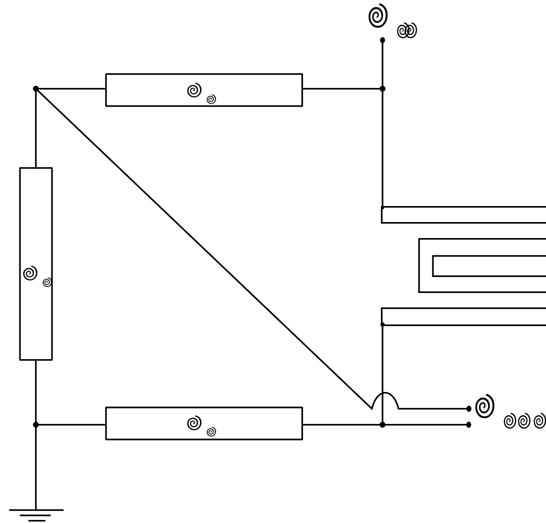

Figure 5.11: Schematic diagram of a Wheatstone bridge using serpentine-shaped resistive element

The serpentine dimensions are illustrated in the Figure 5.12.

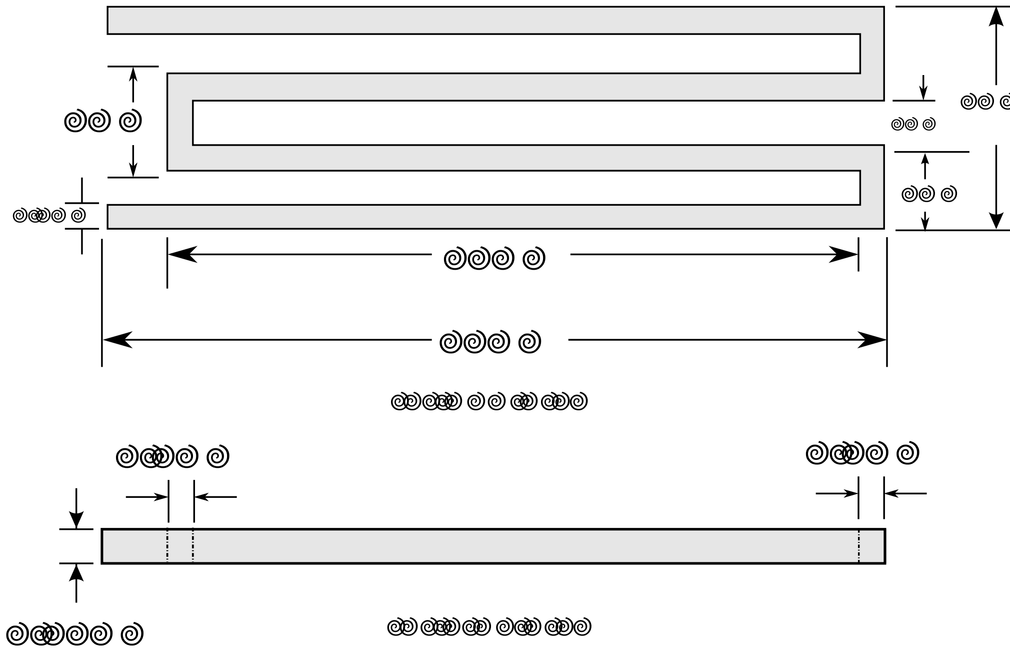

Figure 5.12: Serpentine shaped sensing resistance used in third geometry

The serpentine has four legs of 0.5 m of width. The whole structure has a thickness of 0.25 m and its initial electrical resistance, without stress, is of $R_{S0} = 278\,673K$. This value is obtained as the previous cases, using nite element analysis. Also, as the others two cases of geometry studied here, the mesh using for the computation of change in resistance was the free tetrahedral type, with a ne size prede ned by the tool. The

mesh consists of 22696 elements. To illustrate the new resistive bridge, is presented the Figure 5.13.

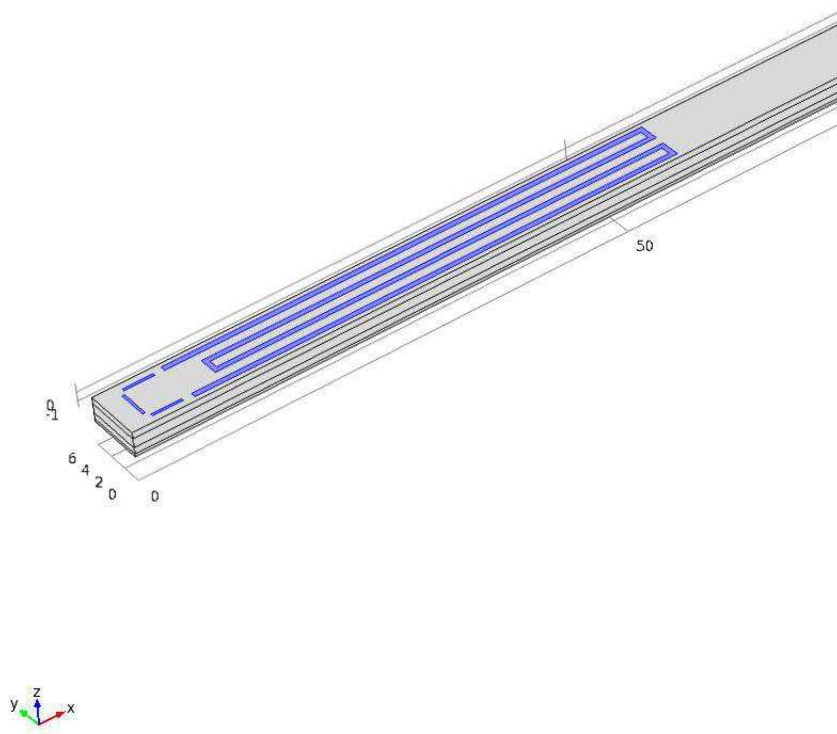

Figure 5.13: Resistive bridge with serpentine shaped element

As before, the input voltage in the bridge is 2 V DC, the number of steps in parametric sweep analysis was 6, starting from 0 MPa to the value proposed by our method for the microcantilever beam 2, $_{1\,max} = 45\,125MPa$. The results of the simulation doing a parametric sweep analysis, incrementing the residual gradient stress, is shown in Table 5.5.

Table 5.5: Results of parametric sweep analysis using serpentine shaped form.

Step	$_{1\,max}$ in (MPa)	Max. Disp. in $(\ m)$	V_{out} in (mV)	Von Mises stress in $(MN\ m^2)$	Resistance R_s in $(K\ \ )$
1	0	0	939.8216	0	278.506
2	9.025	0.2671	940.1048	13.629	278.479
3	18.05	0.5332	940.3877	27.257	278.450
4	27.075	0.7985	940.6701	40.886	278.419
5	36.100	1.063	940.9524	54.515	278.386
6	45.125	1.3268	941.2342	68.144	278.351

Table 5.5 illustrates that increments in the residual gradient stress causes a linear change in the de ection of the microcantilever, and thereby a proportional growth in surface stress.

Figure 5.14 shows that the maximum stress is located nearest to serpentine shaped resistance.

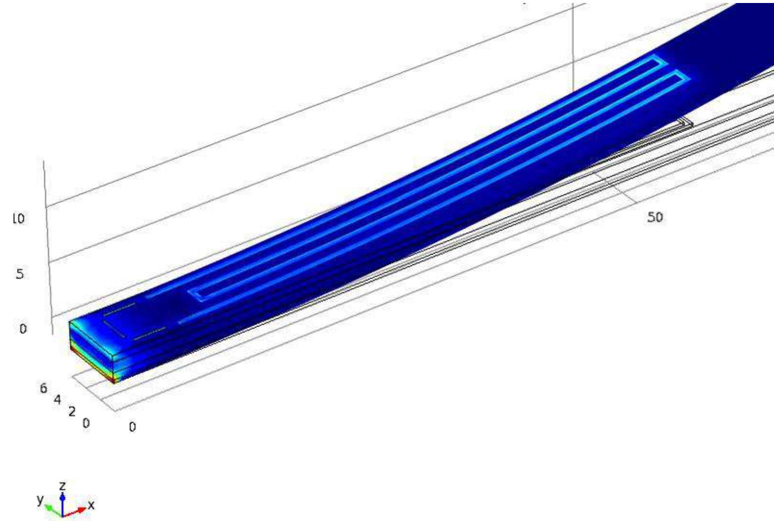

Figure 5.14: Von Mises stress at maximum de ection, using serpentine shaped resistance for beam 2

As Figure 5.14 shows, the higher contribution of stress is nearest to the serpentine edge. This causes the largest change in resistance only for the sensing element. Also, other high stress zone are observed at the xed edge of the microcantilever. However, this zone was not used to implant the resistive elements because the intention of having the sensing element throughout the length of the microcantilever is to measure the de ection due to residual stress in the whole longitude.

The resulting output voltages of the bridge versus the maximum de ection of the microcantilever are presented in Figure 5.15.

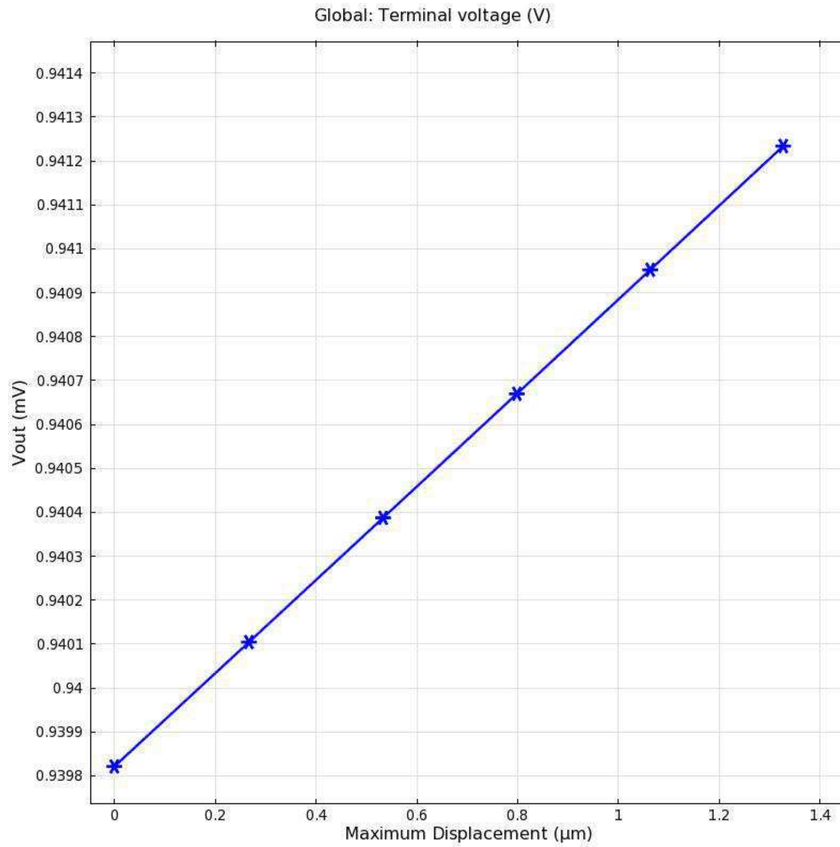

Figure 5.15: Output voltage versus maximum displacement in microcantilever 2, using serpentine-shaped resistance.

The slope of this curve is of 1 06mV m. Which is the highest sensitivity of all geometries analyzed. The following section gives a more detailed comparison of all geometries.

Figure 5.16 illustrates the level of meshing applied to perform the device simulations.

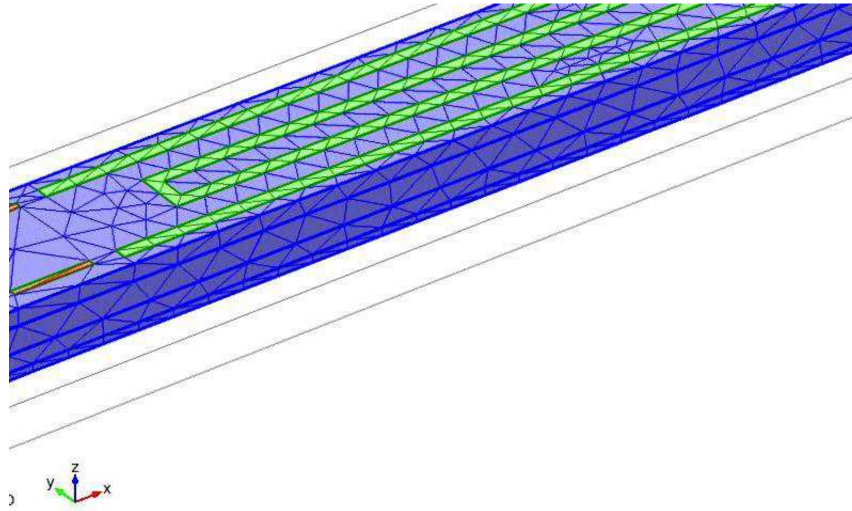

Figure 5.16: Level of meshing applied to the 3D model.

The parameters of the element of mesh are:

Maximum element size: 5.5 m,

Minimum element size: 0.4 m,

Complete mesh consist of 9720 elements.

5.3.1 Discussion

Analyzing the results from this third simulation, the performance of the serpentine shaped element in the bridge was lower sensitive than the others two cases.

Table 5.6 illustrates the performance results of the 3 di erent geometries.

Table 5.6: Performance comparison of the three geometries.

Parameter	Block shaped	U-shaped	Serpentine shaped
Max. De ection (z)	1 374 m	1 326 m	1 326 m
Resistance without stress (R_{S0})	8640	72 055K	278 673K
Change in Resistance (R)	3 762	43	155
Sensitivity$_1$ (R z)	2 73 m	32 m	116 82 m
Sensitivity$_2$ (V z)	0 22mV m	0 66mV m	1 06mV m

From table of results in the performing of the piezoresistive elements; the maximum de ection is practically the same. Also, the initial resistance of each di erent geometry

di ers in more than one order of magnitude between them. This was an expected result, because the three geometries have di erent dimensions. The geometry with the highest initial resistance is the serpentine shaped, with $278.673K$, while the block shaped element has 8,640 . The largest change in resistance was present in the serpentine shaped element with 155 ; while the smallest change in resistance was present in the block shaped with 3 76 . The U-shaped element has 43 of change of resistance, according to Table 5.6.

Moreover, the serpentine shaped element has the largest resolution step, with 116 82 m the resolution of each of the resistive bridge, using di erent geometry in their sensing element, dictates that the serpentine shaped element has the largest step of resolution with 116.82 m, while the lowest value belongs to the block shaped with 2.73 m. The sensitivities are $1.06mV$ m, $0.66mV$ m, and $0.22mV$ m for serpentine shaped, U-shaped and block shaped geometries, respectively. Considering, the precision as the key parameter, we observe that the block shaped is the best option for the application.

Chapter 6

Voltage Reference Circuit

An ideal current or voltage reference is independent of power supply and temperature. Many analog circuits require a building block, which provides a stable current or voltage regardless of variations in power supply and temperature. The term reference is used when the current or voltage values have more precision and stability than ordinarily found in a source. A source is typically dependent on the load connected to it. Therefore, a bu er ampli er can isolate the reference from the load and still maintaining its performance.

This chapter, presents the design of a circuit to drive our Wheatstone bridge proposed on Chapter 5, taking advantage of bene ts that Voltage BandGap references have. The goal is to design a BGR architecture using only CMOS compatible technology.

6.1 Voltage Reference

The bandgap voltage reference (BGR) circuit is widely used in analog and digital circuits. The BGR circuit is the key design in analog circuits to provide a stable voltage reference with low sensitivity to temperature and supply voltage. Most BGR use bipolar junction transistors (BJT) to reduce the temperature dependence, because their good performance in terms of temperature coe cients. However, by continuing in CMOS process, our purpose is to propose a design of a bandgap voltage reference to serve as the voltage supply of the resistive bridge already characterized in previous chapters.

This bandgap voltage reference should use only MOSFET transistors. A P-MOS and N-MOS based references are analyzed in same detail and their sensitivities are evaluated to select the best design for our application. Only MOSFETs devices are considered in the bandgap voltage reference circuit to reduce the operating voltage/power making it compatible with MEMS technology.

6.2 Traditional Bandgap Reference Circuit in CMOS

A traditional implementation of bandgap voltage reference in CMOS technology is shown in Figure 6.1 [71].

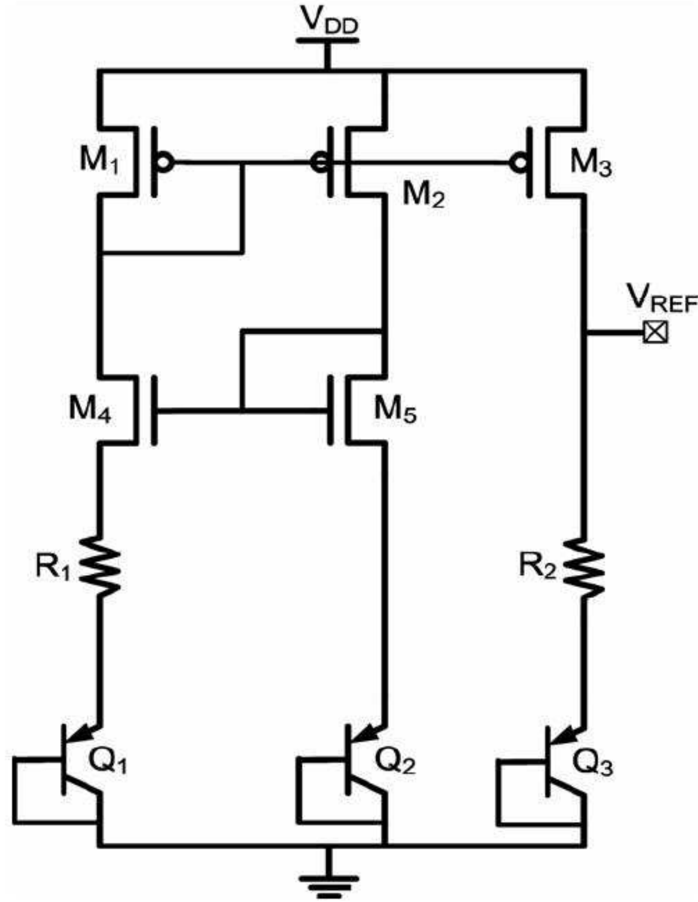

Figure 6.1: Traditional bandgap voltage reference circuit

In this circuit, the output voltage, also called V_{ref} is the sum of a base-emitter voltage (V_{EB}) of BJT Q_3 and the voltage drop across the upper resistor R_2. The BJTs (Q_1, Q_2, and Q_3) are typically implemented by the diode-connected parasitic vertical PNP bipolar junction transistors in CMOS process with the current proportional to $exp^{(V_{EB} \;\, V_T)}$, where V_T $(= \;\; T \;\, q)$ is the thermal voltage. Under constant current bias, V_{EB} is strongly dependent on V_T as well as temperature. The current mirror (formed by M_1, M_2, and M_3) is designed to bias Q_1, Q_2, and Q_3 with identical current. Then, the voltage drop on the resistor R_1 can be expressed by:

$$V_{R1} = V_T \quad ln \quad \frac{A_1}{A_2} \tag{6.1}$$

where A_1 and A_2 are the emitter areas of Q_1 and Q_2 respectively. It is noted that the voltage in R_1 exhibits a positive temperature coefficient when A_1 is larger than A_2. Besides, since the current flows through R_1 is equal to the current flows through R_2, the output voltage of the traditional bandgap voltage reference circuit can be expressed as:

$$V_{REF} = V_{EB3} + \frac{R_2}{R_1} V_T \quad ln \quad \frac{A_1}{A_2} \tag{6.2}$$

The second term in Equation (6.2) is proportional to the absolute temperature (PTAT), which is used to compensate the negative temperature coefficient of V_{EB3}. In overall, the PTAT voltage comes from the thermal voltage V_T with a temperature coefficient about $+0\ 085mV \quad C$ in CMOS technology, which is quite smaller than that of V_{EB}. After multiplying the PTAT voltage with an appropriate factor $(R_2 \quad R_1)$ and summing with V_{EB}, the output voltage V_{REF} of bandgap reference circuit can result in very low sensitivity with respect to temperature.

6.3 Design of Bandgap Voltage Reference

From the analysis on traditional bandgap voltage reference circuit, it has been known that the realization of bandgap voltage reference circuit strongly depends on the temperature coefficient of BJTs. It is said in other words, the exponential term $e^{(V_{EB} \quad V_T)}$ in the Current-Voltage relationship (I-V) of BJTs makes it possible to obtain a PTAT voltage from the voltage difference between a large-area BJT and a small-area BJT.

In the linear region of operation, the drain current of a polysilicon thin-film transistor with channel length L and width W can be expressed as [72]

$$I_D = \frac{W}{L} \quad _0 q V_D \tag{6.3}$$

where $_0$ is the carrier mobility within the grain, V_D is the drain voltage and q is the effective gate-induced free charge per unit area. For large grain polysilicon thin-film transistors, for example L , where L is the channel length and represents the width of the depletion region at the grain boundary, the drain current can be described by the relationship [72]:

$$I_D = \frac{W}{L} \quad _0 C_{ox}(V_G \quad V_T)V_D \tag{6.4}$$

According to [71], the drain current (I_{DS}) of devices operated in the saturation region can be expressed as

$$I_{DS} = \frac{W}{2L} \;{}_0C_{ox}(V_{GS} \quad V_{TH})^2 \;\; exp \quad \frac{V_B}{V_T} \tag{6.5}$$

where ${}_0$ is the carrier mobility within the grain, L denotes the e ective channel length, W is the e ective channel width, C_{ox} is the gate oxide capacitance per unit area, V_{TH} is the threshold voltage of the MOSFET device, and V_{GS} is the gate-to-source voltage of the MOSFET device. V_B is the potential barrier at grain boundaries which is associated with the crystallization quality of the poly-Si lm.

Under small V_{GS}, V_B is large. When the V_{GS} increases, V_B decreases rapidly. When the devices are operated under small V_{GS}, it is found that the drain current I_{DS} of devices is dominated by the exponential term and can be estimated by the following expression [71]

$$I_{DS} = W \quad exp^{(\;\frac{V_B}{V_T})} \tag{6.6}$$

where is treated as a constant under small gate bias (V_{GS}). Then, the equation for V_B can be written as:

$$V_B = V_T \;\; ln \;\; \frac{W}{I_{DS}} \quad = \frac{{}_BT}{q} ln \;\; \frac{W}{I_{DS}} \tag{6.7}$$

where ${}_B$ is the Boltzman s constant, T represents the room temperature. When there is a variation of temperature T, the corresponding variation of V_B is depicted by:

$$V_B = \frac{{}_B \;\; T}{q} ln \;\; \frac{W}{I_{DS}} \tag{6.8}$$

Analyzing Equation (6.8), it can be found that the temperature coe cient (TC) of V_B can be modulated by the channel width. The larger channel width gives rise to the larger TC of V_B. The bandgap voltage reference using MOSFET devices can be implemented in Figure 6.2.

Figure 6.2: Schematic diagram of the proposed bandgap voltage reference.

In this design, the MOSFET devices, M_1, M_2, M_3, M_4, and M_5 are biased in saturation region. The diode-connected BJTs in traditional CMOS bandgap voltage reference circuit (see Figure 6.1) are also biased in saturation region. The nodes n_1 and n_2 are designed to have equal potential by the current mirror circuit.

Also, the channel width of M_6 (W_6) is larger than the channel width of M_7 (W_7), so the temperature coe cient of M_6 is more negative than the temperature coe cient of M_7. The voltage drop across the resistor R_1 (V_{R1}) therefore presents a positive temperature coe cients. If the dependence of m on V_{GS} is neglected, the variation of V_R1 (V_{R1}) as a function of T can be written as

$$V_{R1} = \frac{{}_B\ T}{mq} ln \frac{W_6}{W_7} = \frac{{}_B\ T}{mq} ln(N) \tag{6.9}$$

where $N = W_6 \ W_7$, is the channel width ratio of M_6 and M_7, m is the absolute value of the slope under linear approximation of the variation of V_B versus the variation of V_{GS}, and V_T is the thermal voltage. The current mirror, which is composed of M_1, M_2, and M_3 provides equal currents in these three branches I_1, I_2, and I_3 of the circuit. The output voltage, V_{REF} is the sum of a gate-source voltage of the MOSFET M_8 (V_{GS8}) and the voltage drop across the upper resistor (V_{R2}). Therefore, the output voltage variation (V_{REF}) of the bandgap voltage reference circuit proposed can be expressed as [71]

$$V_{REF} = \quad I_3 R_2 + \quad V_{GS8} = \frac{R_2}{R_1} \frac{{}_B \ T}{mq} ln(N) + \quad V_{GS8} \tag{6.10}$$

Where R_1 and R_2 are the resistors shown in Figure 6.2. The rst term in Equation (6.10) with the positive temperature coe cient is proportional to the absolute temperature (PTAT), which is used to compensate the negative temperature coe cient of V_{GS8}. After multiplying the PTAT voltage with an appropriate factor (proper ratio of resistors) and summing with V_{GS8}), the output voltage of bandgap reference circuit can result in very low sensitivity to temperature.

6.3.1 Simulating Bandgap Voltage Reference 1

In order to state above explained, several simulations were performed using Electric VLSI [73], and LT Spice [74], to obtain the performance of the bandgap voltage reference designed. The scale used in Electric VLSI was $300nm$, where the minimum channel length is $L = 0\ 6\ \ m$, while minimum channel width is $W = 3\ \ m$. Considering the BSIM 3 models for ON semiconductor s C5 process.

6.3.1.1 BGR1 Case I

This rst design considers PMOS transistors as the diode-connected devices under the current mirror, as depicts the following Figure 6.3. The dimensions of the MOSFETs devices and the values of the resistors are illustrated in Table 6.1

Table 6.1: Dimensions of the MOSFET devices and resistor value in Bandgap voltage reference 1, case I.

MOSFET device	Channel Length L	Channel Width W
M1, M2, M3, M4, M5, M7, M8	0.6 m	3 m
M6	0.6 m	30 m

Resistor	Value
R_1	$1M$
R_2	$1K$

As R_2 is equal to $1K$ and R_1 is equal to $1M$. The ratio R_2 R_1 is equal to 1 10^{3}.

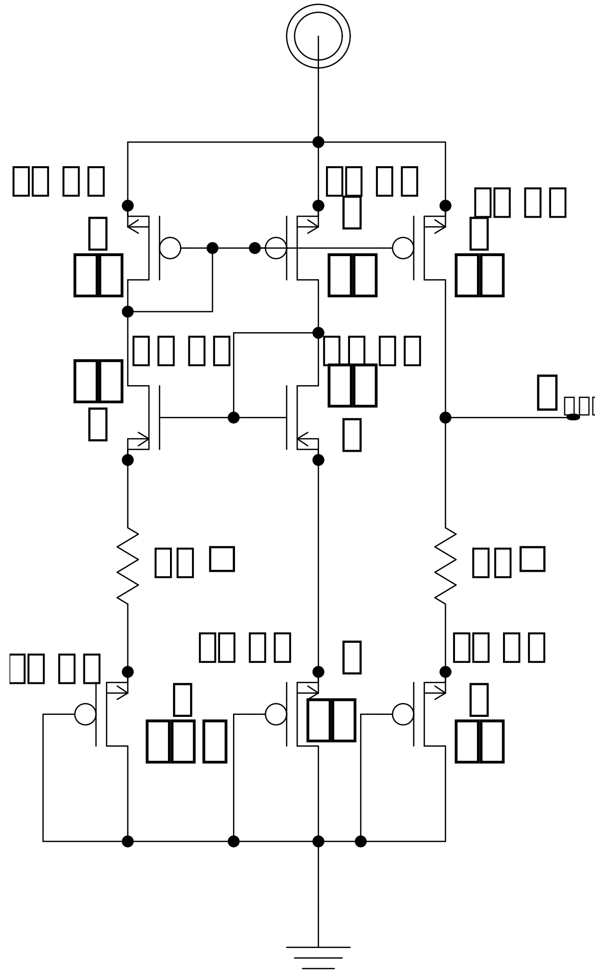

Figure 6.3: Schematic diagram of the BGR 1 using P-channel MOSFETs as diode-connected for case I.

From the Figure 6.3 it is observed that the MOSFET device that has the largest area is M6, as mentioned in the operation of the circuit, then the output voltage obtained after

doing a parametric sweep analysis in the power supply from 0 VDC to 25 VDC and a parametric sweep in temperature from 25 C to 125 C, are presented in Figure 6.4.

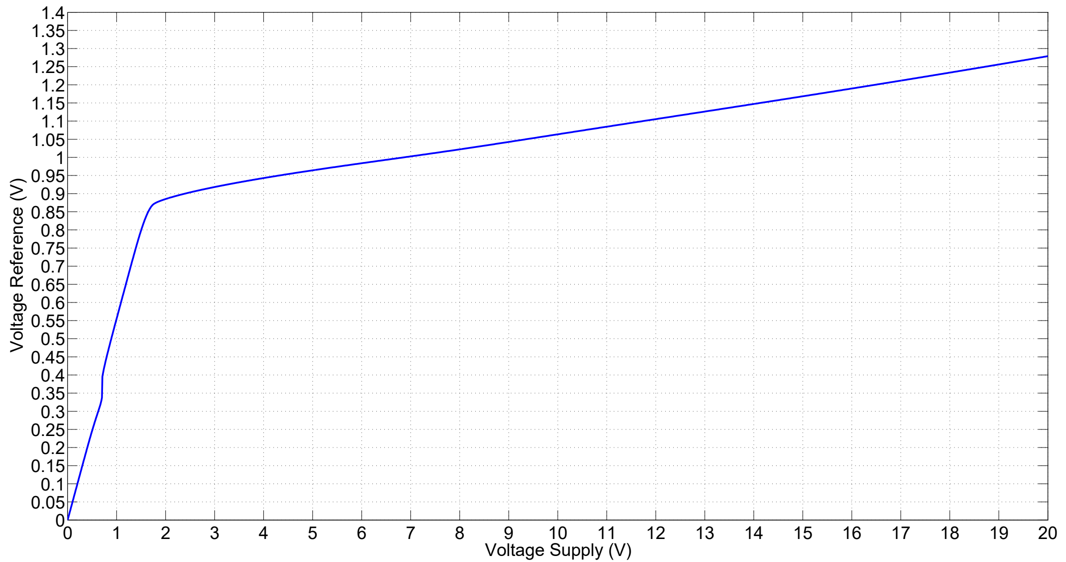

(a) Response of the bandgap voltage reference 1 to power supply changes, case I.

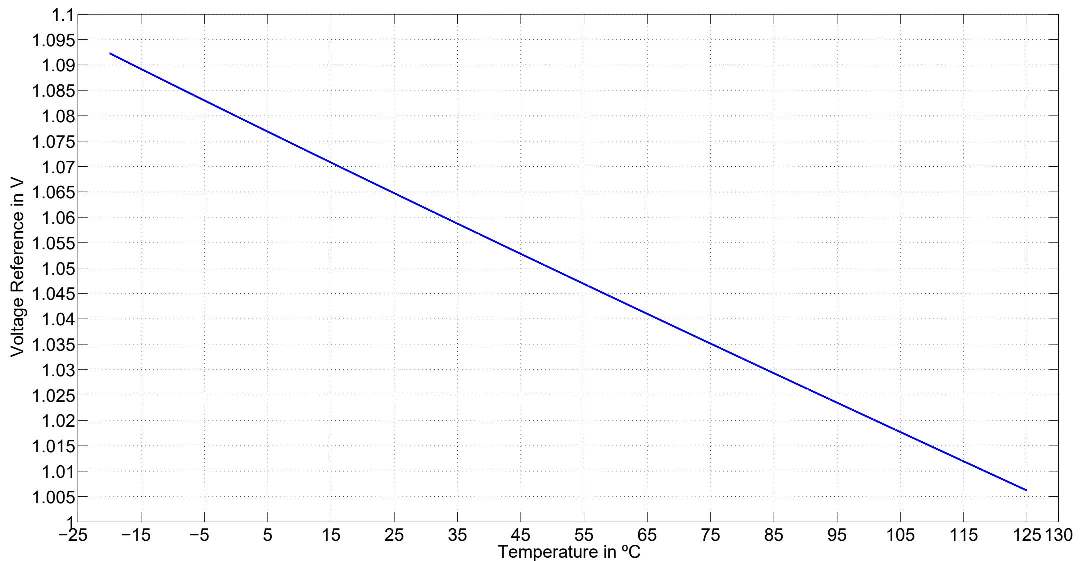

(b) Response of the bandgap voltage reference 1 to temperature changes, case I.

Figure 6.4: Simulations results of the bandgap voltage reference 1, case I.

From the response of the bandgap voltage reference 1 to power supply changes, it can be observed a low sensitivity to power supply changes in the range of $V_{supply} = 1\ 73V$ to $V_{supply} = 20V$. During this range of voltage, the output voltage is changing from

$V_{REF} = 868\ 129mV$ to $V_{REF} = 1\ 278V$. An increasing in the output voltage is evident as long as the power supply is increasing also. Resulting in a change of voltage of $V_{REF} = 409\ 871mV$, exhibiting a sensitivity with respect to power supply changes of $22\ 43mV\ \ V$. All these results were obtained considering a temperature room of $25\ \ C$.

In addition, the response to temperature changes of the bandgap voltage reference is presented in Figure 6.4(b), it is observed a range of temperature considered from $20\ \ C$ to $125\ \ C$, resulting an output voltage range from $V_{REF} = 1\ 095V$ to $V_{REF} = 1\ 009V$. The value of voltage change is $V_{REF} = 86\ 38mV$ and the output voltage at $25\ \ C$ is $V_{REF}(25\ \ C) = 1\ 064V$. A power supply of $V_{supply} = 10V$ was considered for these results.

Considering the coe cient of temperature that exhibits this bandgap voltage reference, we can write

$$TC(V_{REF}) = 10^6 \ \ \frac{V_{REF}\ \ V_{REF}}{T} \quad in\ \ (ppm\ \ \ C) \tag{6.11}$$

By applying Equation (6.11) to results:

$$TC(V_{REF}) = 10^6 \ \ \frac{86\ 38 \ \ \ 10\ \ ^3V\ \ 1\ 064V}{145\ \ C} \quad 560\, ppm\ \ \ C$$

This is the coe cient of temperature of this bandgap voltage reference, this parameter describes the ability of the bandgap voltage reference to keep constant the output voltage with respect to temperature changes. It can be concluded that it does not exhibits a good temperature coe cient if our platform sensing will be under temperature environment changes beyond to the range studied.

6.3.1.2 BGR1 Case II

However, modifying the ratio of $R_2\ \ R_1$ by changing the values of resistances as $R_2 = 1K$, while $R_1 = 100K$. Hence the ratio of $R_2\ \ R_1 = 0\ 01$. Also, the channel width of $M6$ was changed from $30\ \ m$ to $60\ \ m$ and the channel width of $M8$ from $3\ \ m$ to $60\ \ m$. Table 6.2 illustrates the new parameters of the transistors and resistors considered for this new case. Then, the results of a parametric sweep in power supply and temperature are shown in Figure 6.5.

Table 6.2: Dimensions of the MOSFET devices and resistor value in Bandgap voltage reference 1, case II.

MOSFET device	Channel Length L	Channel Width W
M1, M2, M3, M4, M5, M7	0.6 m	3 m
M6, M8	0.6 m	60 m

Resistor	Value
R_1	$100K$
R_2	$1K$

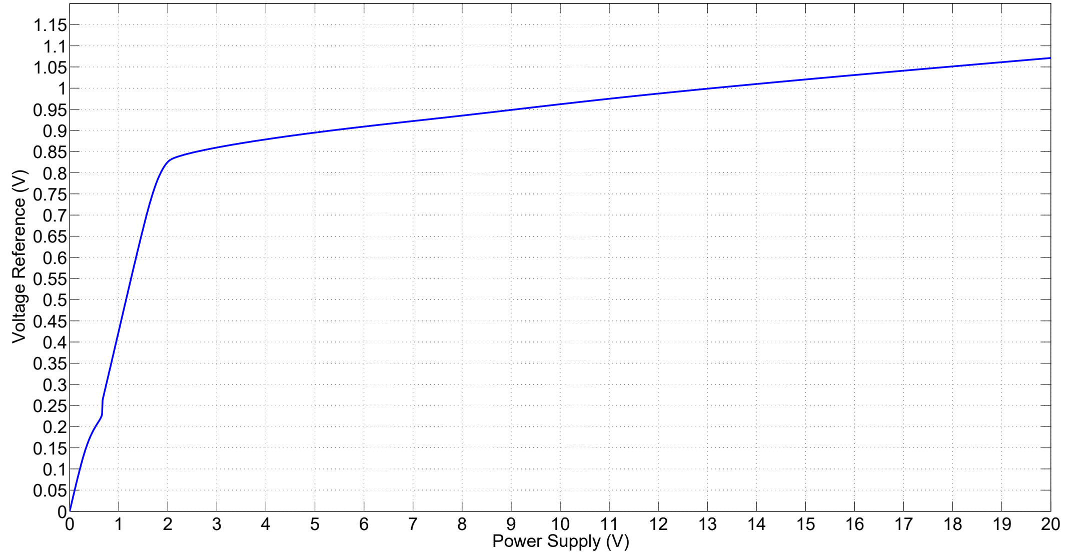

(a) Response of the bandgap voltage reference 1 to power supply changes, case II.

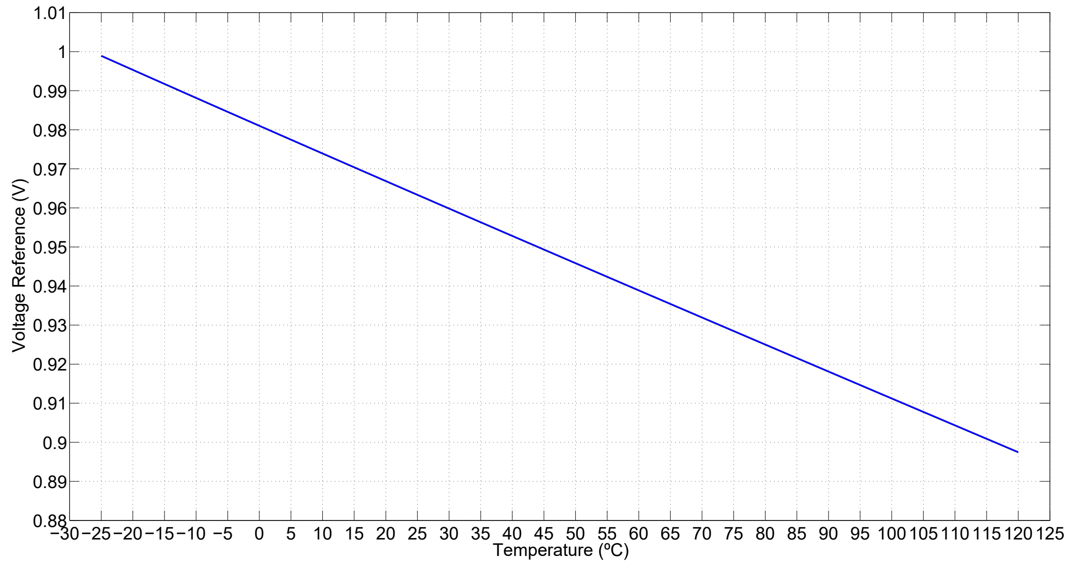

(b) Response of the bandgap voltage reference 1 to temperature changes, case II.

Figure 6.5: Simulations results of the bandgap voltage reference 1, case II

Figure 6.5(a) shows the response of the bandgap voltage reference to power supply changes. By inspection of the curve, it can be observed that the sensitivity to power supply changes is lower than the rst case. The range of power supply voltage in where the bandgap voltage reference presents a low sensitivity to power supply changes is from $V_{supply} = 2V$ to $V_{supply} = 20V$. For this range of power supply voltage, the minimum output voltage is $V_{REF} = 825\ 519mV$, while the maximum output voltage is $V_{REF} = 1\ 0712V$. The change of output voltage is $V_{REF} = 245\ 681mV\ \ V$.

From this curve of response to power supply changes, the sensitivity is $13\ 64mV\ \ V$. It is a better value in comparison with the rst sensitivity with respect to power supply changes obtained of $22\ 48mV\ \ V$.

On the other hand, from the curve of voltage reference response to temperature changes, it is observed that the change in temperature $T = 145\ \ C$. The minimum output voltage is $V_{REF} = 897\ 453mV$, while the maximum output voltage is $V_{REF} = 998\ 935mV$. The output voltage at room temperature is $V_{REF}(25\ \ C) = 963\ 344mV$, the change in output voltage is $V_{REF} = 101\ 482mV$. Also, from the graphical information obtained from Figure 6.5(b), the sensitivity to temperature changes of the bandgap voltage reference is veri ed. Considering those changes in the circuit, the new temperature coe cient can be re-calculated using Equation (6.11) as following:

$$TC(V_{REF}) = 10^6 \quad \frac{101\ 482 \quad 10^{\ \ 3}V\ 963\ 344 \quad 10^{\ \ 3}V}{145\ \ C} \quad 727\, ppm \quad C$$

This new temperature coe cient obtained, $727\, ppm\ \ C$, is not better than the previous one, $559\, ppm\ \ C$. But, the sensitivity with respect to power supply changes was improved from $23\ 168mV\ \ V$ to $13\ 21mV\ \ V$ with respect to power supply changes.

Now, we will change the design, also by using P-channel transistors as diodes but adding a second phase of MOSFET transistors in the current mirror. The new bandgap voltage reference design using P-channel transistors is presented next.

6.3.2 Simulating Bandgap Voltage Reference 2

This section presents a new design of voltage bandgap reference using P-channel devices as diodes. Figure 6.6 depicts the schematic diagram of this new circuit.

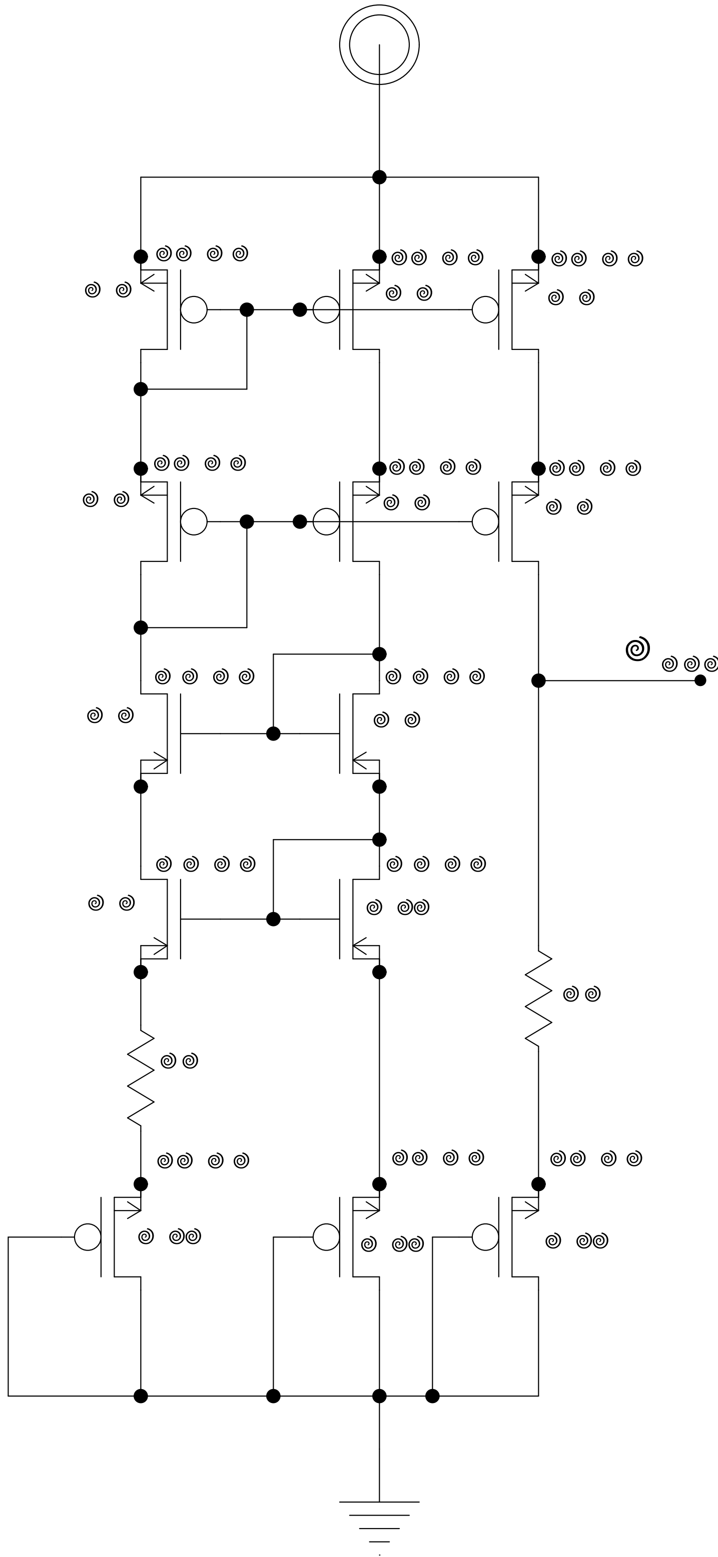

Figure 6.6: Schematic diagram of the BGR 2 using P-channel MOSFETs as diode-connected.

From this new schematic diagram, it is using a new current mirror, unlike the circuit 1 of bandgap voltage reference where is used a current mirror with 4 MOSFET transistors, here, the only change was the use of two phases of MOSFETs devices in the current mirror. MOSFETs devices $M4$, $M5$, $M9$, and $M10$ are forming the second phase of transistors in the current mirror.

6.3.2.1 BGR2 Case I

This new design of bandgap voltage reference uses the diode-connected device as well. The values of resistors are $R_1 = 600K$, $R_2 = 1\ 2M$. Hence the ratio of $R_2\ R_1 = 2$. The dimensions of the MOSFET devices and resistors values are summarized in Table 6.3.

Table 6.3: Dimensions of the MOSFET devices and resistor value in Bandgap voltage reference 2, case I.

MOSFET device	Channel Length L	Channel Width W
M1, M2, M3, M4, M5, M6, M7, M8, M9, M10, M12, M13	0.6 m	3 m
M11	0.6 m	30 m

Resistor	Value
R_1	$600K$
R_2	$1\ 2M$

The Figure 6.7 depicts the performance of the bandgap voltage reference to power supply and temperature changes.

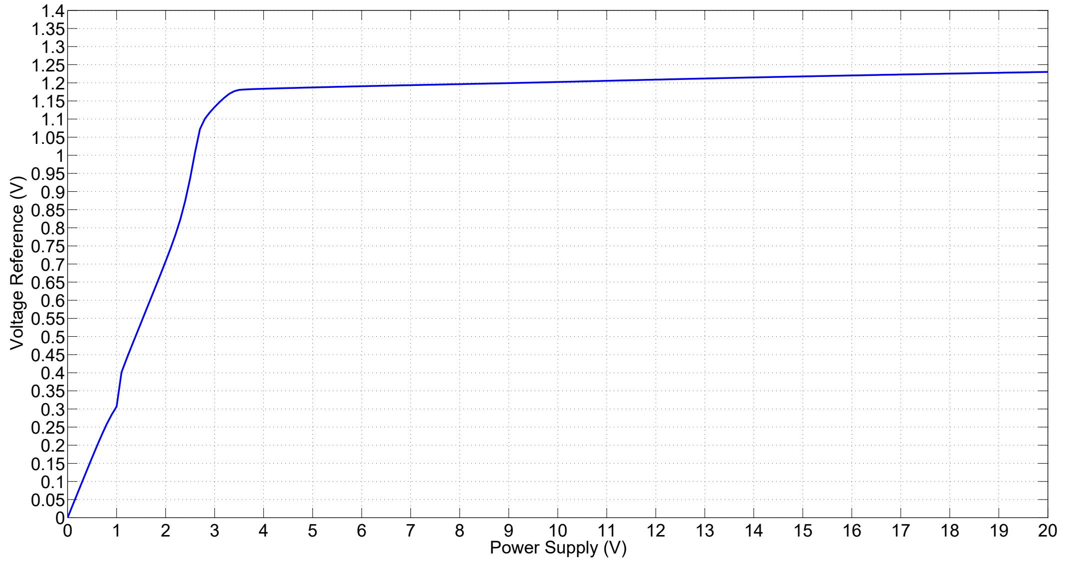

(a) Response of the bandgap voltage reference 2 to power supply changes, case I.

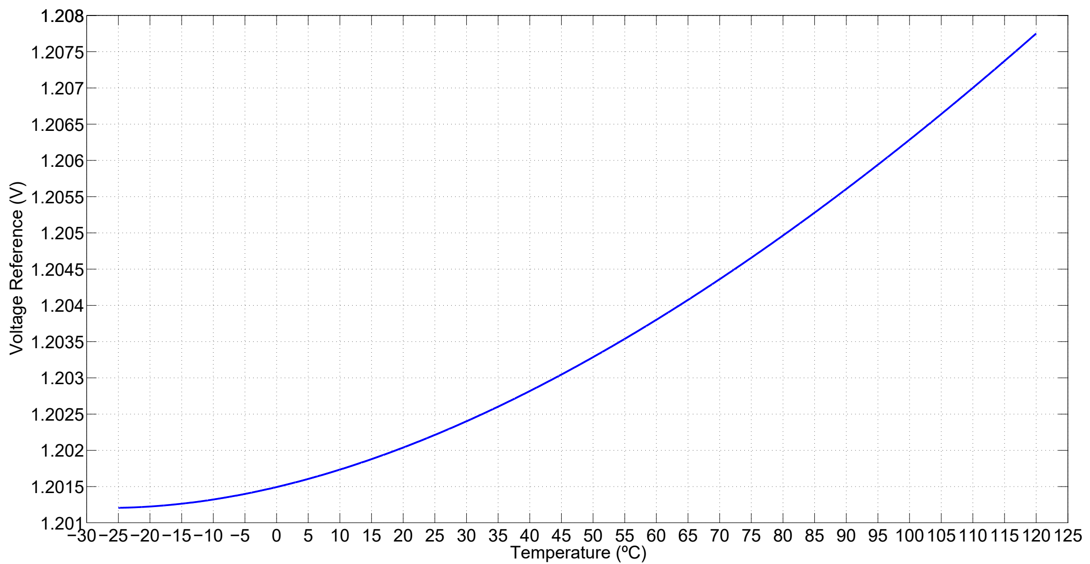

(b) Response of the bandgap voltage reference 2 to temperature changes, case I.

Figure 6.7: Simulations results of the bandgap voltage reference 2

As the previous circuit, it was considered for the response of the bandgap voltage reference, a parametric sweep analysis in the power supply, changing it from $V_{supply} = 0V$ to $V_{supply} = 20V$, at temperature room of 25 C. From the Figure 6.7(a), it can be observed that at a value of $V_{supply} = 3\ 533V$ in the power supply, the output voltage reaches the value of $V_{REF} = 1\ 181V$. The increasing in the power supply causes an

slightly rise in the output voltage of the circuit to $V_{REF} = 1\ 23V$ when the power supply reaches the its maximum value of $V_{supply} = 20V$. The change in output voltage is $\ V_{REF} = 49mV$. In that range of voltage, the slope of the curve is 0 002778. That means that the sensitivity, with respect to power supply changes, of this bandgap voltage reference is of 2 778$mV\ \ V$.

Furthermore, the response of this bandgap voltage reference to changes in temperature is depicted by Figure 6.7(b), where a lower sensitivity to temperature is observed. The maximum value of $V_{REF} = 1\ 2077V$, while the minimum value is $V_{REF} = 1\ 2012V$. Consequently, the change in output voltage is $\ V_{REF} = 6\ 544mV$, the output voltage at room temperature is $V_{REF}(25\ \ C) = 1\ 202V$, and the temperature coe cient of this circuit is calculated as following:

$$TC(V_{REF}) = 10^6 \ \frac{6\ 544 \quad 10\ ^{3}V\ 1\ 202V}{145\ \ C} \quad 38\,ppm \quad C$$

This value of temperature coe cient is lower in relation with the temperature coe cient reached with the bandgap voltage reference in circuit 1.

6.3.2.2 BGR2 Case II

Now, the changes performed in the circuit are: $R_2 = 600K$, $R_1 = 300K$, and the new channel width of $M_1 1$, and $M13$ is 60 m. Table 6.3 illustrates the changes in the dimensions of the MOSFETs of the circuit and the values of the resistances. With these modi cations, a new parametric sweep analysis in temperature was carried out, and the results are illustrated by Figure 6.8.

Table 6.4: Dimensions of the MOSFET devices and resistor value in Bandgap voltage reference 2, case II.

MOSFET device	Channel Length L	Channel Width W
M1, M2, M3, M4, M5, M6, M7, M8, M9, M10, M12	0.6 m	3 m
M11, M13	0.6 m	60 m

Resistor	Value
R_1	$300K$
R_2	$600K$

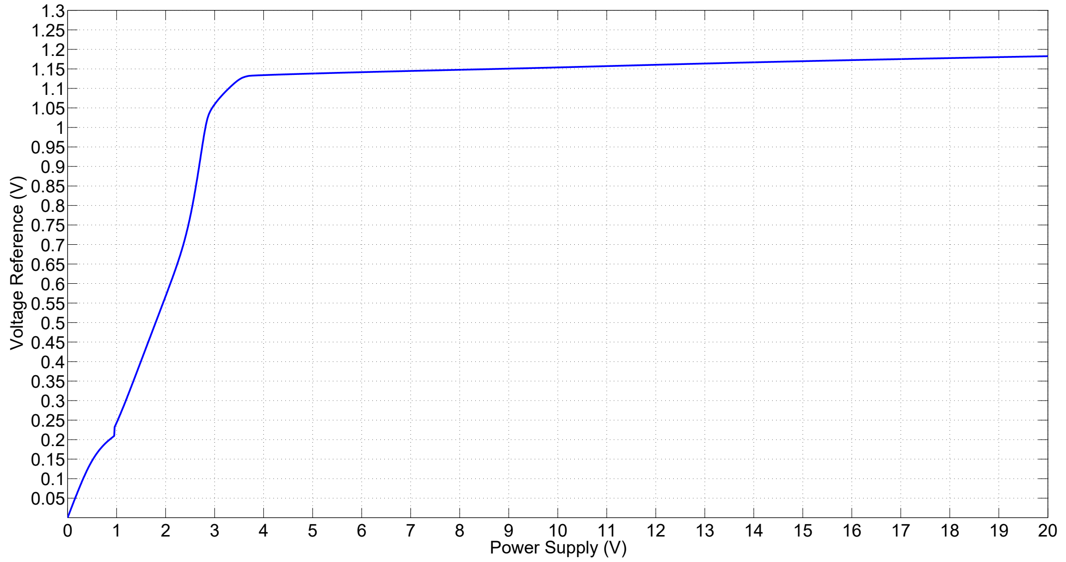

(a) Response of the bandgap voltage reference 2 to power supply changes, case I.

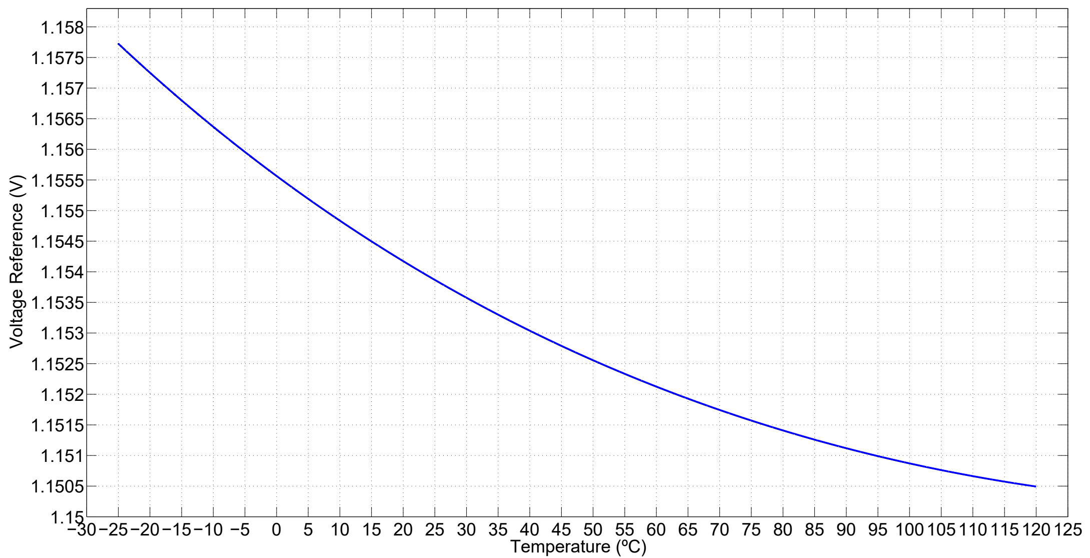

(b) Response of the bandgap voltage reference 2 to temperature changes, case II.

Figure 6.8: Simulations results of the bandgap voltage reference 2, case II.

From Figure 6.8(a) it is observed that the region of low sensitivity with respect to power supply changes begins at $V_{supply} = 3\ 71V$ to $V_{supply} = 20V$, the minimum output voltage is $V_{REF} = 1\ 132V$, while the maximum output voltage is $V_{REF} = 1\ 182V$. Therefore, a relative output voltage change is $V_{REF} = 50\ 3mV$, consequently, the sensitivity of the bandgap voltage reference with respect to power supply changes is $3\ 09mV\ V$. This

value is a little bit more higher than the previous value of sensitivity $2\ 778mV\ \ V$.

Whereas, from Figure 6.8 it is observed that this design of bandgap voltage reference has a better independence of temperature in comparison of rst simulation of this circuit. The minimum output voltage is $V_{REF} = 1\ 15V$, while the maximum output voltage is $V_{REF} = 1\ 157V$. That provides an output voltage change of $\ V_{REF} = 7\ 231mV\ \ V$. The output voltage at room temperature is $V_{REF}(25\ \ C) = 1\ 153V$. The temperature coe cient can be calculated by

$$TC(V_{REF}) = 10^6 \ \frac{7\ 231 \quad 10^{\ 3}V\ \ 1\ 153V}{145\ \ C} \quad 43\,ppm \quad C$$

This coe cient of temperature, $TC(V_{REF}) = 43\,ppm \quad C$, is not lower than the previous temperature coe cient obtained, $TC(V_{REF}) = 38\,ppm \quad C$.

6.3.2.3 BGR2 Case III

But the following change in the circuit is to incrementing the channel width of $M11$ and $M13$, the value of R_2 and R_1 as well. Table 6.5 illustrates the new parameters of the bandgap voltage reference.

Table 6.5: Dimensions of the MOSFET devices.

MOSFET device	Channel Length L	Channel Width W
M1, M2, M3, M4, M5, M6, M7, M8, M9, M10, M12,	$0.6\ \ m$	$3\ \ m$
M11	$0.6\ \ m$	$120\ \ m$
M13	$0.6\ \ m$	$90\ \ m$

Resistor	Value
R_1	$600K$
R_2	$1\ 2M$

From Table 6.5 it can be observed a ratio of channel width in the transistor $M11$ with respect the others of 40:1, while the ratio of channel width between the transistor $M13$ with respect to the rest of devices that form the current mirror is of $30 : 1$. The ratio of $R_2\ \ R_1 = 2$. Figure 6.9 depicts the simulation results of this new bandgap voltage reference.

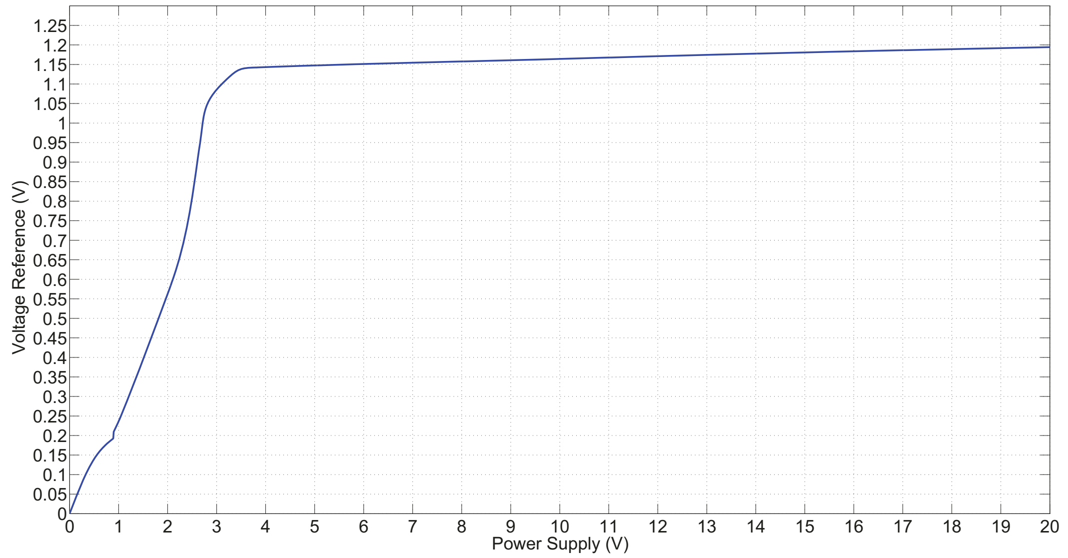

(a) Response of the bandgap voltage reference 2 to power supply changes

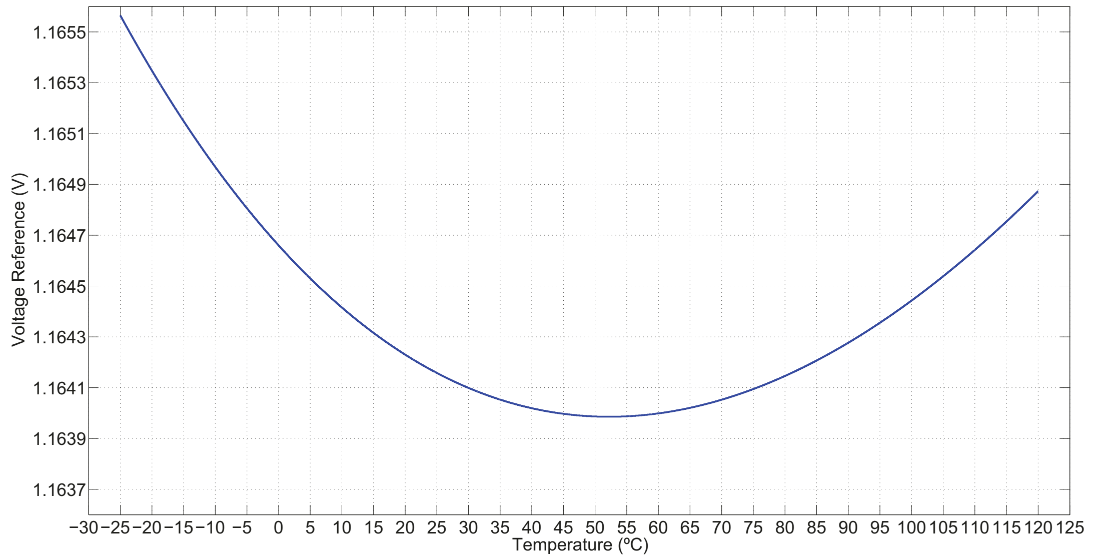

(b) Response of the bandgap voltage reference 2 to temperature changes

Figure 6.9: Simulations results of the bandgap voltage reference 2

From Figure 6.9(a) it is observed that the low sensitivity to power supply changes of the bandgap voltage reference begins at $V_{supply} = 3.586V$ and ends to $V_{supply} = 25V$. The minimum output voltage in that range is $V_{REF} = 1.141V$, while the maximum output voltage is $V_{REF} = 1.194V$. Therefore, this design of bandgap voltage reference has a sensitivity to power supply changes of $3.27mV/V$.

In the context of independence of temperature changes, Figure 6.9(b) shows that the minimum value of the output voltage is $V_{REF} = 1\ 164V$ at temperature of $50\ \ C$, while the maximum output voltage is $V_{REF} = 1\ 165V$ at temperature of $\ \ 25\ \ C$. This range of output voltage is reached by doing a parametric analysis in temperature from $\ \ 25\ \ C$ to $120\ \ C$. The output voltage at room temperature is $V_{REF}(25\ \ C) = 1\ 1641V$. The coe cient of temperature of this bandgap voltage reference can be estimated as

$$TC(V_{REF}) = 10^6 \ \ \frac{1\ 57 \quad 10\ ^3V\ 1\ 1641V}{75\ \ C} \quad 18\,ppm \quad C$$

Stating that this last circuit of bandgap voltage reference has the lowest sensitivity to temperature changes of $18\,ppm \quad C$, while the sensitivity to power supply changes is of $3\ 27mV\ \ V$.

A summary of results of these bandgap voltage reference are presented in next section.

6.4 Discussion

Two circuits structures are proposed as bandgap voltage references, circuit 1 using MOSEFT type P as diode-connected device (BGR1), and the circuit 2 using MOSFET type P as diode-connected device and two phases of transistors in the current mirror (BGR2).

Design of BGR1 includes two cases: case I (see Table 6.1) uses a channel width for $M6$ of $30\ \ m$ while for $M8$ a channel of $3\ \ m$. Also it uses a ratio of $R_2\ \ R_1 = 1 \quad 10\ ^3$. And case II (see Table 6.2) uses a channel width for $M8$ and $M6$ of $60\ \ m$ and a ratio of $R_2\ \ R_1 = 0\ 01$.

Design of BGR2 includes three cases: case I (see Table 6.3) uses a channel width for $M11$ of $30\ \ m$, for the rest of MOSFET devices uses a channel width of $3\ \ m$, and for the ratio of $R_2\ \ R_1$ considers a value of 2. There is a case II (see Table 6.4) where is considered for $M11$ and $M13$ a channel width of $60\ \ m$ while for the rest of the MOSFET devices is used a channel width of $3\ \ m$, and a value of 2 as well for the ratio of $R_2\ \ R_1$. Then, a case III (see Table 6.5) is studied for the design BGR2 which uses a channel width of $120\ \ m$ for $M11$, a channel width of $90\ \ m$ for $M13$ and for the rest of MOSFET devices in the design considers a channel width of $3\ \ m$. In this case III, the ratio $R_2\ \ R_1$ is also the same value of 2.

Table 6.6 shows a comparison of performances by the two BGR s. The table illustrates simulations results from Electric VLSI and LT Spice.

Table 6.6: Comparison of performance of BGRs

	BGR1		BGR2		
Parameter	Case 1	Case 2	Case 1	Case 2	Case 3
TC(V_{REF})	$560\,ppm \quad C$	$727\,ppm \quad C$	$38\,ppm \quad C$	$43\,ppm \quad C$	$18\,ppm \quad C$
Line Regulations	$22\ 43mV\ \ V$	$13\ 64mV\ \ V$	$2\ 77mV\ \ V$	$3\ 09mV\ \ V$	$3\ 27mV\ \ V$

After analyzing the performance of each bandgap voltage reference proposed and studied, our best choice for this application should be BGR2, Case III, because its best temperature coe cient and line regulation: $18\,ppm \quad C$ and $3\ 27mV\ \ V$.

This design uses a MOSFET device type P. This con guration provides a temperature coe cient which is located in the state-of-the-art top voltage reference available in the current literature [75], [76],[77], [78].

Chapter 7

Conclusions

In this thesis work, we have proposed a monolithic biosensing platform based on commercial CMOS processes, consisting of a microcantilever, an embedded piezoresistor and the instrumentation electronics.

We have described the static mode operation of cantilever-based biosensors using adsorption-induced surface stress. A compilation of several analytical models of adsorption-induced surface stress in microcantilevers has been presented. These models describe, from different perspectives, the surface stress induced by the analyte-bioreceptor interaction over the microcantilever resulting in beam deflection.

In the context of the bending as a result of the surface stress, it has been studied the contribution of residual stress in beam deflection. A novel technique to model residual stress in multilayered beams has been proposed and validated by comparing experimental and simulation deflections of fourteen composite beams, obtaining an average of 27% absolute error.

Main contributions of this thesis work are:

1. A model that reproduces residual stress in multilayer beams. It is expected this model will ease future design of cantilever-based micromachined devices.
2. A complete model of a monolithic sensor including mechanical beams, piezoresistive elements and electronics. This global model will improve design process allowing faster optimization cycles.

7.1 Future Work and Directions

Concerning the proposed model of residual stress in multilayer microcantilevers, further improvements could be achieved by incorporating the rotation angle that the beams exhibit at the end where these are anchored to the substrate.

In this work two different CMOS processes have been used, one for the cantilevers and the other one for the electronics. A monolithic prototype will require redesign of one of these components.

Current work in our group is aimed to selectively deposit an active layer over the beams. It is expected this configurable-by-active-layer platform can be used in the future to detect and quantify different analytes for environmental monitoring, food industry and biomedical applications.

Appendix A

Complements

A.1 Piezoresistive Transduction in CMOS-based Microantilever sensor

For a 3-dimensional anisotropic crystal, the electric field is related to the current-density field by a 3-by-3 resistivity tensor as:

$$\begin{pmatrix} E_x \\ E_y \\ E_z \end{pmatrix} = \begin{pmatrix} \rho_{xx} & \rho_{xy} & \rho_{xz} \\ \rho_{yx} & \rho_{yy} & \rho_{yz} \\ \rho_{zx} & \rho_{zy} & \rho_{zz} \end{pmatrix} \begin{pmatrix} I_x \\ I_y \\ I_z \end{pmatrix} \tag{A.1}$$

Or by a 3-by-3 conductivity tensor

$$\begin{pmatrix} I_x \\ I_y \\ I_z \end{pmatrix} = \begin{pmatrix} \sigma_{xx} & \sigma_{xy} & \sigma_{xz} \\ \sigma_{yx} & \sigma_{yy} & \sigma_{yz} \\ \sigma_{zx} & \sigma_{zy} & \sigma_{zz} \end{pmatrix} \begin{pmatrix} E_x \\ E_y \\ E_z \end{pmatrix} \tag{A.2}$$

Using more compact notation

$$\vec{E} = \rho \cdot \vec{I} \tag{A.3}$$

$$\vec{I} = \sigma \cdot \vec{E} \tag{A.4}$$

Where $\vec{E}$ and $\vec{I}$ are the electric field vector and electric current density vector, and ρ and σ the electrical resistivity and conductivity tensors, respectively.

Since piezoresistive theory describes the change in the resistivity tensor, the conductivity tensor is dropped from now on, and the following analysis focuses on the resistivity tensor.

The piezoresistive coefficients of a doped single-crystal silicon piezoresistor are influenced by its relative orientation to crystallographic directions [79].

Using the Onsager's theorem [80], in single crystal material the nine components of both the electrical conductivity and the resistivity tensors always reduce to six value arranged in a symmetric tensor. By using the notations of $\rho_1 = \rho_{xx}$, $\rho_2 = \rho_{yy}$, $\rho_3 = \rho_{zz}$, $\rho_4 = \rho_{yz}$, $\rho_5 = \rho_{zx}$, and $\rho_6 = \rho_{xy}$:

$$\begin{pmatrix} E_x \\ E_y \\ E_z \end{pmatrix} = \begin{pmatrix} \rho_1 & \rho_6 & \rho_5 \\ \rho_6 & \rho_2 & \rho_4 \\ \rho_5 & \rho_4 & \rho_3 \end{pmatrix} \begin{pmatrix} I_x \\ I_y \\ I_z \end{pmatrix} \tag{A.5}$$

This is the Ohm's law expressed in a matrix form. However, for electrical conduction in a three-dimensional single-crystalline media, the current density and the potential gradient will not in general have the same direction.

Besides, single crystal silicon has cubic symmetry. Thus, under stress-free conditions silicon has isotropic resistivity and conductivity and the corresponding tensors reduce to a diagonal tensor with the same value in all orthogonal directions:

$$\rho = \rho_0 \begin{pmatrix} 1 & 0 & 0 \\ 0 & 1 & 0 \\ 0 & 0 & 1 \end{pmatrix} \tag{A.6}$$

where $\boldsymbol{\rho_0}$ is the isotropic resistivity of the unstressed crystal.

This means that the relation between $\vec{E}$ and $\vec{I}$ in the material is isotropic, i.e.,

$$\begin{pmatrix} E_x \\ E_y \\ E_z \end{pmatrix} = \begin{pmatrix} \rho_0 & 0 & 0 \\ 0 & \rho_0 & 0 \\ 0 & 0 & \rho_0 \end{pmatrix} \begin{pmatrix} I_x \\ I_y \\ I_z \end{pmatrix} \tag{A.7}$$

Nevertheless, once the crystal is deformed by a stress, the equation (A.7) is no longer valid and the resistivity needs to be described with the anisotropic resistivity tensor.

A stress tensor is a second rank tensor with six independent components. It can be expressed as:

$$T = \begin{pmatrix} T_1 & T_6 & T_5 \\ T_6 & T_2 & T_4 \\ T_5 & T_4 & T_3 \end{pmatrix} \tag{A.8}$$

where $T_1 = T_{xx}$, $T_2 = T_{yy}$, $T_3 = T_{zz}$, $T_4 = T_{yz}$, $T_5 = T_{zx}$, and $T_6 = T_{xy}$.

The piezoresistance effect states that in a crystalline material, the stress tensor causes the change of resistivity tensor. A general expression is written as:

$$\begin{pmatrix} \rho_1 \\ \rho_2 \\ \rho_3 \\ \rho_4 \\ \rho_5 \\ \rho_6 \end{pmatrix} = \begin{pmatrix} \rho_0 \\ \rho_0 \\ \rho_0 \\ 0 \\ 0 \\ 0 \end{pmatrix} + \rho_0 \begin{pmatrix} \pi_{11} & \pi_{12} & \pi_{13} & \pi_{14} & \pi_{15} & \pi_{16} \\ \pi_{21} & \pi_{22} & \pi_{23} & \pi_{24} & \pi_{25} & \pi_{26} \\ \pi_{31} & \pi_{32} & \pi_{33} & \pi_{34} & \pi_{35} & \pi_{36} \\ \pi_{41} & \pi_{42} & \pi_{43} & \pi_{44} & \pi_{45} & \pi_{46} \\ \pi_{51} & \pi_{52} & \pi_{53} & \pi_{54} & \pi_{55} & \pi_{56} \\ \pi_{61} & \pi_{62} & \pi_{63} & \pi_{64} & \pi_{65} & \pi_{66} \end{pmatrix} \begin{pmatrix} T_1 \\ T_2 \\ T_3 \\ T_4 \\ T_5 \\ T_6 \end{pmatrix} \tag{A.9}$$

The relative change of the resistivity component is defined as:

$$\Delta\rho_i = \frac{\rho_i - \rho_0}{\rho_0}, (i = 1, 2, 3); \quad \Delta\rho_j = \frac{\rho_j}{\rho_0}, (j = 4, 5, 6) \tag{A.10}$$

then, using (A.10) the anisotropic resistivity tensor can be written as the sum of the stress-free resistivity and the stress variation or the resistivity.

$$\begin{pmatrix} \rho_1 & \rho_6 & \rho_5 \\ \rho_6 & \rho_2 & \rho_4 \\ \rho_5 & \rho_4 & \rho_3 \end{pmatrix} = \rho_0 \begin{pmatrix} 1 & 0 & 0 \\ 0 & 1 & 0 \\ 0 & 0 & 1 \end{pmatrix} + \rho_0 \begin{pmatrix} \Delta\rho_1 & \Delta\rho_6 & \Delta\rho_5 \\ \Delta\rho_6 & \Delta\rho_2 & \Delta\rho_4 \\ \Delta\rho_5 & \Delta\rho_4 & \Delta\rho_3 \end{pmatrix} \tag{A.11}$$

where $(\Delta\rho)$ is a second rank tensor determined by the piezoresistive coefficient tensor (π) and the stress (T).

Relative changes in the resistivity can be written as a product of the structural stresses, σ, and the piezoresistive stress coefficients. In Voigt notation, this reads:

$$\begin{pmatrix} \Delta\rho_1 \\ \Delta\rho_2 \\ \Delta\rho_3 \\ \Delta\rho_4 \\ \Delta\rho_5 \\ \Delta\rho_6 \end{pmatrix} = \begin{pmatrix} \pi_{11} & \pi_{12} & \pi_{13} & \pi_{14} & \pi_{15} & \pi_{16} \\ \pi_{21} & \pi_{22} & \pi_{23} & \pi_{24} & \pi_{25} & \pi_{26} \\ \pi_{31} & \pi_{32} & \pi_{33} & \pi_{34} & \pi_{35} & \pi_{36} \\ \pi_{41} & \pi_{42} & \pi_{43} & \pi_{44} & \pi_{45} & \pi_{46} \\ \pi_{51} & \pi_{52} & \pi_{53} & \pi_{54} & \pi_{55} & \pi_{56} \\ \pi_{61} & \pi_{62} & \pi_{63} & \pi_{64} & \pi_{65} & \pi_{66} \end{pmatrix} \begin{pmatrix} T_1 \\ T_2 \\ T_3 \\ T_4 \\ T_5 \\ T_6 \end{pmatrix} \tag{A.12}$$

The piezoresistive coefficients (π_{ijkl}) require four subscripts because they relate two second-rank tensors of stress and resistivity. The first subscript (i), refers to the electrical field component (measured potential), the second (j), to the current density (current), and the third (k), and fourth (l), to the stress (stress has two directional components). For the sake of simplicity the subscripts of each tensor are collapsed [81], i.e., $\pi_{1111} \rightarrow \pi_{11}$, $\pi_{1122} \rightarrow \pi_{12}$.

The basic unit of the diamond structure is a face-centered cubic cell that has the symmetry of O_h group. The silicon crystal has a diamond structure and according with [2], in the crystallographic coordinate system of the crystal, there are only three non-zero independent components for the piezoresistive coefficient tensor. They are $\pi_{11} = \pi_{22} = \pi_{33}$, $\pi_{12} = \pi_{21} = \pi_{13} = \pi_{31} = \pi_{23} = \pi_{32}$, and $\pi_{44} = \pi_{55} = \pi_{66}$. Hence, the piezoresistive coefficient tensor of silicon has a simple form in a crystallographic coordinate system if the $x-$, $y-$, and $z-$ axes are aligned to the <100> crystal axes of silicon:

$$\pi = \begin{pmatrix} \pi_{11} & \pi_{12} & \pi_{12} & 0 & 0 & 0 \\ \pi_{12} & \pi_{11} & \pi_{12} & 0 & 0 & 0 \\ \pi_{12} & \pi_{12} & \pi_{11} & 0 & 0 & 0 \\ 0 & 0 & 0 & \pi_{44} & 0 & 0 \\ 0 & 0 & 0 & 0 & \pi_{44} & 0 \\ 0 & 0 & 0 & 0 & 0 & \pi_{44} \end{pmatrix} \tag{A.13}$$

Considering the piezoresistive matrix of silicon in (A.13), and using the equation (A.12) the relative changes in the resistivity for silicon due to stress is written as:

$$\begin{pmatrix} \Delta\rho_1 \\ \Delta\rho_2 \\ \Delta\rho_3 \\ \Delta\rho_4 \\ \Delta\rho_5 \\ \Delta\rho_6 \end{pmatrix} = (\pi)\,(T) = \begin{pmatrix} \pi_{11} & \pi_{12} & \pi_{12} & 0 & 0 & 0 \\ \pi_{12} & \pi_{11} & \pi_{12} & 0 & 0 & 0 \\ \pi_{12} & \pi_{12} & \pi_{11} & 0 & 0 & 0 \\ 0 & 0 & 0 & \pi_{44} & 0 & 0 \\ 0 & 0 & 0 & 0 & \pi_{44} & 0 \\ 0 & 0 & 0 & 0 & 0 & \pi_{44} \end{pmatrix} \begin{pmatrix} T_1 \\ T_2 \\ T_3 \\ T_4 \\ T_5 \\ T_6 \end{pmatrix} \tag{A.14}$$

The piezoresistive coefficients of single-crystal silicon are not constants but they are affected by three factors such as: the doping concentration, type of dopant, and the temperature of the substrate [82, 83]. For both, n- and p- type silicon, the value of the piezoresistive coefficients decreases with increasing temperature and doping concentrations.

The three non-zero independent components were estimated in a experiment by [2] for high resistivity silicon material. The data is presented in Table (A.1).

Table A.1: Components of the piezoresistive coefficient tensor in silicon.

Coefficient	Unit	Material	
		n-Si ($\rho_0 = 11.7\ \Omega cm$)	p-Si ($\rho_0 = 7.8\ \Omega cm$)
π_{11}	$10^{-11} Pa^{-1}$	-102.2	6.6
π_{12}	$10^{-11} Pa^{-1}$	53.4	-1.1
π_{44}	$10^{-11} Pa^{-1}$	-13.6	138.1

A.2 Coordinate System Transformation

When a piezoresistive element is defined in an arbitrary coordinate system, see figure A.1, it is necessary to perform a coordinate transformation to obtain the respective piezoresistive coefficients π'_{ij} and the stress T'_{kl}.

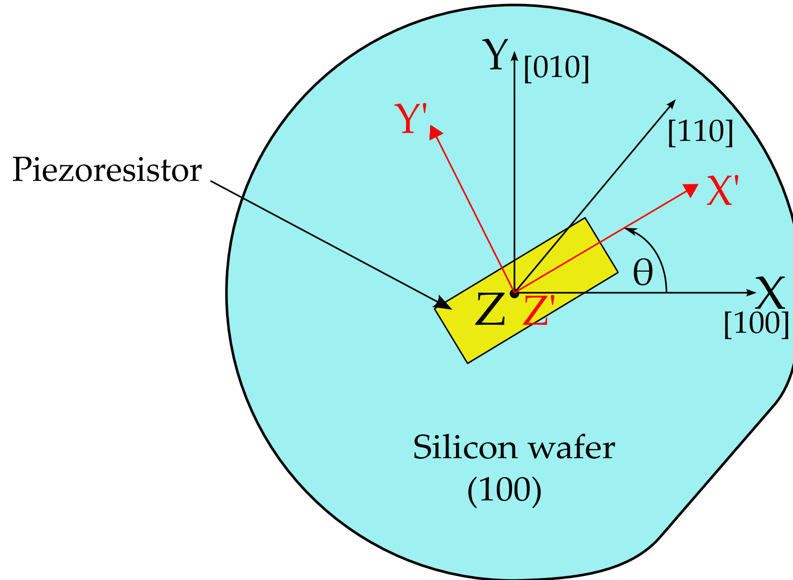

Figure A.1: A piezoresistor at an arbitrary coordinate system

The analysis of the coordinate transformation for the piezoresistive coefficient tensor is described in the following section.

In the coordinate system O-XYZ, a vector $\vec{r}$ as shown in figure A.2 can be expressed by

$$\vec{r} = x\vec{i} + y\vec{j} + z\vec{k} \tag{A.15}$$

Where $\vec{i}$, $\vec{j}$ and $\vec{k}$ are unit vectors in the X-, Y- and Z- directions, respectively.

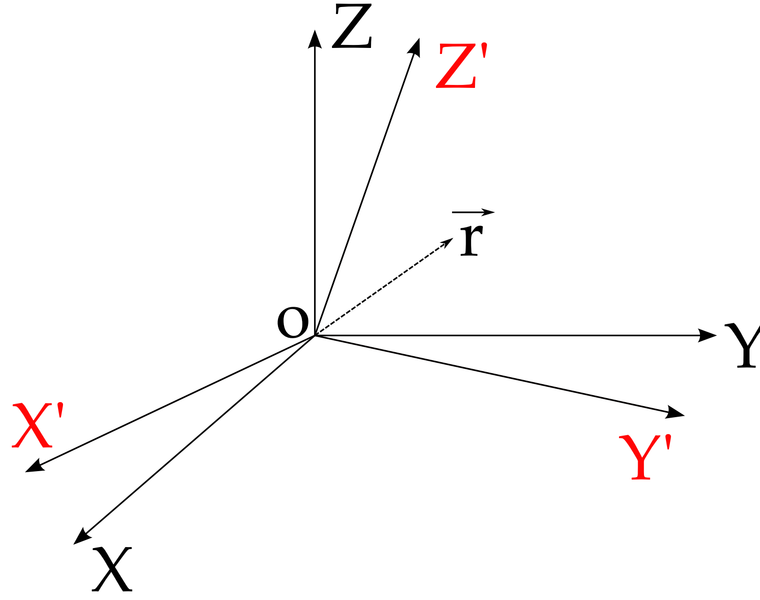

Figure A.2: Locating a vector in two coordinate system

Now, the same vector $\vec{r}$ can also be located in the Cartesian coordinate system O-X'Y'Z' as follows

$$\vec{r}' = x'\vec{i}' + y'\vec{j}' + z'\vec{k}' \tag{A.16}$$

Where $\vec{i}'$, $\vec{j}'$ and $\vec{k}'$ are units vectors in the X'-, Y'- and Z' -directions, respectively. Since $\vec{r}'$ and $\vec{r}$ is te same vector, we can write

$$x'\vec{i}' + y'\vec{j}' + z'\vec{k}' = x\vec{i} + y\vec{j} + z\vec{k} \tag{A.17}$$

The relationship is referred to as the coordinate transformation of vector (first rank tensor) and generally is expressed as

$$\begin{pmatrix} \vec{i}' \\ \vec{j}' \\ \vec{k}' \end{pmatrix} = \begin{pmatrix} l_1 & m_1 & n_1 \\ l_2 & m_2 & n_2 \\ l_3 & m_3 & n_3 \end{pmatrix} \begin{pmatrix} \vec{i} \\ \vec{j} \\ \vec{k} \end{pmatrix} \equiv (R) \begin{pmatrix} \vec{i} \\ \vec{j} \\ \vec{k} \end{pmatrix} \tag{A.18}$$

Where l_1, m_1 and n_1 are direction cosines of $\vec{i}'$ on the X-, Y- and Z-axes, respectively. Similary, l_2, m_2, n_2, and l_3, m_3, n_3 are direction cosines of $\vec{j}'$ and $\vec{k}'$. Hence the matrix formed by $l's$, $m's$ and $n's$ is denoted as (R).

The inverse relation to equation (A.18) is described by

$$\begin{pmatrix} \vec{i} \\ \vec{j} \\ \vec{k} \end{pmatrix} = \begin{pmatrix} l_1 & l_2 & l_3 \\ m_1 & m_2 & m_3 \\ n_1 & n_2 & n_3 \end{pmatrix} \begin{pmatrix} \vec{i}' \\ \vec{j}' \\ \vec{k}' \end{pmatrix} \equiv (R^{-1}) \begin{pmatrix} \vec{i}' \\ \vec{j}' \\ \vec{k}' \end{pmatrix} \tag{A.19}$$

Therefore using equations (A.18) and (A.19), we have

$$\begin{pmatrix} \vec{i}' \\ \vec{j}' \\ \vec{k}' \end{pmatrix} = (R) \begin{pmatrix} \vec{i} \\ \vec{j} \\ \vec{k} \end{pmatrix} = (R)(R^{-1}) \begin{pmatrix} \vec{i}' \\ \vec{j}' \\ \vec{k}' \end{pmatrix} \tag{A.20}$$

Finally, since $(R)(R^{-1}) = I$ is a unity matrix, we have the relations among the direction cosines

$$l_i^2 + m_i^2 + n_i^2 = 1 \qquad (i = 1, 2, 3) \tag{A.21}$$

$$l_i l_j + m_i m_j + n_i n_j = 0 \qquad (i \neq j) \tag{A.22}$$

A.3 The Euler's Angles

As mentioned in appendix A.2, the matrix (R) represents the relation between O-XYZ and O-X'Y'Z'. In fact, there are nine components in (R), but only three are independent ones because of the six restriction conditions given in equation (A.21). The relationship between O-XYZ and O-X'Y'Z' can be described by three rotation angles known as Euler's angles, see figure A.3.

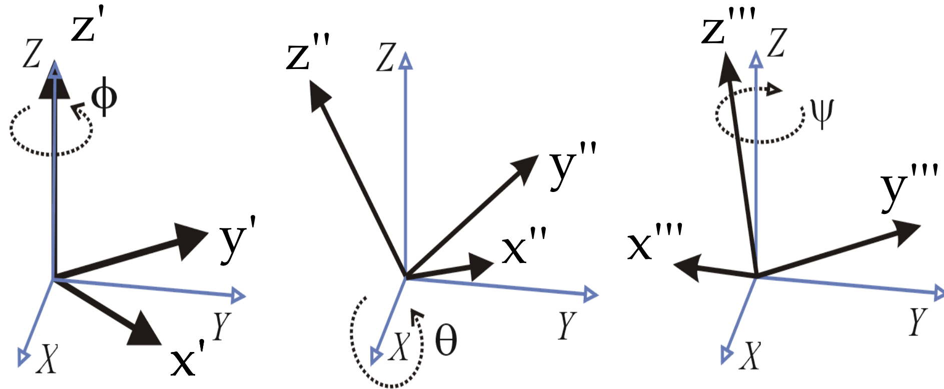

Figure A.3: Rlationship between two coordinate systems by Euler's angles

From the Euler's angles we can conclude that if they are known for two coordinate system, the direction cosines between the two coordinate systems can be found.

$$\begin{pmatrix} x''' \\ y''' \\ z''' \end{pmatrix} = \begin{pmatrix} cos\psi cos\theta cos\phi - sin\psi sin\phi & cos\psi cos\theta sin\phi + sin\psi cos\phi & -cos\psi sin\theta \\ -sin\psi cos\theta cos\phi - cos\psi sin\phi & -sin\psi cos\theta sin\phi + cos\psi cos\phi & sin\psi sin\theta \\ sin\theta cos\phi & sin\theta sin\phi & cos\theta \end{pmatrix} \begin{pmatrix} x \\ y \\ z \end{pmatrix}$$

$$\begin{pmatrix} x''' \\ y''' \\ z''' \end{pmatrix} \equiv \begin{pmatrix} l_1 & m_1 & n_1 \\ l_2 & m_2 & n_2 \\ l_3 & m_3 & n_3 \end{pmatrix} \begin{pmatrix} x \\ y \\ z \end{pmatrix} \tag{A.23}$$

If the Euler's angles for the two coordinate systems are known, the direction cosines between the two coordinate systems can be found.

The tensor relating to first rank tensor is a second rank tensor. A resistivity tensor relating an electric current density tensor (a first rank tensor, or a vector) and an electric field tensor (a first rank tensor, or a vector) is a second rank tensor. For mentioning other second rank tensors include conductivity, stress, strain, etc.

Take resistivity tensor as an example. The relation between $\vec{E}$ and $\vec{J}$ in the O-XYZ coordinate system is

$$(E) = (\rho) \cdot (J) \tag{A.24}$$

while in the O-X'Y'Z' coordinate system, the same relationship can be expressed as

$$(E') = (\rho') \cdot (J') \tag{A.25}$$

As E and J are first rank tensors, we have $(E') = (R) \cdot (E)$ and $(J') = (R) \cdot (J)$

Therefore, we have

$$(R) \cdot (E) = (\rho') \cdot (R) \cdot (J) \tag{A.26}$$

By left-multiplying the equation by (R^{-1}) on both sides, we find

$$(E) = (R^{-1}) \cdot (\rho') \cdot (R) \cdot (J) \tag{A.27}$$

When equation (A.27) is compared with equation (A.24), we have

$$(\rho) = (R^{-1}) \cdot (\rho') \cdot (R) \tag{A.28}$$

Equation (A.28) can also be expressed as

$$(\rho') = (R) \cdot (\rho) \cdot (R^{-1}) \tag{A.29}$$

The full expression of (A.29) is

$$\begin{pmatrix} \rho'_{xx} & \rho'_{xy} & \rho'_{xz} \\ \rho'_{yx} & \rho'_{yy} & \rho'_{yz} \\ \rho'_{zx} & \rho'_{zy} & \rho'_{zz} \end{pmatrix} = \begin{pmatrix} l_1 & m_1 & n_1 \\ l_2 & m_2 & n_2 \\ l_3 & m_3 & n_3 \end{pmatrix} \begin{pmatrix} \rho_{xx} & \rho_{xy} & \rho_{xz} \\ \rho_{yx} & \rho_{yy} & \rho_{yz} \\ \rho_{zx} & \rho_{zy} & \rho_{zz} \end{pmatrix} \begin{pmatrix} l_1 & l_2 & l_3 \\ m_1 & m_2 & m_2 \\ n_1 & n_2 & n_3 \end{pmatrix} \tag{A.30}$$

Now, if the equation (A.30) is developed and the simplified notations are used for the symmetrical resistivity tensor, we can write

$$\begin{pmatrix} \rho'_1 \\ \rho'_2 \\ \rho'_3 \\ \rho'_4 \\ \rho'_5 \\ \rho'_6 \end{pmatrix} = \begin{pmatrix} l_1^2 & m_1^2 & n_1^2 & 2m_1n_1 & 2n_1l_1 & 2l_1m_1 \\ l_2^2 & m_2^2 & n_2^2 & 2m_2n_2 & 2n_2l_2 & 2l_2m_2 \\ l_3^2 & m_3^2 & n_3^2 & 2m_3n_1 & 2n_3l_3 & 2l_3m_3 \\ l_2l_3 & m_2m_3 & n_2n_3 & m_2n_3+m_3n_2 & n_2l_3+n_3l_2 & m_2l_3+m_3l_2 \\ l_3l_1 & m_3m_1 & n_3n_1 & m_3n_1+m_1n_3 & n_3l_1+n_1l_3 & m_3l_1+m_1l_3 \\ l_1l_2 & m_1m_2 & n_1n_2 & m_1n_2+m_2n_1 & n_1l_2+n_2l_1 & m_1l_2+m_2l_1 \end{pmatrix} \begin{pmatrix} \rho_1 \\ \rho_2 \\ \rho_3 \\ \rho_4 \\ \rho_5 \\ \rho_6 \end{pmatrix} \tag{A.31}$$

A simplified notation for equation (A.31) is $(\rho') = (\alpha)(\rho)$, where

$$\alpha = \begin{pmatrix} l_1^2 & m_1^2 & n_1^2 & 2m_1n_1 & 2n_1l_1 & 2l_1m_1 \\ l_2^2 & m_2^2 & n_2^2 & 2m_2n_2 & 2n_2l_2 & 2l_2m_2 \\ l_3^2 & m_3^2 & n_3^2 & 2m_3n_1 & 2n_3l_3 & 2l_3m_3 \\ l_2l_3 & m_2m_3 & n_2n_3 & m_2n_3+m_3n_2 & n_2l_3+n_3l_2 & m_2l_3+m_3l_2 \\ l_3l_1 & m_3m_1 & n_3n_1 & m_3n_1+m_1n_3 & n_3l_1+n_1l_3 & m_3l_1+m_1l_3 \\ l_1l_2 & m_1m_2 & n_1n_2 & m_1n_2+m_2n_1 & n_1l_2+n_2l_1 & m_1l_2+m_2l_1 \end{pmatrix} \tag{A.32}$$

The tensor of stress T, the strain ε and the relative change of resistivity Δ are all second rank tensors, the coordinate transformation relationships for them are $T' = \alpha T$, $\varepsilon' = \alpha\varepsilon$ and $\Delta' = \alpha\Delta$.

As is mentioned, the piezoresistive coefficient is a forth rank tensor relating two tensors of the second rank, the resistivity tensor ρ and the stress tensor T. The relation in the coordinate system O-XYZ, is $\Delta = \pi \cdot T$ as shown by equation (A.14). The same expression but now in the O-X'Y'Z' coordinate system is

$$\Delta' = \pi' \cdot T' \tag{A.33}$$

As Δ and T are second rank tensors, therefore we have $\alpha\Delta = \pi'\alpha T$. Therefore, we obtain

$$\Delta = \alpha^{-1}\pi'\alpha T \tag{A.34}$$

And comparing equation (A.34) with equation (A.12), we have te relation of coordinate transformation for the piezoresistive coefficient tensor $\pi = \alpha^{-1}\pi'\alpha$; or

$$\pi' = \alpha\pi\alpha^{-1} \tag{A.35}$$

This means that the components of π' can be expressed by the components of π by

$$\pi'_{ij} = \sum_{k,l=1}^{6} \alpha_{ij}\pi_{kl}\alpha_{ij}^{-1} \tag{A.36}$$

For instance, the π_{1j} piezoresistive coefficients used for two-terminal piezoresistors are:

$$\pi'_{11} = \pi_{11} - 2(\pi_{11} - \pi_{12} - \pi_{44})[(l_1m_1)^2 + (n_1m_1)^2 + (l_1n_1)^2] \tag{A.37}$$

Using the notation of $\pi_0 = \pi_{11} - \pi_{12} - \pi_{44}$, we have finally the expression

$$\pi'_{11} = \pi_{11} - 2\pi_0(l_1^2m_1^2 + l_1^2n_1^2 + m_1^2n_1^2)$$

All other components of π' matrix are listed in the table A.2 [63], the results have been obtained in a batch derivation by using matrix algebra method [84].

Table A.2: Piezoresistive tensor at an arbitrary coordinate system

$\pi'_{11} = \pi_{11} - 2\pi_0(l_1^2m_1^2 + l_1^2n_1^2 + m_1^2n_1^2)$	$\pi'_{14} = 2\pi'_{41}$
$\pi'_{21} = \pi_{12} + \pi_0(l_1^2l_2^2 + m_1^2m_2^2 + n_1^2n_2^2)$	$\pi'_{24} = 2\pi'_{42}$
$\pi'_{31} = \pi_{12} + \pi_0(l_1^2l_3^2 + m_1^2m_3^2 + n_1^2n_3^2)$	$\pi'_{34} = 2\pi'_{43}$
$\pi'_{41} = \pi_0(l_1^2l_2l_3 + m_1^2m_2m_3 + n_1^2n_2n_3)$	$\pi'_{44} = \pi_{44} + 2\pi_0(l_2^2l_3^2 + m_2^2m_3^2 + n_2^2n_3^2)$
$\pi'_{51} = \pi_0(l_1^3l_3 + m_1^3m_3 + n_1^3n_3)$	$\pi'_{54} = 2\pi_0(l_1l_2l_3^2 + m_1m_2m_3^2 + n_1n_2n_3^2)$
$\pi'_{61} = \pi_0(l_1^3l_2 + m_1^3m_2 + n_1^3n_2)$	$\pi'_{64} = 2\pi_0(l_1l_2^2l_3 + m_1m_2^2m_3 + n_1n_2^2n_3)$
$\pi'_{12} = \pi'_{21}$	$\pi'_{15} = 2\pi'_{51}$
$\pi'_{22} = \pi_{11} - 2\pi_0(l_2^2m_2^2 + l_2^2n_2^2 + m_2^2n_2^2)$	$\pi'_{25} = 2\pi'_{52}$
$\pi'_{32} = \pi_{12} + \pi_0(l_2^2l_3^2 + m_2^2m_3^2 + n_2^2n_3^2)$	$\pi'_{35} = 2\pi'_{53}$
	continued on next page

Table A.2 – continued from previous page

$\pi'_{42} = \pi_0(l_2^3 l_3 + m_2^3 m_3 + n_2^3 n_3)$	$\pi'_{45} = 2\pi'_{63} = \pi'_{54}$
$\pi'_{52} = \pi_0(l_1 l_2^2 l_3 + m_1 m_2^2 m_3 + n_1 n_2^2 n_3)$	$\pi'_{55} = \pi_{44} + 2\pi_0(l_1^2 l_3^2 + m_1^2 m_3^2 + n_1^2 n_3^2)$
$\pi'_{62} = \pi_0(l_1 l_2^3 + m_1 m_2^3 + n_1 n_2^3)$	$\pi'_{65} = 2\pi'_{41}$
$\pi'_{13} = \pi'_{31}$	$\pi'_{16} = 2\pi'_{61}$
$\pi'_{23} = \pi'_{32}$	$\pi'_{26} = 2\pi'_{62}$
$\pi'_{33} = \pi_{11} - 2\pi_0(l_3^2 m_3^2 + l_3^2 n_3^2 + m_3^2 n_3^2)$	$\pi'_{36} = 2\pi'_{63}$
$\pi'_{43} = \pi_0(l_2 l_3^3 + m_2 m_3^3 + n_2 n_3^3)$	$\pi'_{46} = 2\pi'_{52}$
$\pi'_{53} = \pi_0(l_1 l_3^3 + m_1 m_3^3 + n_1 n_3^3)$	$\pi'_{56} = 2\pi'_{41}$
$\pi'_{63} = \pi_0(l_1 l_2 l_3^2 + m_1 m_2 m_3^2 + n_1 n_2 n_3^2)$	$\pi'_{66} = \pi_{44} + 2\pi_0(l_1^2 l_2^2 + m_1^2 m_2^2 + n_1^2 n_2^2)$

Bibliography

[1] S. Camacho-León., *Design, Fabrication and Characterization of a High-Speed, Bimodal, CMOS-MEMS Resonant Scanner Driven By Temperature-Gradient Actuators.* Phd, thesis, Instituto Tecnológico y de Estudios Superiores de Monterrey, May 2010.

[2] C. S. Smith, "Piezoresistance effect in germanium and silicon," *Phys. Rev.*, vol. 94, pp. 42–49, Apr 1954.

[3] W. Paul and G. L. Pearson, "Pressure dependence of the resistivity of silicon," *Phys. Rev.*, vol. 98, pp. 1755–1757, Jun 1955.

[4] M. Madou, *Fundamentals of Microfabrication: The Science of Miniaturization.* CRC Press, 2002.

[5] A. Hierlemann, *Integrated Chemical Microsensors Systems in CMOS Technology.* Microtechnology and MEMS, Springer, 2005.

[6] X. Huang, S. Li, J. S. Schultz, Q. Wang, and Q. Lin, "A mems affinity glucose sensor using a biocompatible glucose-responsive polymer," *Sensors and Actuators B: Chemical*, vol. 140, no. 2, pp. 603 – 609, 2009.

[7] Y. Huang, E. Mather, J. Bell, and M. Madou, "Mems-based sample preparation for molecular diagnostics," *Analytical and Bioanalytical Chemistry*, vol. 372, pp. 49–65, 2002. 10.1007/s00216-001-1191-9.

[8] A. Adami, F. Borghetti, N. Massari, M. Decarli, C. Collini, L. Lorenzelli, and D. Stoppa, "Design of a cantilever-based system for dna detection," in *Ph.D. Research in Microelectronics and Electronics (PRIME), 2011 7th Conference on*, pp. 61 –64, july 2011.

[9] M. Northrup, C. Gonzalez, D. Hadley, R. Hills, P. Landre, S. Lehew, R. Saw, J. Sninsky, and R. Watson, "A mems-based miniature dna analysis system," in *Solid-State Sensors and Actuators, 1995 and Eurosensors IX.. Transducers '95. The 8th International Conference on*, vol. 1, pp. 764 –767, jun 1995.

[10] R. Bogue, "MEMS sensors: past, present and future," *Sensor Review*, vol. 27, no. 1, pp. 7–13, 2007.

[11] H. Fujita, "A decade of mems and its future," in *Micro Electro Mechanical Systems, 1997. MEMS '97, Proceedings, IEEE., Tenth Annual International Workshop on*, pp. 1 –7, jan 1997.

[12] G. Binnig, C. F. Quate, and C. Gerber, "Atomic force microscope," *Phys. Rev. Lett.*, vol. 56, pp. 930–933, Mar 1986.

[13] H. Goldstein, "A beautiful noise [invention of stm and afm]," *Spectrum, IEEE*, vol. 41, pp. 50 – 52, may 2004.

[14] A. Adami, M. Decarli, L. Lorenzelli, V. Guarnieri, M. Malfatti, C. Apetrei, and M. L. R. Mendez, "Microcantilever-based sensor array tor amine detection in agro-tood applications," *Integration Issues of Miniaturized Systems - MOMS, MOEMS, ICS and Electronic Components (SSI), 2008 2nd European Conference Exhibition on*, pp. 1 –3, april 2008.

[15] Z. Yi, X. Liao, and Z. Zhu, "An 8-12ghz capacitive power sensor based on mems cantilever beam," in *Sensors, 2011 IEEE*, pp. 1958 –1961, oct. 2011.

[16] D. W. Dareing and T. Thundat, "Simulation of adsorption-induced stress of a microcantilever sensor," *Journal of Applied Physics*, vol. 97, no. 4, p. 043526, 2005.

[17] C. Leondes, *Mems/Nems: (1) Handbook Techniques and Applications Design Methods, (2) Fabrication Techniques, (3) Manufacturing Methods, (4) Sensors and Actuators, (5) Medical Applications and MOEMS*. MEMS/NEMS: Handbook Techniques and Applications, Springer, 2006.

[18] G. Binnig, H. Rohrer, C. Gerber, and E. Weibel, "Surface studies by scanning tunneling microscopy," *Physical Review Letters*, vol. 49, no. 1, pp. 57–61, 1982.

[19] C. Ziegler, "Cantilever-based biosensors," *Analytical and Bioanalytical Chemistry*, vol. 379, pp. 946–959, Aug. 2004.

[20] K.-U. Kirstein, Y. Li, M. Zimmermann, C. Vancura, T. Volden, W. H. Song, J. Lichtenberg, and A. Hierlemann, "Cantilever-based biosensors in cmos technology," *CoRR*, vol. abs/0710.4692, 2007.

[21] M. Godin, V. Tabard-Cossa, Y. Miyahara, T. Monga, P. J. Williams, L. Y. Beaulieu, R. Bruce Lennox, and P. Grutter, "Cantilever-based sensing: the origin of surface stress and optimization strategies.," *Nanotechnology*, vol. 21, no. 7, p. 75501, 2010.

[22] F. Liu, Y. Zhang, and Z. can Ou-Yang, "Flexoelectric origin of nanomechanic deflection in dna-microcantilever system," *Biosensors and Bioelectronics*, vol. 18, pp. 655 – 660, 2003. Selected papers from the Seventh World Congress on Biosensors Kyoto, Japan 15-17 May 2002.

[23] V. Seena, A. Nigam, P. Pant, S. Mukherji, and V. R. Rao, “"organic cantifet": A nanomechanical polymer cantilever sensor with integrated ofet,” *Microelectromechanical Systems, Journal of*, vol. 21, pp. 294 –301, april 2012.

[24] J. Fritz, M. K. Baller, H. P. Lang, H. Rothuizen, P. Vettiger, E. Meyer, H. J. Güntherodt, C. Gerber, and J. K. Gimzewski, “Translating biomolecular recognition into nanomechanics,” *Science*, vol. 288, no. 5464, pp. 316–318, 2000.

[25] N. Gilda, S. Nag, S. Patil, M. Baghini, D. Sharma, and V. Rao, “Current excitation method for δR measurement in piezo-resistive sensors with a 0.3-ppm resolution,” *Instrumentation and Measurement, IEEE Transactions on*, vol. 61, pp. 767 –774, march 2012.

[26] C. Reddy, M. Khaderbad, and R. Rao, “Piezoresistive su-8 cantilever with fe(iii)porphyrin coating for co sensing,” *Nanotechnology, IEEE Transactions on*, vol. PP, no. 99, p. 1, 2012.

[27] S. Firdaus, H. Omar, and I. Azid, “Fabrication of mass sensitive piezoresistive cantilever structure for biochemical detection,” in *Humanities, Science and Engineering (CHUSER), 2011 IEEE Colloquium on*, pp. 530 –532, dec. 2011.

[28] R. Zhang, Y. Chen, W. Ko, D. Rosenbaum, X. Yu, and P.-L. Feng, “Ex vivo monitoring of rat heart wall motion using piezoelectric cantilevers,” in *Frequency Control and the European Frequency and Time Forum (FCS), 2011 Joint Conference of the IEEE International*, pp. 1 –6, may 2011.

[29] S. Rabbani and P. Brishbhan, “Cantilever embedded mosfet for bio-sensing,” in *Electrical and Computer Engineering (CCECE), 2011 24th Canadian Conference on*, pp. 000489 –000492, may 2011.

[30] M. Islam, S. Das, and M. Shandhi, “Design, fabrication and performance evaluation of a piezoresistive arsenic sensor,” in *Electrical and Computer Engineering (ICECE), 2010 International Conference on*, pp. 239 –242, dec. 2010.

[31] N. Madzhi, L. Khuan, M. Abdullah, and A. Ahmad, “Development of a low cost self-sensing piezoresistive microcantilever biosensor and read-out circuitry for measuring salivary-amylase activity,” in *Electronic Computer Technology (ICECT), 2010 International Conference on*, pp. 9 –13, may 2010.

[32] S. Schmid, P. Wagli, and C. Hierold, “Biosensor based on all-polymer resonant microbeams,” in *Micro Electro Mechanical Systems, 2009. MEMS 2009. IEEE 22nd International Conference on*, pp. 300 –303, jan. 2009.

[33] Y. Li, C. Vancura, K.-U. Kirstein, J. Lichtenberg, and A. Hierlemann, “Monolithic resonant-cantilever-based cmos microsystem for biochemical sensing,” *Circuits and Systems I: Regular Papers, IEEE Transactions on*, vol. 55, pp. 2551 –2560, oct. 2008.

[34] R. Rahim, B. Bais, and B. Majlis, "Design and analysis of mems piezoresistive sio2 cantilever-based sensor with stress concentration region for biosensing applications," in *Semiconductor Electronics, 2008. ICSE 2008. IEEE International Conference on*, pp. 211 –215, nov. 2008.

[35] G. Villanueva, G. Rius, J. Montserrat, F. Perez-Murano, and J. Bausells, "Piezoresistive microcantilevers for biomolecular force detection," in *Electron Devices, 2007 Spanish Conference on*, pp. 212 –215, 31 2007-feb. 2 2007.

[36] H. Ocakli, A. Ozturk, N. Ozber, H. Kavakli, E. Alaca, and H. Urey, "Resonant cantilever bio sensor with integrated grating readout," in *Optical MEMs and Nanophotonics, 2008 IEEE/LEOS Internationall Conference on*, pp. 46 –47, aug. 2008.

[37] S. A. Trammell, L. Wang, J. M. Zullo, R. Shashidhar, and N. Lebedev, "Orientated binding of photosynthetic reaction centers on gold using nióóâËĘï£¡nta self-assembled monolayers," *Biosensors and Bioelectronics*, vol. 19, no. 12, pp. 1649 – 1655, 2004.

[38] S. Munnangi, G. Haobijam, M. Kothamasu, R. Paily, and R. Kshetrimayum, "Cmos capacitive pressure sensor design and integration with rfid tag for biomedical applications," in *TENCON 2008 - 2008 IEEE Region 10 Conference*, pp. 1 –6, nov. 2008.

[39] M. Ansari and C. Cho, "Design and analysis of a high sensitive microcantilever biosensor for biomedical applications," in *BioMedical Engineering and Informatics, 2008. BMEI 2008. International Conference on*, vol. 2, pp. 593 –597, may 2008.

[40] T. R. Strick, "Stretching of macromolecules and proteins," *Reports on Progress in Physics*, vol. 66, no. 1, pp. 1–45, 2003.

[41] M. Zimmermann, T. Volden, K.-U. Kirstein, S. Hafizovic, J. Lichtenberg, and A. Hierlemann, "A cmos-based sensor array system for chemical and biochemical applications," in *Solid-State Circuits Conference, 2005. ESSCIRC 2005. Proceedings of the 31st European*, pp. 343 – 346, sept. 2005.

[42] I. Voiculescu, M. Zaghloul, R. McGill, E. Houser, and G. Fedder, "Electrostatically actuated resonant microcantilever beam in cmos technology for the detection of chemical weapons," *Sensors Journal, IEEE*, vol. 5, pp. 641 – 647, aug. 2005.

[43] Y. Li, C. Vancura, D. Barrettino, M. Graf, C. Hagleitner, A. Kummer, K.-U. Kirstein, and A. Hierlemann, "Advanced chemical microsensor systems in cmos technology [gas sensors]," in *Sensors, 2004. Proceedings of IEEE*, pp. 24 – 27 vol.1, oct. 2004.

[44] R. Littrell and K. Grosh, "Modeling and characterization of cantilever-based mems piezoelectric sensors and actuators," *Microelectromechanical Systems, Journal of*, vol. 21, pp. 406 –413, april 2012.

[45] J. Gimzewski, C. Gerber, E. Meyer, and R. Schlittler, "Observation of a chemical reaction using a micromechanical sensor," *Chemical Physics Letters*, vol. 217, pp. 589 – 594, 1994.

[46] J. Fritz, "Cantilever biosensors," *Analyst*, vol. 133, pp. 855–863, 2008.

[47] L. H. Germer and A. U. MacRae, "Surface reconstruction caused by adsorption," *Proceedings of the National Academy of Sciences*, vol. 48, no. 6, pp. 997–1000, 1962.

[48] N. V. Lavrik, M. J. Sepaniak, and P. G. Datskos, "Cantilever transducers as a platform for chemical and biological sensors," *Review of Scientific Instruments*, vol. 75, no. 7, pp. 2229–2253, 2004.

[49] A. Mathad and R. Patrikar, "The origin of surface stress experienced by a micro-cantilever beam," in *Students' Technology Symposium (TechSym), 2010 IEEE*, pp. 12 –16, april 2010.

[50] G. G. Stoney, "The tension of metallic films deposited by electrolysis," *Proceedings of the Royal Society of London. Series A*, vol. 82, no. 553, pp. 172–175, 1909.

[51] R. Shuttleworth, "The surface tension of solids," *Proc. Phys. Soc. A*, vol. 63, pp. 444–457, 1950.

[52] R. E. Martinez, W. M. Augustyniak, and J. A. Golovchenko, "Direct measurement of crystal surface stress," *Phys. Rev. Lett.*, vol. 64, pp. 1035–1038, Feb 1990.

[53] D. Sander, U. Linke, and H. Ibach, "Adsorbate-induced surface stress: sulfur, oxygen and carbon on ni(100)," *Surface Science*, vol. 272, pp. 318 – 325, 1992.

[54] J. Dewolf, *Mechanics Of Materials (In Si Units)*. McGraw-Hill series in mechanical engineering, McGraw-Hill Education (India) Pvt Limited, 2004.

[55] S. TIMOSHENKO, "Analysis of bi-metal thermostats," *J. Opt. Soc. Am.*, vol. 11, pp. 233–255, Sep 1925.

[56] Z. a. Feng and H. a. Liu, "Generalized formula for curvature radius and layer stresses caused by thermal strain in semiconductor multilayer structures," *Journal of Applied Physics*, vol. 54, pp. 83 –85, jan 1983.

[57] D. DeVoe and A. Pisano, "Modeling and optimal design of piezoelectric cantilever microactuators," *Microelectromechanical Systems, Journal of*, vol. 6, pp. 266 –270, sep 1997.

[58] S. Scott, J.-I. Kim, F. Sadeghi, and D. Peroulis, "An analytical capacitance model of temperature-sensitive, large-displacement multimorph cantilevers: Numerical and experimental validation," *Microelectromechanical Systems, Journal of*, vol. 21, pp. 161 –170, feb. 2012.

[59] P. Gilgunn, J. Liu, N. Sarkar, and G. Fedder, "Cmos-mems lateral electrothermal actuators," *Microelectromechanical Systems, Journal of*, vol. 17, pp. 103 –114, feb. 2008.

[60] Burch, "http://engineering.ucsb.edu/hpscicom/projects/me271.htm," August 2006.

[61] J. Gere, *Mechanics of Materials*. Pacific Grove, 2001.

[62] W. Fang and J. Wickert, "Determining mean and gradient residual stresses in thin films using micromachined cantilevers," *Journal of Micromechanics and Microengineering*, vol. 6, no. 3, pp. 301–309, 1996.

[63] M. Bao, *Analysis And Design Principles Of Mems Devices*. Elsevier, 2005.

[64] P. Allen and D. Holberg, *CMOS Analog Circuit Design*. The Oxford Series in Electrical and Computer Engineering, Oxford University Press, USA, 2002.

[65] K.-S. Ou, K.-S. Chen, T.-S. Yang, and S.-Y. Lee, "A novel semianalytical approach for finding pull-in voltages of micro cantilever beams subjected to electrostatic loads and residual stress gradients," *Microelectromechanical Systems, Journal of*, vol. 20, pp. 527 –537, april 2011.

[66] W. S. Yang, S. Cho, H. Ryu, S. H. Cheon, B. G. Yu, and C. A. Choi, "Deformation reduction of a mems sensor by stress balancing of multilayer," in *Sensor Technologies and Applications, 2008. SENSORCOMM '08. Second International Conference on*, pp. 391 –395, aug. 2008.

[67] R. W. Johnstone and M. Parameswaran, "Curl and effective height of micromachined bi-layer cantilevers under differing residual stresses," in *Electrical and Computer Engineering, 2006. CCECE '06. Canadian Conference on*, pp. 1617 –1620, may 2006.

[68] G. F. P.J. Gilgunn, "Flip-chip integrated soi-cmos-mems fabrication technology," pp. 10–13, June 2008.

[69] COMSOL-Multiphysics, "http://www.comsol.se/products/multiphysics," 12 2012.

[70] R. Budynas, J. Shigley, and J. Nisbett, *Shigley's Mechanical Engineering Design*. No. vol. 10 in McGraw-Hill Series in Mechanical Engineering, McGraw-Hill, 2007.

[71] T.-C. Lu, M.-D. Ker, H.-W. Zan, C.-H. Kuo, C.-H. Li, Y.-J. Hsieh, and C.-T. Liu, "Design of bandgap voltage reference circuit with all tft devices on glass substrate in a 3μm ltps process," in *Custom Integrated Circuits Conference, 2008. CICC 2008. IEEE*, pp. 721 –724, sept. 2008.

[72] A. Hatzopoulos, D. Tassis, N. Hastas, C. Dimitriadis, and G. Kamarinos, "On-state drain current modeling of large-grain poly-si tfts based on carrier transport through latitudinal and longitudinal grain boundaries," *Electron Devices, IEEE Transactions on*, vol. 52, pp. 1727 – 1733, aug. 2005.

[73] Electric-VLSI, "http://www.staticfreesoft.com/index.html."

[74] LTSpice, "http://www.linear.com/designtools/software/."

[75] K. Sanborn, D. Ma, and V. Ivanov, "A sub-1-v low-noise bandgap voltage reference," *Solid-State Circuits, IEEE Journal of*, vol. 42, pp. 2466 –2481, nov. 2007.

[76] Y. Li, S. Yufeng, L. Lian, and Z. Zengyu, "Cmos bandgap voltage reference with 1.8-v power supply," in *ASIC, 2003. Proceedings. 5th International Conference on*, vol. 1, pp. 611 – 614 Vol.1, oct. 2003.

[77] R.-M. Weng, X.-R. Hsu, and Y.-F. Kuo, "A 1.8- v high-precision compensated cmos bandgap reference," in *Electron Devices and Solid-State Circuits, 2005 IEEE Conference on*, pp. 271 – 273, dec. 2005.

[78] M. Jingwen, C. Tingqian, C. Cheng, R. Junyan, and Y. Li, "Cmos 1.5v bandgap voltage reference," in *ASIC, 2005. ASICON 2005. 6th International Conference On*, vol. 1, pp. 469 –472, oct. 2005.

[79] C. Liu, *Foundations of MEMS*. Prentice Hall, 2 ed., 2012.

[80] D. M. Grimes, "Onsager's theorem from thermodynamics," *Education, IEEE Transactions on*, vol. 8, pp. 136 –139, dec. 1965.

[81] W. P. Mason and R. N. Thurston, "Use of piezoresistive materials in the measurement of displacement, force, and torque," *The Journal of the Acoustical Society of America*, vol. 29, no. 10, pp. 1096–1101, 1957.

[82] K. Yamada, M. Nishihara, S. Shimada, M. Tanabe, M. Shimazoe, and Y. Matsuoka, "Nonlinearity of the piezoresistance effect of p-type silicon diffused layers," *Electron Devices, IEEE Transactions on*, vol. 29, pp. 71 – 77, jan 1982.

[83] O. N. Tufte and E. L. Stelzer, "Piezoresistive properties of silicon diffused layers," *Journal of Applied Physics*, vol. 34, pp. 313 –318, feb 1963.

[84] M. Bao and Y. Huang, "Batch derivation of piezoresistive coefficient tensor by matrix algebra," *Journal of Micromechanics and Microengineering*, vol. 14, no. 3, p. 332, 2004.